Reconnaissance chirale dans des complexes moléculaires neutres et ioniques

Ananya Sen

ORSAY
N° ORDRE : 2163

UNIVERSITE PARIS-SUD

ÉCOLE DOCTORALE : CHIMIE
Institut des sciences moléculaires d'Orsay

DISCIPLINE CHIMIE

THÈSE DE DOCTORAT

soutenue le 20/09/2012

par

Ananya SEN

Reconnaissance chirale dans des complexes moléculaires neutres et ioniques.

Composition du jury :

Président du jury :	Anne LAFOSSE	ISMO (Université de Paris Sud)
Rapporteurs :	Jeanne CRASSOUS	Université Rennes
	Laurent NAHON	Synchroton SOLEIL
Examinateurs :	Valérie BRENNER	Laboratoire Francis Perrin CEA Saclay
	Fabien CHIROT	Université Lyon
Directeur de thèse :	Anne ZEHNACKER-RENTIEN	ISMO (Universite de Paris Sud)
Membres invités :	Debora SCUDERI	LCP (Université de Paris Sud)

ORSAY
N° ORDRE : 2163

UNIVERSITE PARIS-SUD

ÉCOLE DOCTORALE : CHIMIE
Institut des sciences moléculaires d'Orsay

DISCIPLINE CHIMIE

THÈSE DE DOCTORAT

soutenue le 20/09/2012

par

Ananya SEN

Chiral Recognition in neutral and ionic molecular complexes.

Composition du jury :

Président du jury :	Anne LAFOSSE	ISMO (Université de Paris Sud)
Rapporteurs :	Jeanne CRASSOUS	Université Rennes
	Laurent NAHON	Synchroton SOLEIL
Examinateurs :	Valérie BRENNER	Laboratoire Francis Perrin CEA Saclay
	Fabien CHIROT	Université Lyon
Directeur de thèse :	Anne ZEHNACKER-RENTIEN	ISMO (Universite de Paris Sud)
Membres invités :	Debora SCUDERI	LCP (Université de Paris Sud)

Acknowledgements

I want to express my sincere gratitude and appreciation to my PhD supervisor and mentor Prof. Dr. Anne Zehnacker-Rentien for her generous support during the time of my research, her consistent interest in the progress of my work as well as valuable suggestions and valuable discussions.

Especially, I enjoyed the excellent working conditions and literally no wishes were left unfulfilled with the plenty of top, first-class equipments available. This allowed me to get a broad, profound knowledge in different spectroscopic techniques. Furthermore, I want to thank my supervisor for an overall pleasant atmosphere, the fruitful discussions and her anytime accessibility. Prof. Dr. Jeanne Crassous and Dr Laurent Nahon are gratefully acknowledged for refereeing this thesis. I am also grateful to Prof. Dr Anne Lafosse, Dr Valérie Brenner and Dr Fabien Chirot for agreeing to be part of the jury for my PhD defense. I would also like to thank the director of ISMO Dr Philippe Bréchignac.

The Ecole doctoral de Chimie Paris Sud granted me with a Doctoral Fellowship that allowed me to pursue my research, for which I am very grateful. I thank the French National Research Agency (ANR-Grant ANR-08-BLAN-0158) for financially supporting my research. This research would not have been successful without the support from the Triangle de la physique contract « Dichromol » n° 2007-025T.SFB 623 “Molecular Catalysts – Structure and Functional Design”.

I sincerely thank Dr. Katia Le Barbu Debus for performing all the calculations related to this thesis. My heartfelt gratitude to Dr Valéria Lepere, for teaching me how to handle the instruments in the laboratory and being there to help me whenever I faced any technical difficulty.

I also want to thank Dr Debora Scuderi for collaborating the FEL laser facility (CLIO) with our project. I learnt a lot from the fruitful discussions, the overall pleasant atmosphere, the confidence and exchanging ideas with her.

This thesis would not have been possible without the constant support and guidance from Mr Christophe Charrière of the electronics department and Mr Frédéric Ferreira from the mechanics department. Their continuous guidance and strong support helped me build a confidence to work with electronic devices and instruments which I am sure will help me a lot in the future. The rest of the members of the electronics and mechanics department of ISMO are also acknowledged for their continuous support and guidance.

This thesis would have not been possible without ideas, suggestions and discussions with colleagues and friends. In particular, I would like to thank Dr Christophe Jouvet, Dr Piuzzi, Dr Broquier and Dr Carçabal for providing me with valuable suggestions. I also want to thank my colleague Dr Bouchet for her generous support and friendly conversations.

I also want to thank the rest of the members of the group D (Structure et dynamique des systèmes complexes isolés) of ISMO, for the friendly ambience and guidance throughout the three years of my PhD.

I am indebted to Dr Nikhil Guchchait for instilling in me the confidence to work in a research laboratory and encouraging me throughout the last three years.

I am deeply grateful for the consistent and strong support of my beloved family, my parents, my brother and Chitrak. I would not have been able to complete this thesis without their love, blessings and unfaltering belief in my capabilities.

SUMMARY

INTRODUCTION

INDEX

List of figures

I. CHIRALITY

This thesis is devoted to chiral recognition in the gas phase, in both neutral and ionic systems. In this introductory part, we will recall a few notions which lie at the basis of chirality and chiral recognition.

I.1. Definition

The term *chirality* originates from the Greek word χειρ Kheir which means "hand". Just as the left hand is a mirror image of the right hand and they are non superposable on each other, two molecules are said to be chiral if they behave in a similar manner. Homo-chirality is an important property in life chemistry and is omnipresent in nature.[1] For instance, 19 of the 20 common amino acids that form proteins are themselves chiral, as are a host of other biologically important molecules. Their natural forms all possess the same chirality, as do other simple natural molecules like sugar, or complex macromolecular systems like DNA and RNA. Why nature prefers only one enantiomer of its building blocks remains a puzzle till date……

I.2. History[1,2]

Probably the earliest discovery which is important when one studies chirality goes back to the start of nineteenth century with the discovery of plane-polarised light by the French physicist Malus. This was followed by another discovery by French scientist Arago in 1811. He discovered that a quartz plate, when cut at right angles to its crystal axis, can rotate the plane polarized light through an angle proportional to the thickness of the plate. This observation formed the basis of the phenomenon of optical rotation. He further added that the degree of rotation produced by quartz is a property of the crystal which is observed only in the solid state and depends on the direction in which the crystal is viewed. In 1815 Biot also observed optical activity in samples of certain liquids, such as turpentine, various essential oils, and solutions of substances such as sugar and camphor. Since both pure liquids and solutions of organic compounds

exhibit optical activity, the property could not be attributed to a characteristic of the solid state but instead to the molecular structure.

In the year 1848, Pasteur solved a question related to tartaric acid. Indeed, the tartaric acid usually present in wine lee shows optical rotation. However, it may happen that a peculiar form of tartaric acid found in wine does not show any rotatory power. It is called racemic acid (from the Latin word racemus which means grape). Mitscherlich, a German chemist and mineralogist, has proposed that the only difference between tartaric and racemic acids was the presence of optical rotation in the former and not in the latter. Pasteur discovered that the crystals of Na^+/NH_4^+ salts of racemic acid were composed of hemihedral crystals which were mirror image to each other.

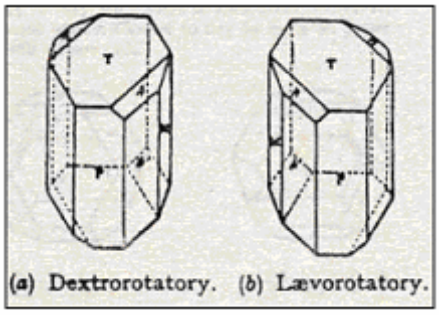

Figure 1*: Hemihedrism of quartz crystals.*

He successfully separated crystals of Na^+/NH_4^+ salts of (+) and (-) tartaric acid from a racemic (non-rotating) mixture. Soon enough in 1860, he stated that the ability to rotate polarized light by crystals and molecules originates from dissymmetry in the molecule itself, *i.e* the non-identity of the crystal or molecule with its mirror image. This makes the two acids enantiomorphous at the molecular level, or in other words enantiomers (*mer* being a Greek word meaning “part” and enantios means “opposite”). The rotation produced by the organic substances is a property of the individual molecules and may be therefore observed in solid, liquid and gaseous states.

Of prime importance in Pasteur’s work was to relate the chirality of a molecule to life. Pasteur stated that the molecular dissymmetry (now known as homochirality of life) originated from the dissymmetry of the cosmic forces. Indeed, tartaric acid found in wine lee is enantiopure because it is produced by a fermentation process while the one chemically synthesised is racemic.

After another thirty years, two scientists Van't Hoff and Le Bel independently proposed the idea that chirality is related to the presence of an asymmetric carbon atom, which is a C atom attached to four different types of atom or four different groups of atoms. They precisely stated the 3D arrangement by explaining the structure of a molecule containing a C atom with four linkages towards the corners of a regular tetrahedron ultimately giving two nonsuperposable *enantiomers* as shown below.

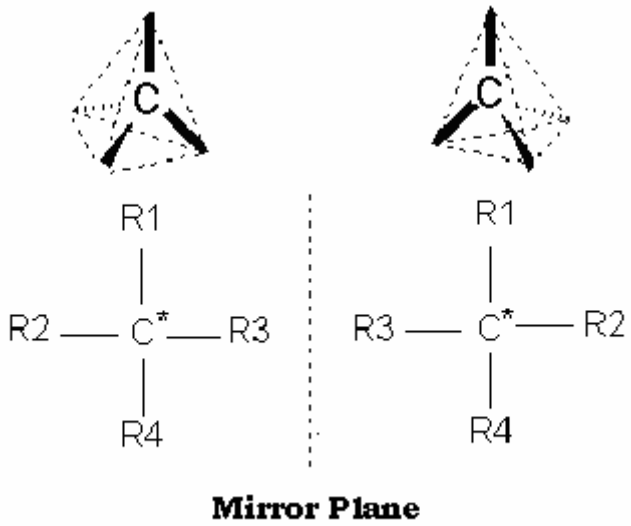

Figure 2*: Model showing two chiral molecules with a central asymmetric C atom and surrounded by four different groups/ atoms (R_1, R_2, R_3 and R_4), that are non-superposable on their mirror images*

The word *chirality* was first coined by Lord Kelvin who defined it in the following way in the year 1904 " I call any geometrical figure or group of points chiral, and say that it has chirality if its image in a plane mirror, ideally realized, cannot be brought into coincidence with itself ".

Later Cahn, Ingold and Prelog defined a molecule as chiral when it has no elements of symmetry except at most an axis of rotation. In 1951, the first experimental X-ray crystallography determination of the absolute configuration of any chiral molecule was achieved on the example of sodium rubidium double salt of (+)-tartaric acid.

I.3. Nomenclature[1]

The absolute configuration of a tetrahedral C atom can be determined by using the priority rule devised by Cahn-Ingold-Prelog (1951), abbreviated as the CIP chirality rule. The rule takes into consideration a chiral centre C with four substituents attached to it (a, b, d and e) following a priority order of a>b>d>e. The sequence is decided based on the following points:

i. Ligands of higher atomic number precede ligands of lower atomic numbers.

ii. In case of a trivalent atom e.g N or P, one of the substituents is a lone pair which is given the lowest priority (atomic number zero).

iii. When two or more atoms directly attached to the chiral centre are the same, one proceeds outwardly to the second atom and if needed to the third to come to a decision.

iv. The last rule is valid for isotopic substituents. For them, the higher atomic mass precedes lower atomic mass isotope.

Keeping the above sequences in mind, the CIP chirality rule can be followed only if the molecule is viewed towards the side occupied by the ligand of lowest priority (d in the given example). If the rest three ligands (a, b and c) follow a clockwise priority sequence, they are described as *R* (in Latin *rectus (R)* meaning right), and if an anticlockwise sequence they are termed as *S* (in Latin *sinister (S)* meaning left). An example is shown below in Figure 3.

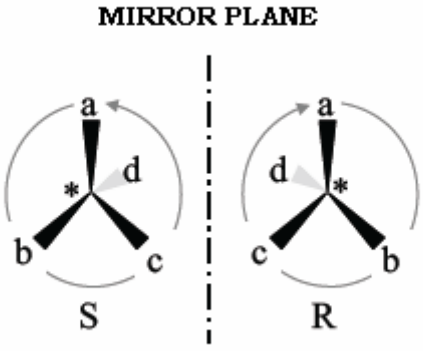

Figure 3: *Nomenclature of R and S.*

II. PROPERTIES OF ENANTIOMERS

II.1. Physical properties[1]

Pure enantiomers have identical physical properties except for their optical rotation, as they rotate the plane-polarized light by equal amounts in opposite directions. They contrast with diastereomers, which are characteristically different in their physical properties, such as melting point, boiling point, densities, solubilities, heats of formation and Gibbs free energies.

The observed angle of rotation of plane of polarization by an optically active liquid solution, or (more rarely) gas or solid is usually denoted by the symbol α. The angle may be either positive or negative depending on whether the rotation is clockwise, *i.e* to the right (dextro) or to the left (levo) as seen by an observer towards whom the beam of polarized light travels.

Biot discovered that the observed rotation is proportional to the length l of the cell or tube containing the optically active liquid or solution and the concentration c (or density in case of a pure liquid):

$$\alpha = [\alpha]\ c\ l \qquad \text{(Biot's law)}$$

The value of the proportionality constant depends on the units chosen; in polarimetry it is customary to express l in decimetres and c in g/mL.

$$[\alpha] = \frac{\alpha}{l(\mathrm{dm})\ c(\mathrm{gmL^{-1}})}$$

The value of [α], the specific rotation, depends on wavelength and temperature.

As it is not possible to tell the difference between α and 180°-α, two measures at least are necessary. Readings taken at two different concentrations almost always determine α unequivocally.

II.2. Chemical properties

Pure enantiomers have exactly the same chemical properties when they are in achiral environment. For example, they have the same solubility in non

chiral solvent or the same reactivity towards non chiral reactants. However, when two pure enantiomers are embedded in an environment which is chiral itself, they behave differently. This is precisely what is called chiral discrimination or chiral recognition. This phenomenon plays an important role in life-chemistry, in particular for the action of drugs because the receptors in the body are chiral too and interact in a different way with the two pure enantiomers of a chiral molecule. A commonly cited classic example is the chiral drug thalidomide, which was sold worldwide to pregnant women as a treatment for morning sickness from 1957-1962, and was responsible for the birth of over 10000 deformed babies. Thalidomide is chiral and was sold in its racemic form, despite the fact that only one of the pure enantiomers was the active drug. It was first thought that it was the other enantiomer which was harmful.

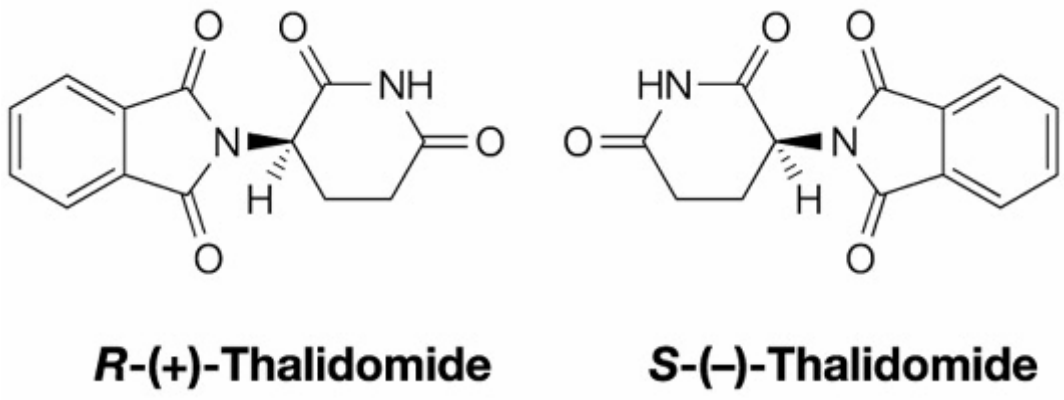

Figure 4: *The two enantiomers of thalidomide*

It was thus believed that the birth defects could have been avoided if thalidomide had been marketed as an enantiomerically pure substance, namely the (S) form, rather than a racemic mixture. However, even enantiomerically pure thalidomide racemizes *in vivo*, so that it is effectively impossible to administer just one form. Other examples encompass molecules related to the senses of smell and taste. For example the two pure enantiomers of limonene exhibit a different odour commonly known as orange aroma (*R* limonene) or the off odour of turpentine (*S*-limonene). These smell different because our olfactory receptors also contain chiral molecules that behave differently in the presence of different enantiomers.

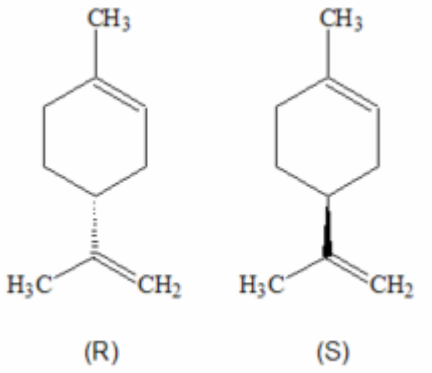

Figure 5*: The two enantiomers of limonene*

II.3. How do we obtain chiral molecules?

When a molecule is produced from non chiral substances by chemical synthesis, it is obtaind as a racemic mixture. It is possible to produce an enantiomeric excess of a chiral substance (in the order of a pure enantiomer) by asymmetric synthesis. Henry Kagan pioneered this work on asymmetric catalysis by stating that if the reactant is achiral, the chirality is introduced through a chiral catalyst[3]. The asymmetric catalysis reactions involving oxidation and hydrogenation processes were later developped by Nobel laureates of the year 2001 (William S. Knowles, Ryoji Noyori, K. Barry Sharpless). William S. Knowles and Ryoji Noyori exploited the transition metals (Rhodium) to form chiral catalysts utilised in hydrogenation reactions. The catalyst often acts by differentiating the two faces of a prochiral molecule, i.e. a molecule that can be converted from achiral to chiral in a single step. An example of prochirality is a ketone substituted by two different substituents, as illustrated by Figure 6.

Cinchona alkaloids akin to those which are presented in this thesis are commonly used as catalyst for the asymmetric hydrogenation of prochiral ketones, leading to asymmetric alcohols[4]. Assymmetric catalysis has tremendous importance in pharmacy, for example it helped in introducing the antiparkinsson medicine, L-Dopa in the pharmaceutical industry. K. Barry Sharpless had also developed the role of chiral catalysts in oxidation reactions.

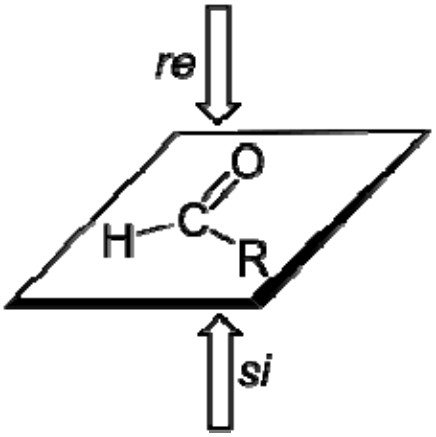

Figure 6*: The two different faces of a prochiral ketone*

II.4. Separation of enantiomers

It is sometimes possible to separate a pure enantiomer from a racemic enantiomeric mixture as initiated by Pasteur by manually separating the crystals of para-tartarate with the help of a pair of tweezers. This is the case when the enantiomers crystallize separately as distinct crystals. Other methods of separation are given below:

A common way of separation of enantiomers uses the conversion into diastereomers, which are not mirror images of each other. This is known as ***derivatisation***. For e.g, the two enantiomers *1*-Phenylethylamine (*S*-(-), *R*-(+)) are separated using (*L*)-(+)-tartaric acid (also known as the (*R,R*)-form) as resolving agent. The two salts formed possess different cation ions are therefore not enantiomers of each other anymore. The (*S*)-(*1*)-Phenylethyl ammonium-(*R,R*)-tartrate salt crystallizes faster than the (*R*)-(*1*)-Phenylethyl ammonium-(*R,R*)-tartrate salt.

Chromatographic methods [5] [6] [7] are used for the separation of a wide variety of chiral compounds. While enantiomers cannot be distinguished in achiral environments, such as a solvent system or by normal silica gel chromatography, they *can* be distinguished in chiral environments, such as in the active site of an enzyme, or in a chiral stationary phase of a column. In a chiral column, achiral silica gel (SiO_2) is converted into a chiral stationary phase by grafting a chiral molecule on it. Once the enantiomers that need to be separated are run down the column, one enantiomer will "stick" to the stationary

phase better than the other, and there will be separation. Chiral stationary phases built on cinchona alkaloids are very commonly used for the separation of amino acids among others [8]

Enantiomerically pure compounds have gained tremendous importance in the last decade which has in turn had an influence on the development and application of chiral chromatographic methods used industrially. These methods are based on specific interactions between the chiral stationary phase and the enantiomers to be separated. Since this interaction energy is of the order of thermal energy at room temperature, the contact pairs initiating chiral recognition are difficult to separate and study in solution.

III. CHIRAL DISCRIMINATION IN GAS PHASE

To a chemist, the difference in behaviour of the two enantiomers of a chiral molecule when interacting with a chiral environment can be explained in terms of weakly bound contact pairs involving specific interactions. However, these contact pair are short lived and difficult to study in solution. The advantage of studying chiral recognition in the gas phase is that the influence of the environment is not taken into account, which is not true in case of condensed phase[9].

The interactions can be classified into different components: repulsive, electrostatic interaction, polarization and dispersion.

The repulsive interactions: The non-penetration of electron cloud between of two molecules gives rise to a repulsive force between them. It is a short range force which decreases exponentially with increase in the intermolecular distance.

Electrostatic interactions: These interactions occur between molecules having permanent moments (charge, dipole, quadrupoles etc). These forces vary as $\mathbf{1/r^n}$, r being the intermolecular distance.

Polarization: These interactions exist between molecules having permanent and induced dipole moments. These forces are attractive in nature and exist at shorter range than electrostatic forces. They vary as **$1/r^6$**.

Dispersion: It is the weakest intermolecular force arising from induced instantaneous polarization in molecules. They can act in molecules without permanent moments and vary as **$1/r^6$**.

The dominant forces existing between neutral molecules are mostly electrostatic (hydrogen bond) and dispersive (e.g Van der Waals forces) in nature and those between an ion and a molecule mostly involve electrostatic forces.

III.1. Neutral complexes in a supersonic expansion

Chiral discrimination as observed in life chemistry rests on the formation of weakly bond diastereoisomers Rr and Rs complexes which cannot be observed at room temperature. Supersonic expansions allow overcoming this difficulty by stabilizing and isolating these complexes. The low temperature achieved in the jet, combined with the resolution (below 1 cm^{-1}) achieved by laser spectroscopy allows probing the structure of the diastereomer in detail leading to information at the molecular level on the forces responsible for chiral recognition.

The group I am working in has done extensive research in the enantiodifferentiation of jet-cooled chiral aromatic molecules in the gas phase for almost more than a decade. Their studies mainly involve the formation of Van der Waals complexes in the jet, which exhibit different spectroscopic features depending on the chirality of the complexing agent with respect to the chiral target molecule, thereby imitating the lock-and-key phenomena observed in chiral biomolecules.[10] [11,12]. The principle of the experiment is shown in Figure 7.

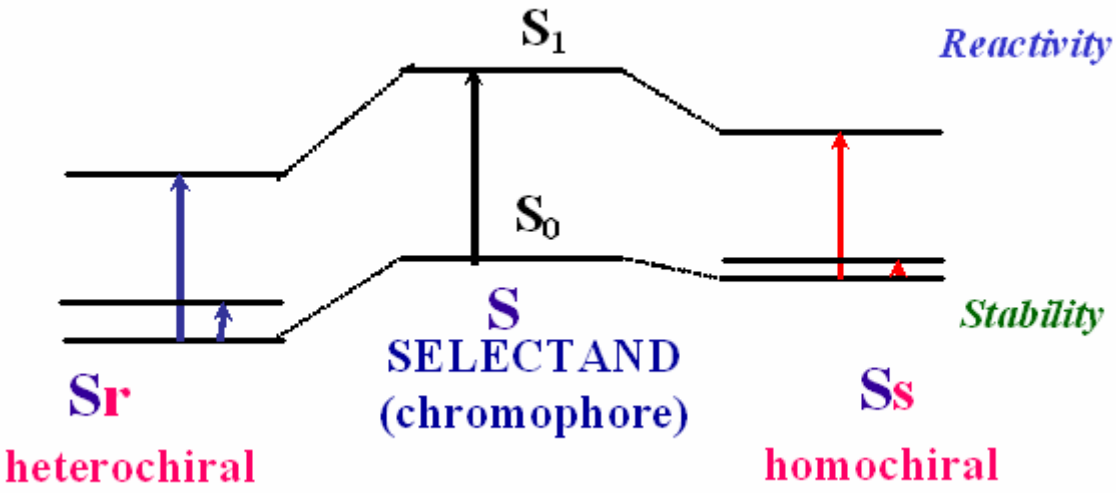

Figure 7*: Principle of the experiment*

The principle of the experiment rests on the formation of complexes between a chiral chromophore used as a selectand in its pure enantiomeric form, let's say S, with the two enantiomers of the species to discriminate. Complexation results to a shift of the energy levels, which is not the same for the Sr and the Ss complex owing to the selectivity of the interactions. This induces differences in the transition energies, for both the vibrational and electronic spectroscopy, which can be interrogated by laser spectroscopy.

Energetic studies on jet-cooled complexes are scarce. Binding energy measurements have been pioneered by Latini et al. on the 1-phenyl-1-propanol complexes[13]. They found out that the homochiral complex is stabilized relative to the heterochiral adduct by 4.6±1.7 kJ/mol in the ground state. Our group has also reported binding energy measurements of 1-phenyl ethanol and 2-butanol which have also shown a homochiral preference[14].

Understanding structure has been the objective of numerous studies. They have been performed using the techniques of optical spectroscopy. On combining supersonic expansion with electronic and vibrational spectroscopic techniques in conjunction with quantum chemical calculations one can gain information about the structure of weakly bound complexes of chiral molecules and the nature of interactions giving rise to chiral recognition. Few general spectroscopic methods used to decipher the intermolecular forces involved in the chiral discrimination process at the molecular level, are given below:

III.1.a. Electronic Spectroscopy

This technique is valid only for molecules containing an aromatic chromophore. In our experiment, we study a neutral cinchona alkaloid, Quinine, with Quinoline as the aromatic chromophore. We study the various diastereomers of Quinine using the following two techniques:

a) Laser induced fluorescence: This technique requires the presence of a fluorescent chromophore (Quinoline in our case) in the complex, to record the electronic spectra of aromatic molecules and chiral complexes. This method has been extensively used in our group for the past decade to study chiral discrimination.[15] [11] [16]

b) Resonance Enhanced Multiphoton Ionisation (REMPI): This spectroscopic technique coupled with a supersonic jet and time of flight mass spectrometry can record mass-resolved electronic spectra of chiral molecules or complexes.[17] In our case we have studied cinchona alkaloids in neutral form using this technique. The technique used in our experiment is based on a 2-colour-2-photon excitation scheme and has been described in detail in chapter 1.

III.1.b. Vibrational Spectroscopy

IR-UV double resonance:

In order to gain more information on the structure and energetics of large molecules the IR-UV double resonance technique has been used. For a molecule as large as the studied Quinine and its pseudoenantiomer, it allows gathering structural information which can be directly comparable to that obtained from quantum chemical calculation. However, this technique is also limited to molecules containing aromatic chromophores as the method is based on the depletion of ion signal or fluorescence signal by Infrared absorption. On the other hand, this is a very sensitive and selective technique and it will be illustrated in chapters 2 and 3.

Direct IR absorption

Suhm's group has used Fourier transform infrared spectroscopy (FTIR) to study the ν(OH) and ν(CO) stretch modes of the aggregates of simple molecules like methyl-lactate formed in supersonic jet. Unlike the ones described above, this technique does not require the presence of an aromatic chromophore. Hence it permits the study of simple aliphatic systems that are more accessible to theoretical chemistry calculations.[18] [19] [20] However, the spectra obtained by direct absorption contain the superposition of the absorptions of all species present in the jet.

Microwave studies.

Microwave spectroscopy is limited to fairly small systems. It has the advantage of providing structural information (moments of inertia) which can be directly comparable with quantum chemical calculations. In the field of microwave spectroscopy, Howard et al. characterized the rotational spectroscopy of the homochiral dimer of butan-2-ol[21]. Later, Xu et al. studied chiral recognition in model system like the methyloxirane dimer.[22]

III.2. Ionic complexes in an ion trap

Studies in ion traps complement the results obtained from those performed in supersonic expansion conditions. In contrast with supersonic expansion, ion traps are at room temperature and are often thought to be under thermodynamically controlled conditions.

The study of chiral recognition in an ion trap has been pioneered by Cooks and co-workers and consists mostly of the measurement of enantioselective dissociation energy by the so-called Cooks kinetic method[23]. In other words, the larger affinity of a chiral ion for one or the other enantiomer of a chiral molecule has been studied. There has been a great deal of studies done based on the relative abundance of diastereoisomeric ions[24], their collisional dissociation[25]or ion molecule reactions[26]. However, spectroscopic studies are rare. The only clear spectroscopic evidence of chiral recognition in ionic complexes has been reported by our group. [27]

IV. PRESENT WORK

The group I am working with applies various techniques to the study of chiral recognition in the gas phase. It has now turn its attention to molecules which contain several chiral centers, hence exhibit diastereoisomerism, like cinchona alkaloids. It also focuses on ionic systems, within the frame of a collaboration with Dr. Debora Scuderi of the Laboratoire de Chimie Physique (LCP Orsay)[27,28]. These two aspects have been the subject of my thesis.

Indeed, there are two types of stereoisomers, enantiomers and diastereomers. If two molecules have identical constitution but different spatial arrangement and are not mirror images to each other, they are known as diastereomers. While molecules containing one asymmetric carbon atom as the only chiral centre are always chiral and exist in two enantiomers, those containing two or more asymmetric carbon atoms are not always chiral. Moreover they often exhibit diastereoisomerism. The secondary structure of helical peptides represents an example for intramolecular chirality effects. It has been shown for example that changes in the chirality of one of the amino acids of a small peptide chain isolated in a supersonic expansion changes the sense of the helix.[29] The phenomenon is even more marked in charged species as studied in an ion trap. Dramatic chirality effects have been observed in the binding site of a cation to the LL and DL forms of a dipeptide containing two phenylalanine residues PhePhe which changes when the chirality of a residue is changed[30].

In this thesis, firstly I present the study of a system in which the differences between the stereoisomers are so minute that they are called “pseudo-enantiomers”, namely the pairs consisting of Quinine and Quinidine, and that consisting of Hydroquinine and Hydroquinidine. The study of these two pairs will be described in chapters two and three.

Next, in chapter four, I describe the energetic and spectroscopic aspects of chiral recognition in a simple ionic complex, namely, the protonated Camphor-Alanine complex.

V. REFERENCES

[1] E. L. Eliel. and S. A.Wilen., *Stereochemistry of Organic Compounds*. (John Wiley and Sons, Inc., 1994).

[2] Collet A, Crassous J, Dutasta J, and G. L., *Molécules chirales : Stéréochimie et propriétés*. (2006).

[3] H. Kagan, l'Actualité Chimique Nov-Dec 2003, 10 (2003).

[4] N. M. Maier, S. Schefzick, G. M. Lombardo, M. Feliz, K. Rissanen, W. Lindner, and K. B. Lipkowitz, Journal of the American Chemical Society 124 (29), 8611 (2002); T. Burgi and A. Baiker, Accounts of Chemical Research 37 (11), 909 (2004).

[5] W. H. Pirkle and T. C. Pochapsky, Chemical Reviews 89 (2), 347 (1989).

[6] R. G. Lodevico, D. R. Bobbitt, and T. J. Edkins, Talanta 44 (8), 1353 (1997).

[7] D. R. Bobbitt and S. W. Linder, TrAC Trends in Analytical Chemistry 20 (3), 111 (2001).

[8] M. Lammerhofer and W. Lindner, Journal of Chromatography A 741 (1), 33 (1996).

[9] *Chiral recognition in the Gas Phase*, edited by A. Zehnacker (CRC Press Taylor & francis Group, Boca Raton, 2010); A. Zehnacker and M. A. Suhm, Angewandte Chemie-International Edition 47 (37), 6970 (2008).

[10] A. R. AlRabaa, K. Le Barbu, F. Lahmani, and A. Zehnacker-Rentien, Journal of Photochemistry and Photobiology A-Chemistry 105 (2-3), 277 (1997).

[11] K. Le Barbu, V. Brenner, P. Millie, F. Lahmani, and A. Zehnacker-Rentien, Journal of Physical Chemistry A 102 (1), 128 (1998).

[12] F. Lahmani, K. Le Barbu-Debus, N. Seurre, and A. Zehnacker-Rentien, Chemical Physics Letters 375 (5-6), 636 (2003); N. Seurre, K. Le Barbu-Debus, F. Lahmani, A. Zehnacker-Rentien, and J. Sepiol, Journal of Molecular Structure 692 (1-3), 127 (2004); N. Seurre, K. Le Barbu-Debus, F. Lahmani, A. Zehnacker, N. Borho, and M. A. Suhm, Physical Chemistry Chemical Physics 8 (8), 1007 (2006).

[13] A. Latini, D. Toja, A. Giardini-Guidoni, S. Piccirillo, and M. Speranza, Angewandte Chemie-International Edition 38 (6), 815 (1999).

[14] M. Mons, F. Piuzzi, I. Dimicoli, A. Zehnacker, and F. Lahmani, Physical Chemistry Chemical Physics 2 (22), 5065 (2000).

[15] A. R. AlRabaa, E. Breheret, F. Lahmani, and A. Zehnacker, Chemical Physics Letters 237 (5-6), 480 (1995).

[16] K. Le Barbu-Debus, F. Lahmani, A. Zehnacker-Rentien, N. Guchhait, S. S. Panja, and T. Chakraborty, Journal of Chemical Physics 125 (17), 174305 (2006); K. Le Barbu-Debus, M. Broquier, A. Mahjoub, and A. Zehnacker-Rentien, Journal of Physical Chemistry A 112 (40), 9731 (2008).

[17] A. Giardini-Guidoni, S. Piccirillo, D. Scuderi, M. Satta, T. M. Di Palma, and M. Speranza, Physical Chemistry Chemical Physics 2 (18), 4139 (2000).

[18] N. Borho, T. Haber, and M. A. Suhm, Physical Chemistry Chemical Physics 3 (11), 1945 (2001).

[19] N. Borho and M. A. Suhm, Physical Chemistry Chemical Physics 4 (12), 2721 (2002).

[20] N. Borho and M. A. Suhm, Organic & Biomolecular Chemistry 1 (23), 4351 (2003).

[21] A. K. King and B. J. Howard, Chemical Physics Letters 348 (3-4), 343 (2001).

[22] N. Borho and Y. Xu, Physical Chemistry Chemical Physics 9 (32), 4514 (2007).

[23] W. A. Tao and R. G. Cooks, Analytical Chemistry 75 (1), 25A (2003).

[24] Y. J. Liang, J. S. Bradshaw, and D. V. Dearden, Journal of Physical Chemistry A 106 (42), 9665 (2002).

[25] W. A. Tao, F. C. Gozzo, and R. G. Cooks, Analytical Chemistry 73 (8), 1692 (2001).

[26] M. Speranza, F. Gasparrini, B. Botta, C. Villani, D. Subissati, C. Fraschetti, and F. Subrizi, Chirality 21 (1), 69 (2009).

[27] D. Scuderi, K. Le Barbu-Debus, and A. Zehnacker, Physical Chemistry Chemical Physics 13 (40), 17916 (2011).

[28] D. Scuderi, P. Maitre, F. Rondino, K. Le Barbu-Debus, V. Lepere, and A. Zehnacker-Rentien, Journal of Physical Chemistry A 114 (9), 3306 (2010).

[29] V. Brenner, F. Piuzzi, I. Dimicoli, B. Tardivel, and M. Mons, Angewandte Chemie-International Edition 46 (14), 2463 (2007).

[30] R. C. Dunbar, J. D. Steill, and J. Oomens, International Journal of Mass Spectrometry 297 (1-3), 107 (2010).

CHAPTER I

Experimental and Theoretical methods

INDEX

List of figures

The experiments that we have done in gas phase combine supersonic expansions with laser spectroscopy. The latter includes both electronic spectroscopy (resonance enhance multiphoton ionisation, laser-induced fluorescence) and vibrational spectroscopy (fluorescence dip spectroscopy).

I. PRINCIPLE OF SUPERSONIC EXPANSION

All our experiments in the gas phase rest on the use of a supersonic expansion, which allows obtaining cold and isolated molecules as well as weakly bound complexes which would be destroyed at room temperature.

A gas enclosed in a chamber at a temperature T_1 and pressure P_1 is in a disordered state with its atoms constantly in collision, either with each other or with the walls of the enclosure that contains them. The average distance travelled by an atom between two collisions is defined as the mean free path (λ_0). Due to this erratic motion the velocities of the atoms are distributed randomly in all directions in space and in a very broad Maxwell-Boltzmann distribution.

However, it is possible to transform this chaotic motion into a more ordered state in the form of a molecular jet. The jet is produced by expansion of free gas from a zone of high pressure P_0, called stagnation pressure, to an area of low pressure P_1 through a nozzle of diameter D where: $\lambda_0 << D$. The flow through the nozzle then converts the disordered movement into an ordered translational motion along the axis of the nozzle. The flow may reach sonic velocity at the exit of the nozzle if the ratio P_0/P_1 exceeds a certain threshold critical value[1]:

$$G = \left(\frac{\gamma+1}{2}\right)^{\frac{\gamma}{\gamma-1}} \qquad \text{Eq. 1}$$

G is less than 2.05 for all gases (γ being the ratio of the specific heat capacities C_p/C_v at constant pressure and volume, respectively). If the P_0/P_1 ratio is less than G, the flow is subsonic and the pressure at the nozzle exit is close to P_1. If the ratio is greater than G, the jet becomes supersonic and the pressure at the collision zone is independent of P_1 and is P_0/G.

During the adiabatic expansion process the molecules moving faster collide with the slower ones thereby decelerating the former and accelerating the latter.

Hence this results in a narrow velocity distribution. Such being the case, at low temperatures the relative velocity between the molecules is low unless they collide with the walls of the vacuum chamber. However, there always exists a non-zero residual pressure in the vacuum chamber (P_1) due to some residual gases present inside the vacuum chamber and they are constantly shoved away by the expanding molecules. This results in the formation of a barrier of closely packed molecules, called a ***Mach disk***. It is the edge of the cold zone, beyond which a large number of collisions occur between atoms and molecules, thereby hindering the cooling process.

The supersonic jet is composed of various zones as shown in Figure 1.

I.1. The collision zone

The collision zone is located at the exit of the nozzle (1-2 mm). The cooling of molecules and the formation of complexes occur precisely in this zone. During a two-body collision, the carrier gas takes away the internal energy from the molecules of interest in the form of kinetic energy.

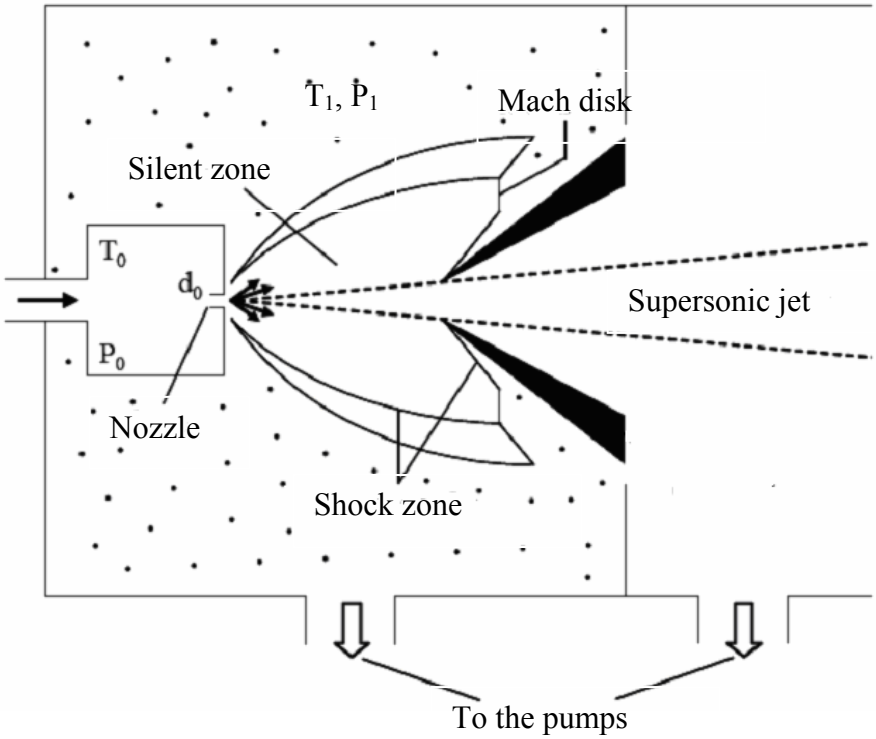

Figure 1 *Diagram of a skimmed supersonic jet*

After undergoing collision, the molecules are said to be "cold", with temperature in the range of few Kelvin therby indicating that only the lowest

vibrational level (v"=0) and few rotational levels of the electronic ground state are populated[2]. In a similar three-body collision, the carrier gas makes the formation of a complex possible by carrying away the binding energy in the form of kinetic energy.

The molecules under study are often seeded in the carrier gas at a concentration of a few percents, by evaporating the solid sample contained in an oven prior to the expansion. In our experiment we introduce a plume of ablated molecules directly in the collision zone, in some sort of pick up process, the details of which are explained later.

I.2. The silent zone

It is the isentropic region between the nozzle and the Mach disk, which cannot be penetrated by the residual gas atoms in the chamber. Here, the isolated molecules move with the same velocity and in the same direction. It is in this zone that spectroscopic studies take place. It is possible to skim the silent zone (see Figure 1) to take its most internal hence coldest part. In our studies, we have used an un-skimmed molecular beam.

I.3. The jet boundary

The zone where the atoms of carrier gas enter into collisions with the residual gas molecules/atoms present inside the vacuum. This boundary layer protects the zone of silence.

I.4. The Mach disk

It is the outer limit of the zone of silence located at X_M distance from the nozzle.

The distance from the nozzle to the Mach disk, X_M, is expressed by:

$$X_M = 0.67D\sqrt{\frac{P_0}{P_1}} \qquad \text{Eq. 2}$$

Where, P_0 and P_1 are the pressures of the gas in the nozzle and in the vacuum chamber, respectively and D is the diameter of the nozzle.

In the case of experiments with P=1x10^{-3} mbar, P_0= 5bar, and D=100 μm, X_M is calculated to be 15 cm. However, one has to keep in mind that this calculation is strictly valid for a continuous jet and that the above value of X_M is an upper limit of the true value.

II. THE VALVE

The valve used in the experiment is a commercially available General Valve working with 28 V voltage. It consists of an electromagnet which is a solenoid wrapped around a soft Iron magnet. The tip of the magnet contains a spring and a poppet made of teflon. Finally they are covered by a metallic flange with an orifice of diameter in the range of a few 100 μm, through which the molecules go out. In our case, the diameter of the valve is usually 100 μm.

When a current is applied to the solenoid, a magnetic field is produced which pulls the magnet along with the spring and the poppet and opens the valve. There is a delay of about 450 μs between the current applied to the valve and the actual moment at which it opens. This delay is due to the mechanical inertia of the valve. The opening duration of the valve is about 250 μs and is adjusted on the signal intensity. This parameter is of much greater importance with the laser ablation source than the heated source.

More details about the sequencing of the valve and lasers will be given later on.

III. PRINCIPLE OF THE LASER ABLATION SOURCE

The molecules under study are put intact in the gas phase by means of a laser ablation source. The desorbed molecules intersect the carrier gas atoms close to the nozzle, in the collision zone, which allows them to be substantially cooled down.

The term “desorption” is defined as the transition from the condensed phase to the gas phase and is said to occur on the outermost surface of the

former. Although it's a thermal process, one should not confuse it with the term "vaporization" wherein a *bulk* of sample is heated into gas phase. The same transition when caused non-thermally is known as laser ejection or ablation. To be more precise, an ablation process involves pulsed removal of a volume of sample from a substrate (matrix) when mixed homogeneously with it[3,4].

Figure 2 gives a clearer picture of the difference between the two processes: while (a) depicts the thermal desorption of a thin film adsorbed on a substrate, (b) shows the non-thermal ejection of multiple layers from a matrix at one laser pulse.

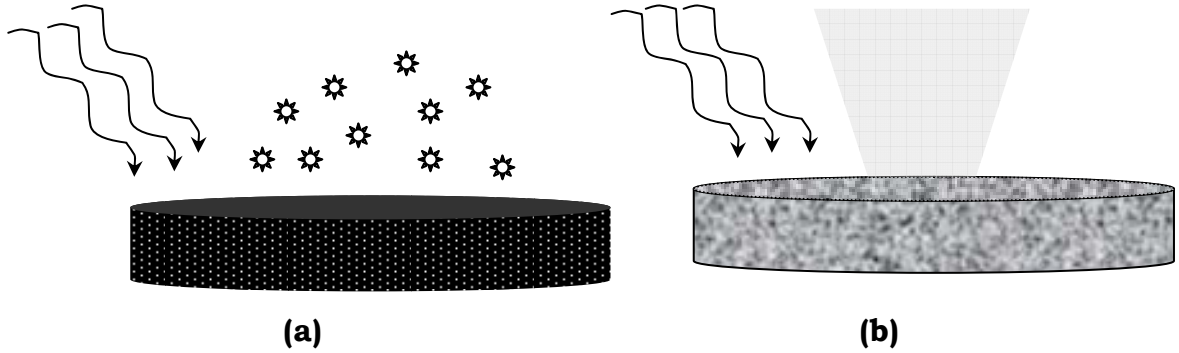

Figure 2 *Schematic representation of (a) Thermal laser desorption of a substrate; (b) Non-thermal laser ablation of a homogeneous substrate-adsorbate mixture[4].*

In our experiment, the main motive is to trap the molecule of interest, in its neutral form, before it decomposes. When a sample is heated there are higher chances of decomposition, as the whole surface containing the sample is continuously exposed to the heat, even after it has already vaporized. The advantage of using the techniques of laser desorption and ablation is that they occur much faster than thermal decomposition.

This can be explained a little more in detail by looking at the activation energy barriers for decomposition (E_{react}) and desorption (E_{des}) processes. The kinetic picture can be explained by the Polanyi-Wigner model, which explains the rate of desorption and decomposition of an adsorbate by simple Arrhenius rates:

$$\frac{d[\theta]_{des}}{dt} = [\theta]^{n}_{ads} . \nu_{des} . \exp\left[- \frac{E_{des}}{RT} \right]$$

Eq. 3

$$\frac{d[\theta]_{react}}{dt} = [\theta]^{n}_{ads} . \nu_{react} . \exp\left[- \frac{E_{react}}{RT} \right] \qquad \text{Eq. 4}$$

The above equations **Eq. 3** and **Eq. 4** (as given by Levis)[4] depict the rate of desorption and rate of decomposition respectively with ν_{des}, ν_{react} being the frequency factors and E_{des}, E_{react} being the activation energy barriers for the two processes and $[\theta]^{n}_{ads}$ being the adsorbate coverage. Generally speaking, when both E and ν are larger for desorption than for decomposition, desorption dominates at higher temperatures. Thus fragmentation can be minimized by a high heating rate.

The fact that even if the temperature of the sample-substrate interface increases the fragile molecules are ablated mostly intact, can also be explained from the bottleneck model as explained by Zare & Levine[5]. According to them, the main reason behind the said process is the difference in frequencies between the vibrational modes of the surface-adsorbate bond and the intramolecular vibration of the adsorbate, which results in a bottleneck in the Intramolecular Vibrational Redistribution (IVR) process. Thus a rapid laser-induced desorption can cleave the surface-adsorbate bond in spite of the presence of weaker bonds in the free molecule. The laser excites the phonons of the surface, which are roughly in resonance with the frequency of the bond between the adsorbate and the surface, but not with that of the vibration mode of the adsorbate. The intramolecular modes are poorly coupled to those of the surface; the adsorbate remains therefore unexcited. This is why it is possible to obtain desorbed cold molecules. The kinetic equation for energy transfer through the surface-adsorbate bond:

$$\frac{dE(t)}{dt} = \frac{dE_0(t)}{dt} - kh\nu\{\exp[E(t)/h\nu] - 1\} \qquad \text{Eq. } \mathbf{5}$$

where $dE_0(t)/dt$ is the rate of energy gained by the adsorbate-substrate bond when energy is not transferred to the intramolecular modes. The second term on the right hand side contains the rate constant k for energy transfer from the surface-adsorbate mode of frequency ν to the molecule. The second term is also known as the “loss term”.

As E (t) << hν, equation **Eq.** 5 is approximated by

$$\frac{dE}{dt} = \frac{dE_0(t)}{dt} - kE(t) \qquad \text{Eq. 6}$$

Desorption is achieved when E_0 reaches the adsorbate-substrate bond dissociation energy D. This condition is met at time τ. Integration of the above equation at time τ gives the following result:

$$E(\tau) = D(1 - k\tau) \qquad \text{Eq. 7}$$

Thus the higher is the adsorbate-surface bond dissociation energy, the greater is the probability of energy flowing into the adsorbate molecule. However, if the time (τ) required for $E_0(t)$ to reach the bond dissociation energy is very small ($k\tau<1$) then the above equation becomes:

$$E(\tau) = D \qquad \text{Eq. 8}$$

From the above equation it can be said that the criteria to desorb an atom bound to the surface with the same dissociation energy as the molecule is given by

$$k\tau \langle 1 \qquad \text{Eq. 9}$$

which explains why fast heating is required.

The rate constant k for the energy transfer from surface-adsorbate vibrational modes to intramolecular modes can be expressed as:

$$k = \nu \exp(-\xi) \qquad \text{Eq. 10}$$

Where ξ is the adiabaticity parameter $\xi = 2\pi\left(\nu/\nu'\right)$ which relates the desorption efficiency to the mismatch between the intra and intermolecular frequencies.

Hence from equations **Eq. 9** and **Eq. 10** we can write the following equation:

$$\nu\tau < \exp(\xi) \qquad \text{Eq. 11}$$

Thus it can be concluded that, for an energy transfer from one vibrational mode, such as the surface adsorbate bond with frequency ν, to an internal vibrational mode in the adsorbate having frequency ν', the mismatch of the

vibrational frequencies and the time allowed for energy transfer is mandatory to obtain good desorption efficiency.

IV. WORKING

The ablation source is made out of a single piece of metal block with a hole dug at the top to fit in the mouth of the General Valve containing the nozzle opening at its centre. It is also attached to a mount which holds the pellet which is to be ablated. The ablation laser beam is sent through an optical fibre. The scheme of the ablation source is shown in Figure 3. The ablated molecules are made to enter the jet close to the nozzle and are cooled down in some sort of a pick-up process. They then travel downstream carried away by the expansion before they reach the zone where they interact with the laser. This travel induces a delay between the ablation laser and the spectroscopy laser, which depends on the speed of the jet and hence on the nature of carrier gas. It is of the order of 10 to 20 µs.

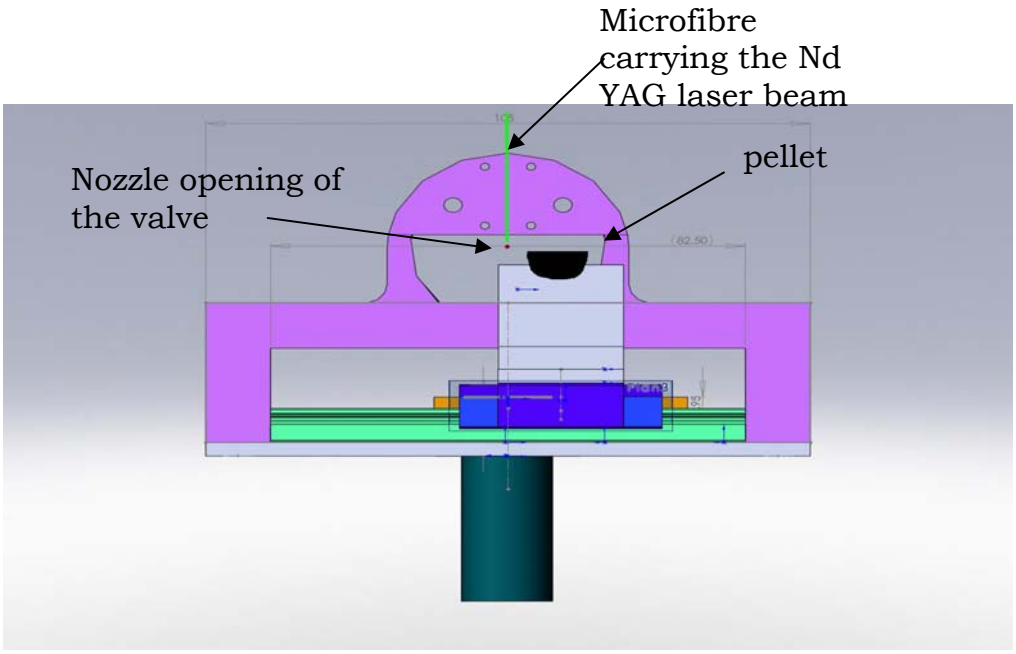

Figure 3 *The laser ablation motor with the pellet and the fibre transferring the ablation laser.*

The laser beam of ~2 mm diameter is focused on the pellet by a telescope fed into a multimode optical fibre of diameter 600 µm, 3 m length, and 70%

transparency. Both the end of the fibre and the face of the pellet containing the sample are placed about 0.5 mm from the valve nozzle.

The pulse energies required for sufficient ablation to occur was around 5mJ/pulse. The fibre is made to pass through one of the flanges of the vacuum chamber through a modified Swagelok connection through a hole of 1mm diameter. Hence the laser coming out of the fibre directly hits the flat edge of the pellet in order to yield the maximum ablation.

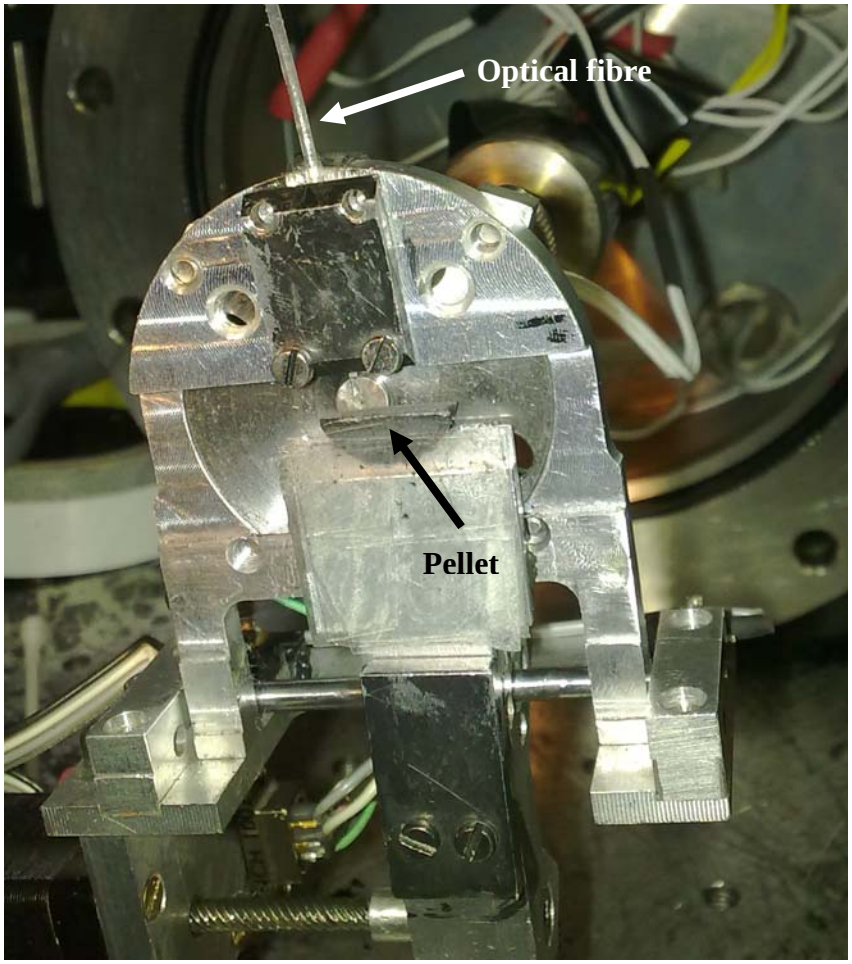

Figure 4: *A digital image of the laser ablation motor.*

The pellet being used is actually a homogeneous mixture of finely powdered carbon (~25%) and the sample (~75%). Carbon is chosen as it is unreactive, and apolar; as a dark substance it absorbs light in a wide range. The mixture is pressed (~ 3.5 tonnes) into a pellet of approximately 1cm diameter and 2 mm width using a die and a hydraulic press. Before pressing, the two constituents of the mixture are manually ground in a mortar and pestle. The round pellet is cut

into two halves and the edges of each semicircle are filed neatly so that the entire cross-section of the laser beam falls on it.

However, in order to use the same pellet for a long time, it was imperative to move the face of pellet laterally so that the laser gets to hit a fresh layer each time[6]. This was achieved by using a motor attached to the mount of the pellet. The motor having a voltage of 12V was able to move the pellet back and forth across the face of the nozzle and at high speed. With the help of a remote control we could operate the motor. With medium laser power we could use a single pellet for almost 5 hours, after which we had to file the edge.

After using this ablation source for a period of time we could detect that the following modifications were required to improve it:

a) The closer we keep the pellet to the nozzle the higher are the chances to obtain a bigger ablation plume. However, doing so the laser can damage the pellet faster too.
b) The faster is the translational speed of the motor, the lesser is the noise on the excitation signal. On other words the slight inhomogenities in the pellet are neglected.
c) The distance between the nozzle and the pellet is crucial to obtain a cold supersonic expansion. Indeed, injecting the ablated plume too far from the nozzle prevents the molecules from being cooled down, because the plume meets the carrier gas in the cold zone instead of the collision zone. The ideal value is of the order of 1mm in our experimental conditions.

However, the cooling efficiency is not as good as with a simple seeded jet, in particular for large floppy molecules like Quinine. For this reason, He cannot be used as a carrier gas; we usually resorted to Ar or Ne which is even better. It has to be noted that the cooling efficiency depends on the studied molecule; it is for example better for the test molecule S-Naproxen than for Quinine. On the other hand, there exist several ablation regimes which can be introduced by changing the delay between the desorption and ionization lasers. A change in delay might result in the probed zone to shift to the end of the ablation plume. Indeed, increasing the delay results in probing the end of the ablation plume which could correspond to a different ablation regime, with much smaller velocity of the ablated species hence warmer species as depicted by Focsa's group.[7]

V. ELECTRONIC SPECTROSCOPY

When a molecule is excited from the lowest vibrational level of the electronic ground state to the lowest vibrational level of the excited electronic state, it corresponds to the lowest-energy electronic transition of the molecule. This electronic transition is known as the band origin. All other transitions starting from the ground electronic state to the different vibrationally excited levels of the excited electronic state are called vibronic bands as they involve vibrational excitation in the electronic excited state. As will be discussed later on in the results section, these vibronic bands are allowed either if they possess non negligible Franck Condon activity or if they are made active by Hertzberg-Teller coupling. Electronic spectroscopy has been studied in our experiment using the following two techniques:

V.1. Resonance Enhanced Multiphoton Ionisation (REMPI)

This a procedure by which one can study the mass-selected electronic absorption spectrum of different species present in the supersonic jet.

It is a combination of two consecutive steps. The first photon promotes the molecule from the ground electronic state to an excited vibronic state (S_0-> S_1), followed by another photon to ionise the molecule (S_1-> D_0), as shown in **Figure 5**

The probability of ionisation is enhanced by the fact that the first photon is resonant with an intermediate excited electronic state of the molecule. In our case, the two photons come from two different lasers because the S_1-> D_0 energy is larger than the S_0-> S_1 energy. The excitation dye laser (SIRAH) is tuned in a range of wavelength near the S_0-> S_1 transition of the molecule while the fourth harmonic of a Nd:YAG laser (BMI Industrie) (wavelength of 266 nm) ionises the molecule from the excited electronic state. Since the excited-state life time of the studied molecule Quinine is very short, around 10 ns, the two lasers have to be synchronised in a way that the delay between the two lasers is less than 10ns.

Also, it is crucial to maintain the fluence of the ionisation laser as low as possible so as to avoid ionisation by two photons at 266 nm.

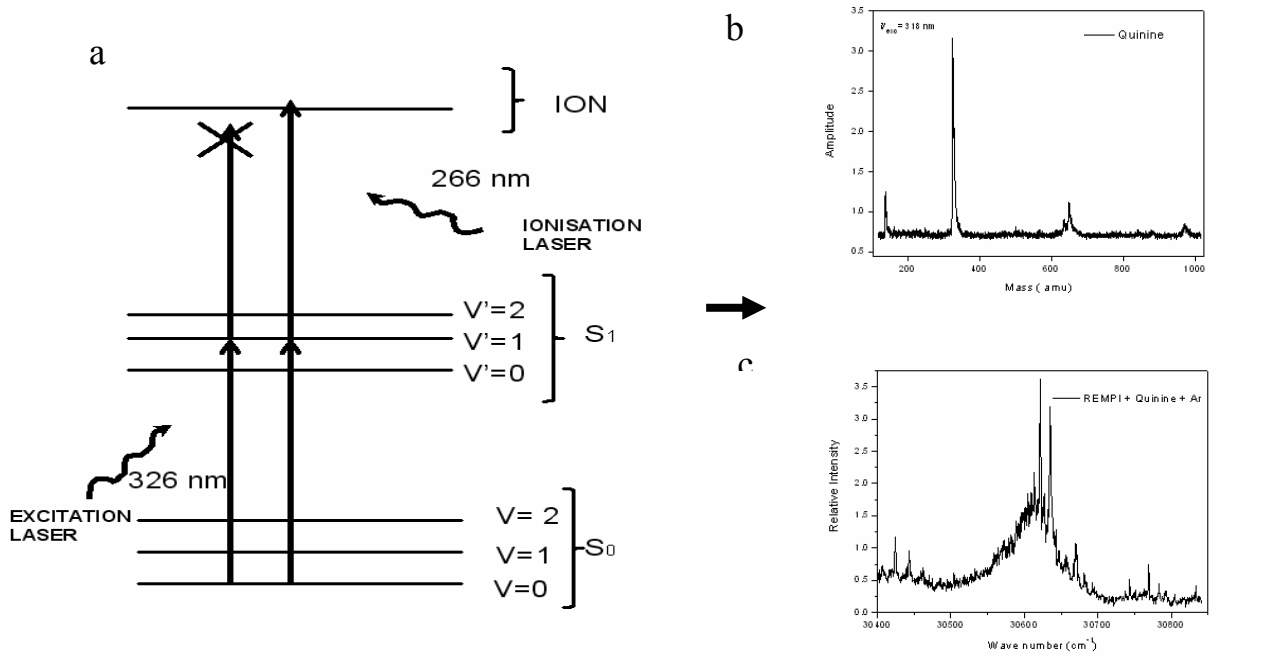

Figure 5 *(a) Energy level diagram of 2-colour-2-photon resonance-enhanced ionisation scheme.*

(b) Example plot of mass spectrum showing an intense peak corresponding to the mass of Quinine.

(c) Example plot of REMPI spectrum taken at the mass of Quinine with respect to wavelength scanned.

As shown in Figure 6, the species present in the supersonic jet perpendicularly cross the lasers and are ionised between the two electrodes E_1 and E_2, the ion-source region of a linear time-of-flight mass spectrometer (RM Jordan, Wiley-McLaren type). The repeller electrode, E_1 is about 2000V, while the electrode E_2 is set to about 1800V. This difference in voltage allows extraction of the newly-formed cations. The acceleration voltage between E_2 and E_3, being 10 times larger than that between the E_1 and E_2, accelerated the extracted ions into the flight tube. The accelerated ions moving with an initial velocity of the supersonic jet will gradually try to drift from the axis of the flight tube. Hence to counteract this, two steering plates X in a direction parallel to the supersonic expansion with potential V_x are introduced to repel the drifted ions back onto the desired course.

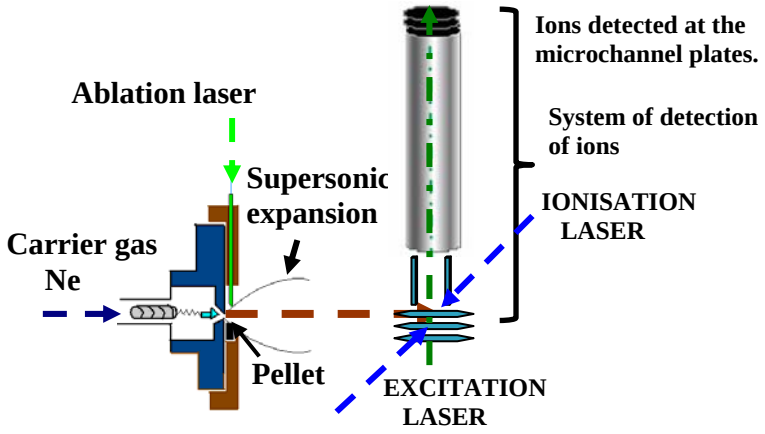

Figure 6 *The set up of the Time of Flight Mass Spectrometer coupled with supersonic expansion*

Then, the ions of mass m travel through a tube free of electric field with a velocity v, the flight tube, of length d. Doing so, they keep the kinetic energy E they have gained during the extraction-acceleration stage.

Hence the energy of the ions inside the flight tube is given by

$$E = \frac{1}{2}mv^2 \qquad \text{Eq. 12}$$

which when solved for v looks like:

$$v = \sqrt{\frac{2E}{m}} \qquad \text{Eq. 13}$$

Hence ions with lower masses arrive at the detector earlier than the heavier ones. In order to measure the time t taken by an ion to reach the detector, which is called the time of flight (TOF), we combine **Eq. 13** and v=d/t to yield.

$$m = \left(\frac{2E}{d^2}\right)t^2 \qquad \text{Eq. 14}$$

Eq. 14 is the basic time of flight relationship. The design of the mass spectrometer is such that d is fixed by the length of the TOF tube and E is given by the voltage applied on the electrodes, thereby giving

$$m = At^2 \qquad \text{Eq. 15}$$

where A is defined by the apparatus used.

To compensate for inhomogeneous fields and other experimental artifacts, it is necessary to correct the measured time, t_m by subtracting a delay of t_0, such that:

$$m = A(t_m - t_0)^2 \qquad \text{Eq. 16}$$

After their travel through the flight tube, the ions reach a detector made from microchannel plates (MCP).

When the ions are impinged on the microchannel plates (RM Jordan, 25 mm), electrons are liberated, which undergo further collisions thereby leading to an amplification of 10^3-10^6. The current obtained can be measured easily by a fast digital oscilloscope (Lecroy wavesurfer).

As the ions reach the detector with a TOF characteristic of their mass, mass-selective electronic absorption spectra are acquired by setting narrow time gates on the signal visualised on the oscilloscope, matched to the flight time through the spectrometer. The ion signal is then monitored as a function of the excitation photon wavelength by the above-mentioned oscilloscope and a personal computer.

In order to convert measured flight time,t_m, to mass, the values of A and t_0 must be determined, hence a calibration has to be done. To do that we have used toluene clusters.

Calibrant compound	Mass(amu)	Flight Time(μs)
Monomer of Toluene	92.14	18.2
Dimer of Toluene	184.28	25.7

Hence with the above known values of mass the computer which receives data from the instrument calculates A and t_0. It uses non-linear regression to find out values of A and t_0 such that the two sides of **Eq. 16** match closely for the given data.

The temporal scheme of the lasers used in the REMPI experiment is given in Figure 7. The delay between the opening of the valve, the ablation laser, and the lasers used for spectroscopy is controlled by a computer-controlled home-made digital gate generator (G.I.N.I).

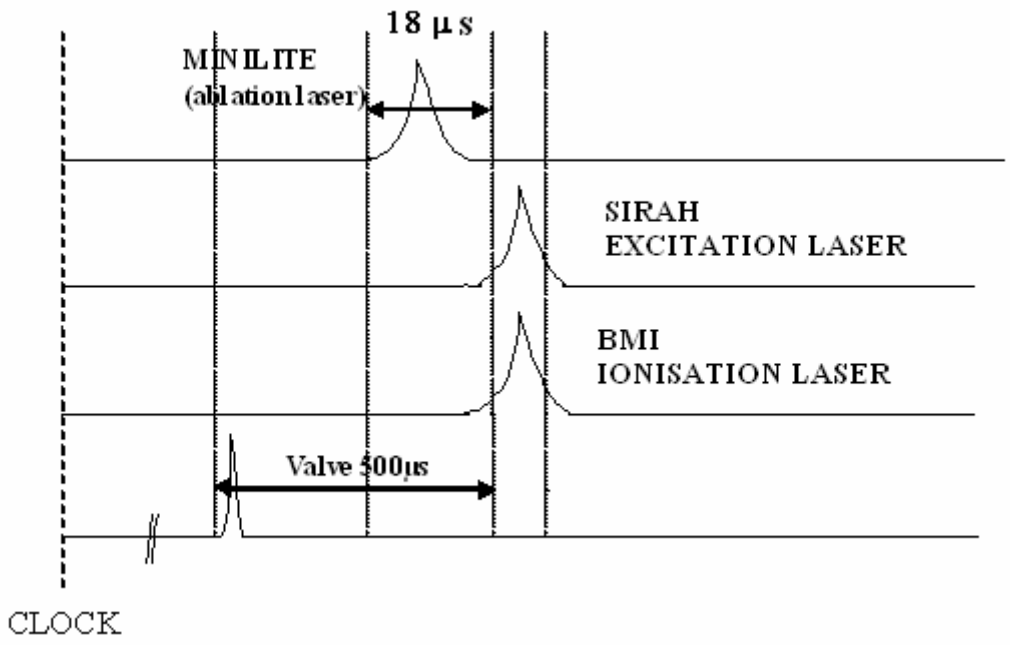

Figure 7 *Temporal scheme for REMPI experiment.*

V.2. Laser Induced Fluorescence Spectroscopy

V.2.a. Laser Induced Fluorescence Excitation

It is a technique to record the absorption spectra corresponding to the electronic transition of S_0 (v"= 0)→ S_1(v'=0 to n), limited to fluorescent molecules.

To achieve this we vary the wavelength of the excitation laser around the band origin and record the global fluorescence emission due to radiative decay of the molecule from excited state S_1 to the ground state S_0. This way we gather information about the active vibrational levels of the excited electronic state. The action spectrum obtained thereby is identical to the absorption spectrum convoluted by the fluorescence quantum yield Q_f. For molecules with Q_f high enough, it is identical to that observed by 2-colour 2-photon REMPI experiments (Figure 8 (a) and (b))

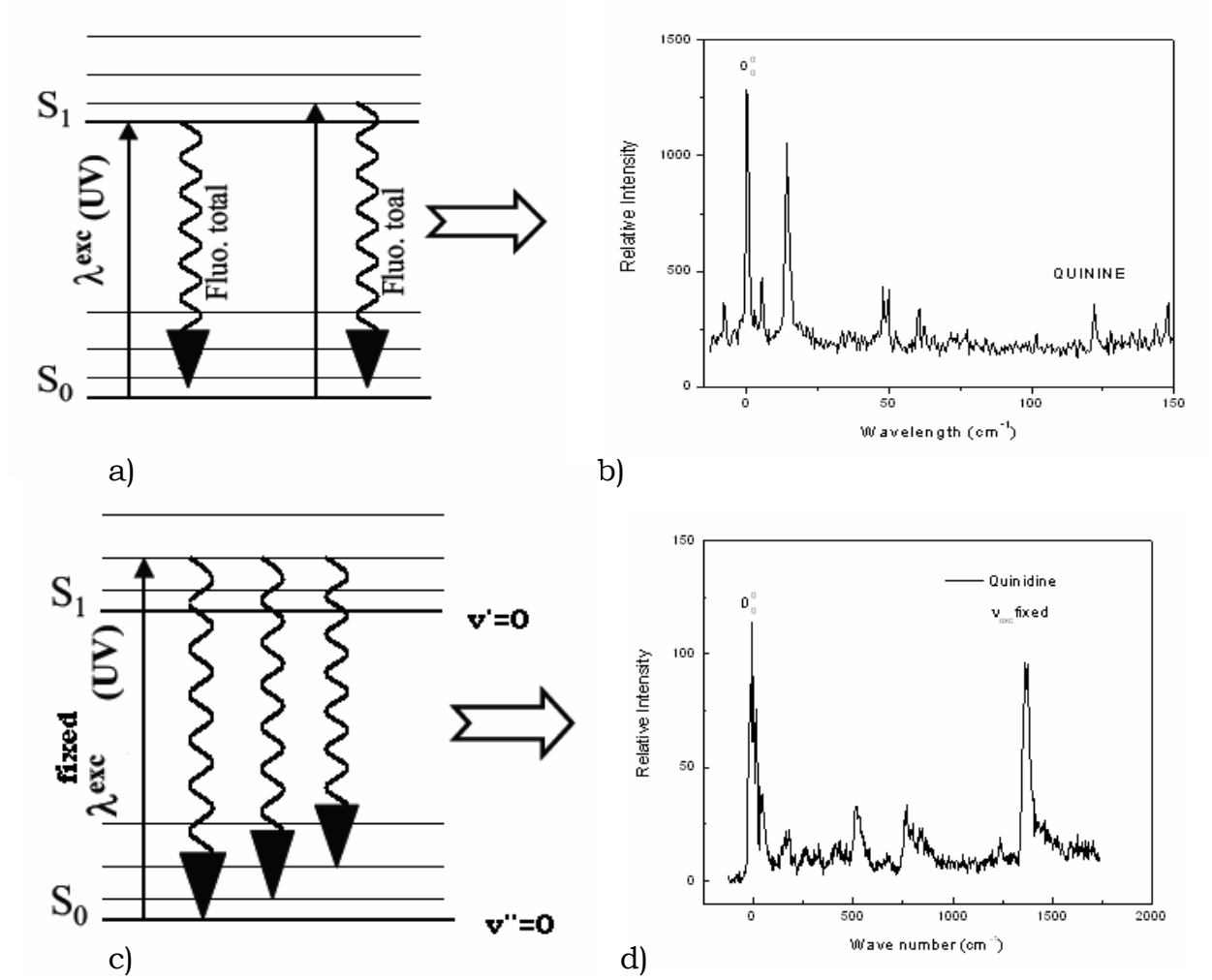

Figure 8 *(a) Energy level diagram of global fluorescence emitted after an electronic excitation.*

(b) is a plot of the emitted fluorescence intensity as a function of the excitation wavelength.

(c) is an energy level diagram of dispersed fluorescence obtained from excitation of a fixed wavelength, (d) being its example plot.

(d) is an example of a plot showing dispersed fluorescence emission intensity with respect to wavelength emitted.

V.2.b.Fluorescence Life-time

The fluorescence life-time of a molecule in excited state can be measured from the rate of fluorescence decay after a sufficiently short laser pulse. Since the decay curve follows an exponential function the fluorescence life time can be easily calculated from it. In our experiment the life time of Quinine in excited electronic state is within the laser pulse (10 ns) and cannot be measured.

V.2.c. Dispersed Fluorescence Emission

Here the excitation laser is fixed to an electronic transition corresponding to S_0 (v"= 0)→ S_1(v'= 0 to n). The fluorescene emission from the S_1(v'=n) state is then dispersed by a diffraction grating of sufficient resolution to obtain the energies corresponding to the excited vibrational levels of the ground electronic state S_0. (Figure 8 (c) and (d)). The emission spectra give information on the vibrational levels of the electronic ground state.

V.2.d. Fluorescence Detection

The Doppler effect, which results in a broadening of the bands can be avoided by having the axis of propagation of the molecules perpendicular to the axis of the laser and that of detection. In addition, to minimize background signal and noise due to stray light, the axis of detection is kept perpendicular to the axis of the laser. Hence the axes of the laser, the axis of the jet and that of detection are perpendicular to each other (Figure 9).

For the fluorescence excitation spectra, a photomultiplier (PM) Hamamatsu R2059 along with a 25 cm monochromator (Huet M25) used as a broad band filter has been used to collect the global fluorescence (the bandwidth of the monochromator is approximately 30 nm).

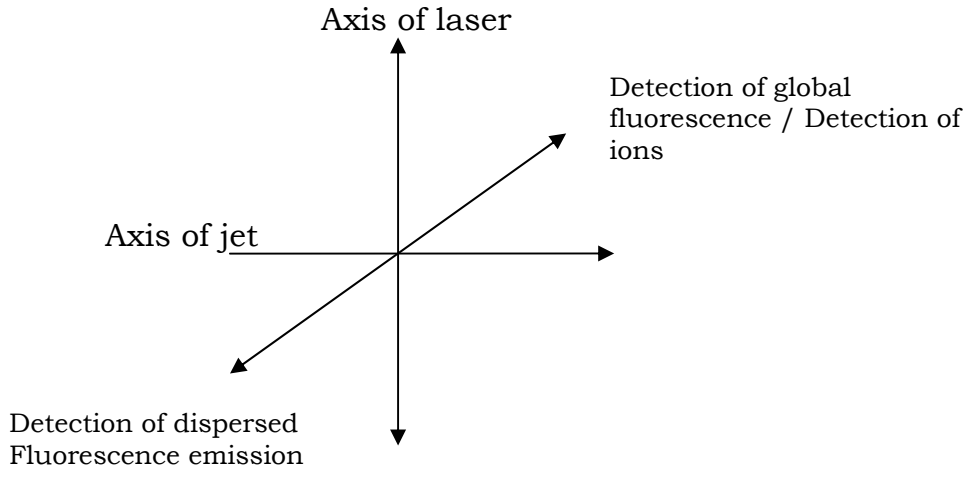

Figure 9 *The perpendicular arrangement of the jet axis, axis of laser and the axis of detection*

The emission spectra have been obtained in two different ways: first, we have defined the emission range by using the 25 cm monochromator under broad band conditions. This allows defining the resonant or Stokes-shifted character of the emission. Than we have used a higher resolution monochromator (Spectra-Pro) of 1200g/mm grating equipped with a CCD camera (Intensified Charge Coupled Device) Andor Technology (1024 x 256 pixels of 26 μm^2). This allows determining the vibrations of the ground state.

VI. IR-UV DOUBLE RESONANCE VIBRATIONAL SPECTROSCOPY

For studying the vibrational spectroscopy of the jet-cooled species the IR-UV double resonance technique was used[8].

It uses two lasers:

- The pump laser which scans in the mid-infrared region, from 4000 to 2800 cm^{-1} in a continuous manner.
- The probe laser is in the ultraviolet range, fixed on the band origin S_0 (v"=0)→ S_1(v'=0) or any intense band of the studied molecule.

The intensity of the fluorescence induced by the probe gives us a measure of the population of the probed species. The IR laser is scanned in the region of the ν(OH) and ν(CH) stretch modes. When the IR laser is resonant with a vibrational transition arising from the same ground state as that being probed by the UV laser, a decrease in the fluorescence signal is observed. When the frequency of infrared laser $h\nu_{IR}$ is not in resonance with a vibrational transition, the population of the state pumped remains unchanged and the fluorescence emission induced by the probe is constant (Figure 10).

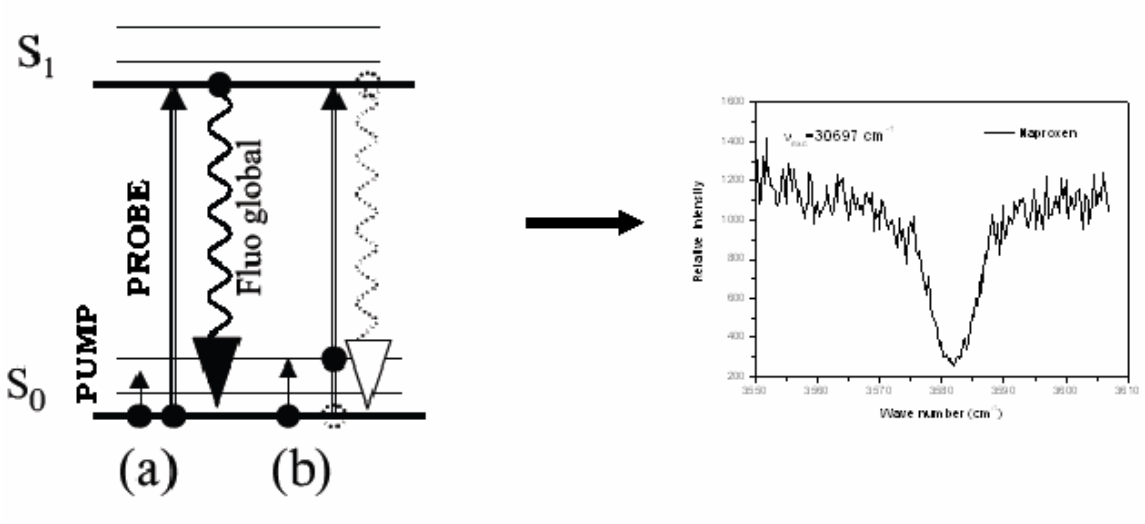

Figure 10 *Energy level diagram of IR-UV double resonance technique:*
(a) shows a IR radiation with $h\nu_{IR}$ not in resonance with any vibrational level of S_0.
(b) shows a IR radiation with $h\nu_{IR}$ in resonance with a vibrational transition, thereby leading to a dip in fluorescence emission.
(c) shows an example plot with depletion intensity with respect to the wavelength (IR) scanned .

When the IR laser is in resonance with a vibrational transition, it induces depletion of the ground state thereby decreasing the fluorescence intensity. By recording the fluorescence intensity as a function of the IR wavelength one records the IR spectrum as a series of dips. The IR laser can be fired either before the UV laser, depleting the ground state or after the UV laser (within the life-time of the excited state), depleting the excited state.

Here we analyze the spectroscopy of the ground state, by firing the IR laser shortly before the UV laser (50 to 80 ns).

As mentioned earlier, the ablation source we use in our experiment is not as stable as a source resting on a heated sample. We must correct the signal for the modifications in intensity of the source. The IR laser is therefore pulsed at half the frequency (5 Hz) to that of UV. A mechanical chopper is introduced to interrupt the IR laser at successive laser pulses. Hence we can monitor the effect of IR by measuring the difference between two successive UV pulses, one without and one with the IR present.

While co-propagating the two laser beams care is taken so that the two laser beams approach each other in an almost parallel manner and superimpose in a line, in order for the superimposition to be optimal. On the other hand,

depletion is more complete if the section of the UV laser beam is smaller than the IR laser beam, so that all probed species have been pumped by the IR. We have introduced iris on the UV laser and adjusted the focal conditions to achieve this. The two lasers are focused by a 500 mm focal length lens on the cold region of the supersonic expansion. They enter the vacuum chamber through a calcium fluoride window.

Last, we sometimes attenuated the power of the lasers to avoid saturation of the electronic or vibrational transition.

VII. LIGHT SOURCES

VII.1. Dye laser

In our experiment, we use a commercial dye laser (Sirah) pumped by a Nd^{3+}: YAG laser pulsed to 10 Hz (Spectra Physics) with a Q-switch provided by a Pockels cell. The dye is chosen according to the range of wavelength absorbed by the molecule of interest. In this experiment we have used DCM dye mixed with a little of LDS 698 (Pyridine), which emits between 620 nm and 670 nm using the second harmonic (532 nm) of the YAG for pumping.

The laser consists of a Littman-type oscillator (grazing-incidence grating), a preamplifier, and an amplifier. The visible laser obtained has a pulse of 10 ns and possesses a spectral resolution 0.02 cm^{-1}. The frequency is doubled by a non-linear crystal of KDP (Potassium Phosphate Dihydrogen KH_2PO_4) mounted on an adjustable angle tuner. It is used to obtain a tuneable light in the near ultraviolet range to which the absorption spectrum of the studied molecule belongs. The tuner is connected to a home-made computer-controlled device (P.O.L.O) which moves the crystal in order to optimise phase matching. Finally the frequency doubled beam is passed through a filter (UG11) which allows the wavelength in the UV region to pass through it and discards the fundamental. The resolution of the UV is 0.02 cm^{-1}.

VII.2. Optical parametric oscillator

The optical parametric oscillator is based on the parametric interaction of a strong pump wave $E_p \cos\left(\omega_p t - \vec{k}_p.\vec{r}\right)$ with a nonlinear crystal. It splits up a pump photon $\hbar\omega_p$ into 2 photons, $\hbar\omega_s$(signal) and $\hbar\omega_i$(idler), which satisfy the conservation of energy and momentum at every point in the nonlinear crystal. (Figure 11)

$$\omega_p = \omega_i + \omega_s$$
$$k_p = k_i + k_s$$

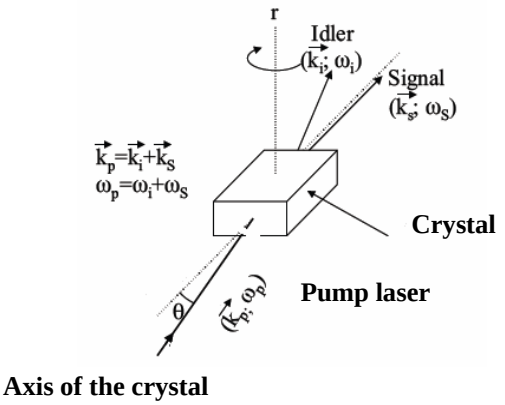

Figure 11 *Principle of OPO*[2]

The tunable IR source is a tabletop IR Optical Parametric Oscillator/Amplifier (OPO/OPA) (LaserVision).

The parametric system shown in Figure 12 is an integrated, multi-stage nonlinear device designed to convert the fixed-frequency output of an unseeded Nd:YAG laser into tunable radiation in the mid infrared. Using the combination of a 532 nm pumped OPO and a 1064 nm pumped OPA, the system will produce an output that is tunable from 710 to 885 nm and from 1.35 to 5 μm using a single set of nonlinear crystals. In our experiment we use the latter to study the region of the ν(OH), ν(NH) and ν(CH) stretch modes. All OPO and OPA crystals are controlled through a Microsoft Windows^{tm} based program running on a dedicated personal computer.

The power is slightly optimized at each wevelength range (ν(CH) or ν(OH) stretches) by optimizing the position of the crystals of the OPA. The power utilized to pump ν(CH) modes were 8.5-11 mJ per pulse and that of ν(OH) modes were 11-13 mJ per pulse. The resolution of the IR OPO is 3 cm^{-1}.

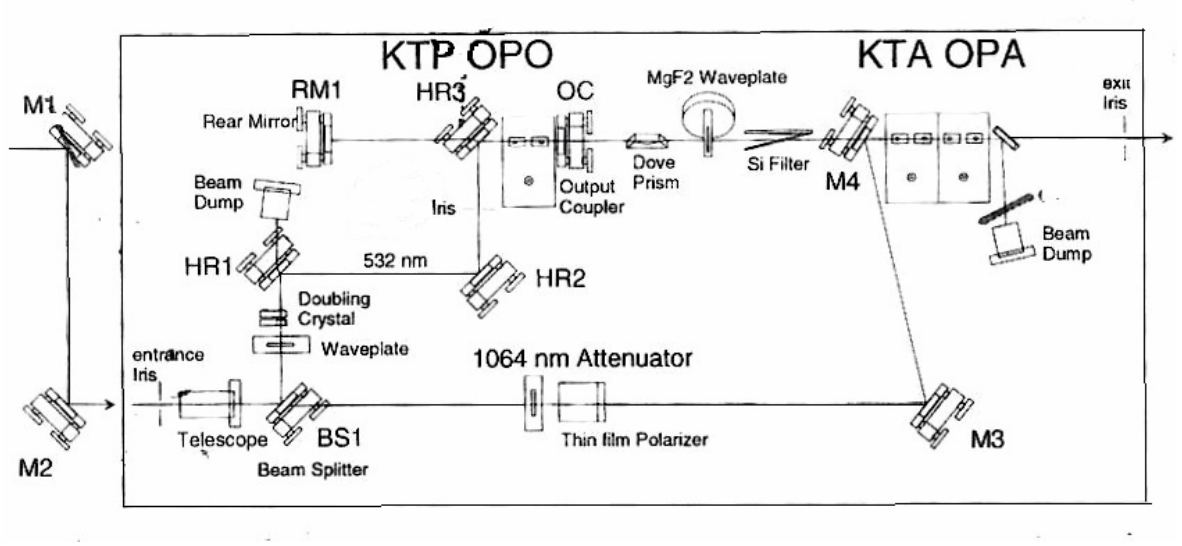

Figure 12 *Layout of the LaserVision Parametric Oscillator and Amplifier used in this work.*

A crucial part of IR-UV double resonance experiment is to maintain the optical path of the infrared laser so that it is well superimposed with the UV probe. A diode laser has been used to mimic the path of the infrared laser. The first step is to aligne this diode laser with the UV laser. For that purpose, a mirror with a movable shaft has been introduced. Its purpose is to reflect the image of the point where IR and UV are co-focused on the cold region of the jet outside the vacuum chamber, on a very small aperture iris (200 μm). This way one can make sure of the overlap of the two lasers inside the vacuum chamber without actually opening the chamber itself. The first round of alignment consists in aligning the diode and the UV lasers. Then the IR is made to follow exactly the same path as the diode laser, by checking the superpositon of the two beams along the whole optical path well defined by irises, by means of a pyroelectric detector. When removing the retractable mirror mentioned above, the IR must superimpose with the UV exactly at the middle of the vacuum chamber.

The temporal scheme of the lasers used in the IR-UV fluorescence experiments are given in Figure 13.

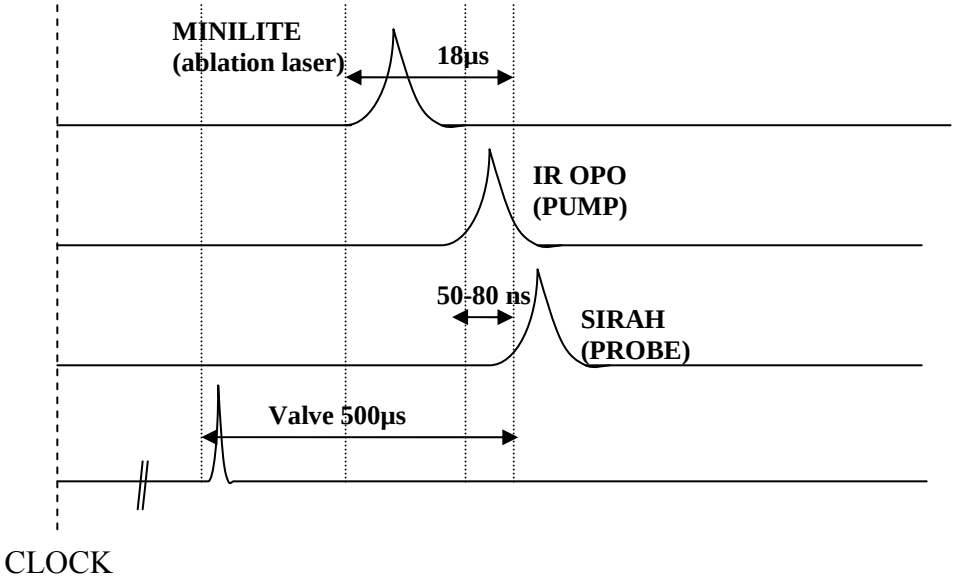

Figure 13 *Temporal scheme of IR-UV Experiment*

VIII. VIBRATIONAL CIRCULAR DICHROISM

The experiments in the gas phase have been complemented by experiments in solution which rest on vibrational circular dichroism spectroscopy.

Vibrational Circular Dichroism (VCD) is one of the methods which measure the chiroptical properties of a chiral molecule in the infra-red wavelength range. Using this technique, one can combine the rich structural content of vibrational spectroscopy with stereochemical sensitivity of an optically active sample[9].

Vibrational circular dichroism is basically the difference in absorption of left and right circularly polarised infrared radiation by a chiral molecule (Figure 14), i.e

$$\Delta A = A_L - A_R \qquad \text{Eq. 17}$$

where A is the absorbance of a VCD active mode, with $A_{L,R}$ being that of left and right circular polarized light, respectively.

Or, in terms of molar extinction coefficient ε the above equation can be written as, $\Delta\varepsilon = \varepsilon_l - \varepsilon_R$ where $\varepsilon = Acl$, c and l being the concentration and length of the cell containing the sample.

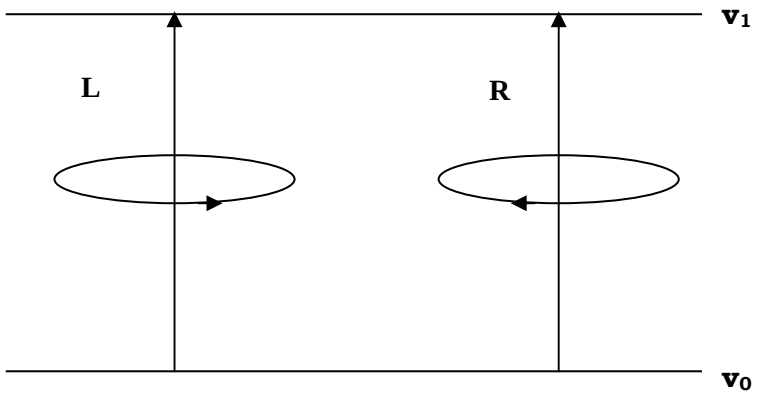

Figure 14 *Scheme of the vibrational transition involved in VCD* [10].

The goal of a VCD experiment is to measure the anisotropy ratio, g, defined as,

$$g = \frac{\Delta A}{A} = \frac{\Delta \varepsilon}{\varepsilon} \qquad \text{Eq. 18}$$

While ε, the absorbance of the molecule, is always positive $\Delta\varepsilon = \varepsilon_l - \varepsilon_R$ can take both positive and negative values.

The magnitude of g is in the order of 10^{-3} to 10^{-6}. This is why it is extremely delicate to measure.

VIII.1. Principle

The intensity of an IR transition corresponding to the normal mode Q_a is given by its transition moment:

$$D_{01}^{a} = \frac{\hbar}{2\omega_a}\left|\left(\frac{\partial\vec{\mu}}{\partial Q_a}\right)_0\right|^2 \qquad \text{Eq. 19}$$

Where μ is the electric dipole transition moment.

A mode is said to be infra-red active if the vibration involves a change in electric dipole moment with respect to the coordinates, *i.e*,

$$\left(\frac{\partial\vec{\mu}}{\partial Q_a}\right)_0 \neq 0 \qquad \text{Eq. 20}$$

Similarly, the rotational strength of a vibrational mode is given by:

$$R_{01}^{a} = \frac{\hbar}{2i\omega_a}\left(\frac{\partial\vec{\mu}}{\partial Q_a}\right)_0 \cdot \left(\frac{\partial\vec{m}}{\partial Q_a}\right)_0 \qquad \text{Eq. 21}$$

where m is the magnetic dipole transition moment

A mode shows optical activity if its oscillator strength is not zero. Therefore, a mode is said to be VCD active if the following points are true:

- $\left(\frac{\partial\vec{\mu}}{\partial Q_a}\right)_0 \neq 0$
- $\left(\frac{\partial\vec{m}}{\partial Q_a}\right)_0 \neq 0$
- and $\vec{\mu}$ and $\vec{m}$ are not orthogonal to each other. This is true only for chiral molecules. Moreover the sign and magnitude of a VCD signal depends on the direction and magnitude of the electric and magnetic dipole moment vectors

VIII.2. Experimental Setup

The experiments rest on the use of a standard FTIR spectrometer (Bruker Vertex 70) combined with a module allowing polarization of the light and detection of the circular dichroism. In what follows, we won't describe the FTIR apparatus which is standard, but we will shortly describe the VCD module.

As circular dichroism spectroscopy involves the use of polarized light, we will shortly recall the main concepts of polarization of light.

Polarisation of light

An electromagnetic wave is said to be *polarised* when the direction of its electric field vector E, which oscillates perpendicularly to the propagation axis, is well specified. When E oscillates along a single axis, the radiation is said to be *linearly polarised*, and if it follows a circular revolution during one period of vibration, it is known to be *circularly polarized*.

A linearly polarized light wave can be described as the sum of two equally intense components, one left circularly polarized and the other right-circularly polarized.

How do we modify the polarisation ?[11]

When a linearly polarized wave at an angle of 45° to the optic axis, passes through a birefringent material, like a block of silica, it suffers a retardation induced by the difference in refractive index ($n_x \neq n_y$) along the x and y axes. Hence,

$$\begin{aligned}\vec{E} &= E_x\vec{u}_x + E_y\vec{u}_y \\ &= E_{ox}\cos(kz-\omega t)\vec{u}_x + E_{yo}\cos(kz-\omega t+\phi)\vec{u}_y \end{aligned} \qquad \text{Eq. 22}$$

where ϕ is the *retardation* introduced, $\vec{u}_x$ and $\vec{u}_y$ are the unit vectors along x and y directions respectively.

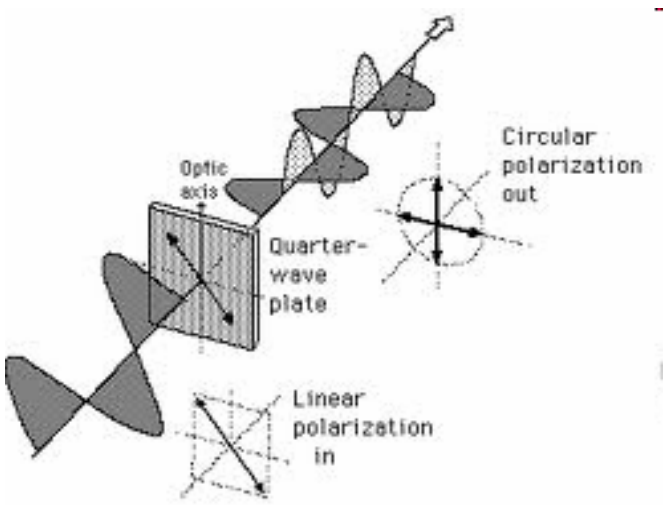

Figure 15 *Generation of circularly polarised light from linearly polarised light*

As shown in Figure 15, when the x-component of the resultant polarized light wave is retarded by λ/4 relative to the y component, it becomes right circularly polarized (RCP). Similarly if it is retarded by - λ/4 it generates the left-circularly polarized light wave (LCP).

Bruker VCD Spectrometer

The layout of the BRUKER VCD spectrometer is shown below in Figure 16:

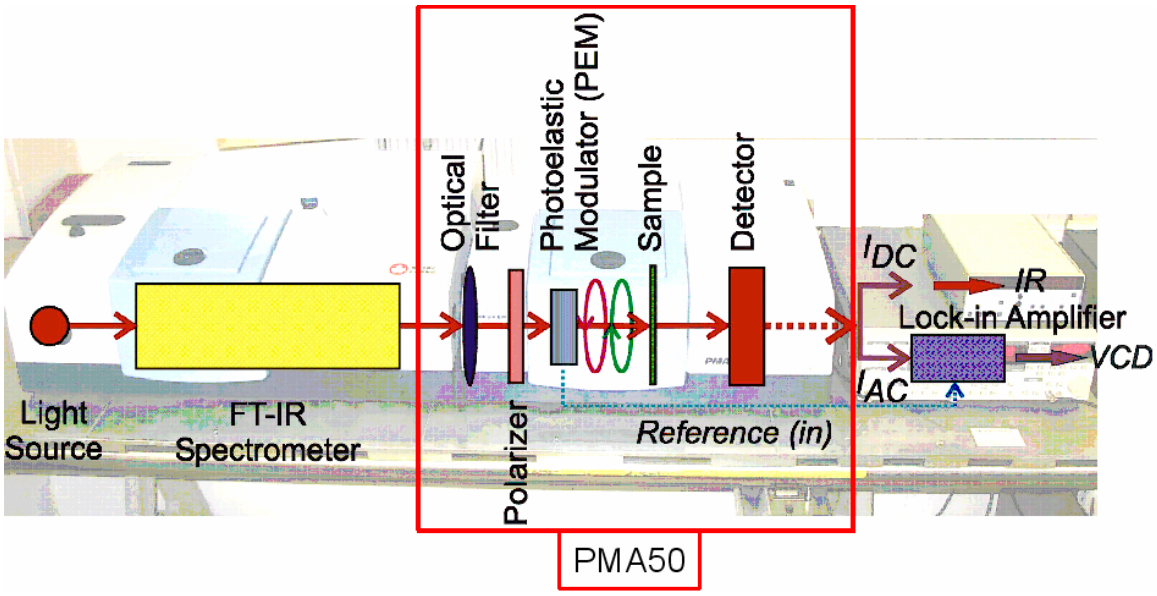

Figure 16 *Block Diagram of a VCD Spectrometer.*

Light from an unpolarised high-energy source of ceramics type enters the BRUKER PMA 50 module which is a dedicated instrument meant for polarization-modulation IR spectroscopy. The non polarized light is first made to pass through a linear polarizer. This allows producing light with linear polarization. The optical axes of the polarizer are set at an angle of 45° from the vertical, so that the polarization of the produced light is vertical. As we shall see later, the polarizer is set on an adjustable rotation stage which allows slightly varying this angle. Next the vertical linearly polarized light enters the photoelastic modulator, which transforms it into an oscillating left and right circularly polarised light which will pass through the sample. The photoelastic modulator contains an optical element, a birefringent BaF_2 crystal, in contact with a block of quartz which acts as a piezoelectric driver when excited into its natural oscillation frequency (~ 50 kHz).

After the infrared radiation is differentially absorbed by the sample, it is focused on a liquid-nitrogen cooled photovoltaic HgCdTe(MCT) detector .

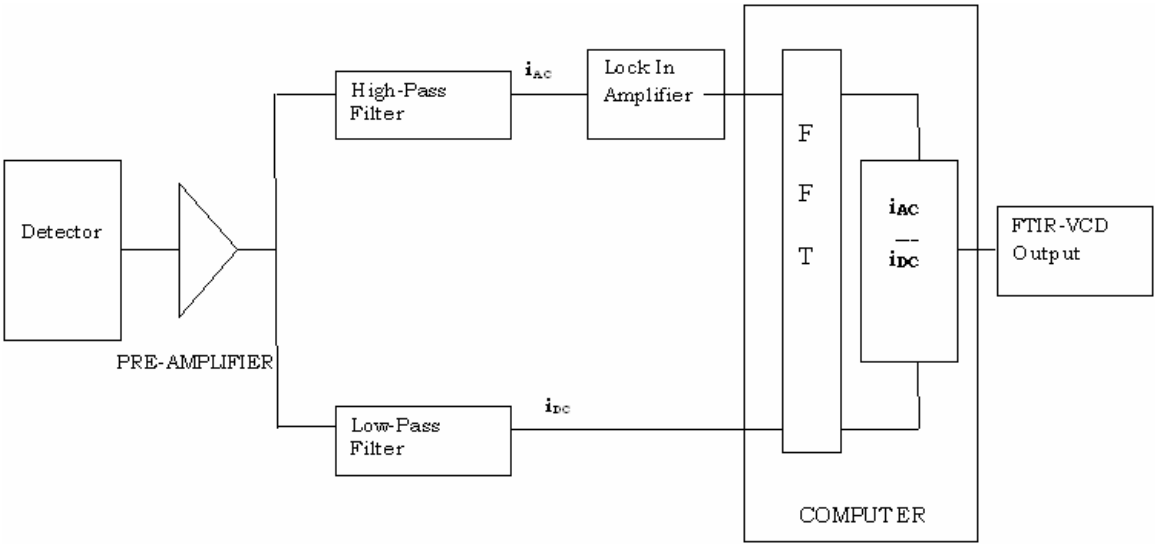

Figure 17 *Block diagram of the Electronic part of a VCD spectrometer*[12].

As shown in Figure 17 the electronics used to process the detected signal involves a pre-amplifier, a lock-in amplifier and low and high pass filters. The lock-in amplifier allows the output signal of the detector to be split into two parts by multiplying it with a cosine function, at the so-called detection frequency ω_r as follows:

$$V_{out} = \frac{1}{2}\left(\cos[(\omega_r + \omega_s)t + \phi] + \cos[(\omega_r - \omega_s)t + \phi]\right) \qquad \text{Eq. 23}$$

100 kHz signal Continuous signal

where ω_r and ω_s are the frequencies of detection and excitation respectively and V_{out} is the output voltage.

In the lock-in amplifier we use, $\omega_s = \omega_r$, which simplifies the above equation to a separation between a signal at frequency $2\omega_s$ (100 kHz) from a continuous signal.

The 100 kHz signal oscillates rapidly and is proportional to the total infrared absorption. This signal is filtered by an electronic filter with a very narrow band-width centered at a frequency of $2\omega_s$.

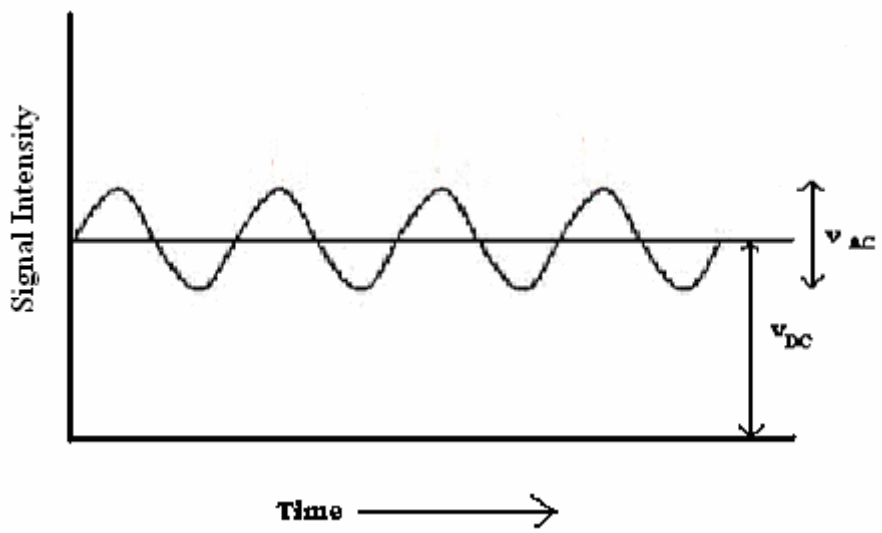

Figure 18 *The output signal.*

The continuous signal coming out of the high-pass filter is phase-locked to the frequency with which the polarisation is modulated by the PEM. The ratio of this rectified signal to the overall absorbance signal gives a value which is directly proportional to the selective absorption and hence the optical activity of the chiral enantiomers under study.

Eventually, we have

$$\frac{V_{AC}}{V_{DC}} = k\,\Delta A \qquad \text{Eq. 24}$$

where V_{AC} & V_{DC} are the 100 kHz and continuous components of V_{out} respectively, and

$$\Delta A = \frac{I^L - I^G}{I^L + I^G} \qquad \text{Eq. 25}$$

where I^L and I^G are the intensities of left and circularly polarised light.

Alignment of the spectrometer

The validity of the VCD measurements strongly depends on a good alignment of the spectrometer.

It is crucial to check whether the ratio of incident LCP:RCP seen by the sample is 50:50. When the degree scale is set at 0, ideally the polarizer will pass radiation whose E vector is in vertical direction, resulting in a 50:50 ratio. However, there is always a residual birefringence in the cell which changes the

ratio. Hence we compensate by turning the polarizer slightly so that the polarizer degree scale is a little shifted from zero. Similarly the position of cell is also rotated with respect to the zero position of the polarizer to minimize the birefringence of the cell.

In order to verify the alignment of the spectrometer we checked first that the IR bands of a non-chiral solvent don't show any dichroism. We then checked the mirror-image relation between the VCD spectra of the two enantiomers of camphor (0.3M in CCl_4) in the same cell as used for our measurements.

All the spectra were measured using solutions of 60 mg of Quinine and Quinidine in 1 ml $CDCl_3$ in an adjustable cell (Harricks) with a path length of 120 μm. The acquisition time was 3h.

The choice of $CDCl_3$ over $CHCl_3$ was mainly to avoid any absorption in the studied region. The solvent $CHCl_3$ absorbs at 1200 cm^{-1} while that of $CDCl_3$ absorbs at 800 cm^{-1}. Since we were mainly interested in the fingerprint region between 900 to 1800 cm^{-1}, $CDCl_3$ was a better choice.

The spectra of Quinine and Quinidine were then corrected for baseline deviation by subtracting the solvent spectra recorded under identical conditions.

Theoretical methods

All the calculations presented in this thesis have been done by K. Le Barbu-Debus. I shall only give a short description of the methods used. A global exploration of the potential energy surface has been done by means of the Macrodmodel program[13] included in the Maestro suite. The 20 most stable isomers have been optimized at the B3lyp/6-31+G(d,p) level of theory with Gaussian 09. Dispersion - corrected density-functional theory (B3lyp-D/6-31+G(d,p) level) 25 has been applied to the most stable isomers to check whether dispersion changes the relative stability of the isomers. As this is not the case, the results presented in what follows are those obtained at the b3lyp/6-31+G(d,p) level of theory. In what follows, the stability of the monomer is given in terms of free energy ΔG at 298.15 K (in kcal/mol) relative to the most stable conformation. Unless specified otherwise, we will limit the discussion to isomers with ΔG smaller than 1.5 kcal/mol. Indeed, those with ΔG above 1.5 kcal/mol have a population smaller than ~5% of the main form.

The vibrational spectrum has been simulated by calculating the harmonic frequencies at the same level of theory and convoluting the scaled frequencies by a Lorentzian line shape of 3 cm^{-1} FWMH. The calculated frequencies have been scaled by 0.96 in the ν(OH) and ν(CH) stretch region and 0.98 in the fingerprint region.

The VCD spectra have been simulated including the solvent ($CHCl_3$) at the same level of theory as the isolated species. The solvation model is the polarizable continuum model (PCM) using the integral equation formalism variant (IEFPCM) provided in the Gaussian 09 package[14].

IX. REFERENCES

[1] V. Lepere, Université Paris XI, Orsay, 22 septembre 2006, "Dynamique de photofragmentation de petits agrégats d'Argon et de molécules biologiques : nouvel outil par piégeage et corrélation vectorielle."

[2] N. Seurre, Université Paris XI, Orsay, 21 septembre 2004, "Etude par spectroscopie de double résonance IR-UV de complexes à liaisons hydrogène formés en jet supersonique : application aux intéractions énantiosélectives."

[3] J. A. Thomas, University of Pittsburgh, 2011, "Structure and dynamics of biomolecules in the gas phase using vibrationally and rotationally resolved electronic spectroscopy."

[4] R. J. Levis, Annual Review of Physical Chemistry **45**, 483 (1994).

[5] R. N. Zare and R. D. Levine, Chemical Physics Letters **136** (6), 593 (1987).

[6] F. Piuzzi, I. Dimicoli, M. Mons, B. Tardivel, and Q. C. Zhao, Chemical Physics Letters **320** (3-4), 282 (2000).

[7] C. Focsa, C. Mihesan, M. Ziskind, B. Chazallon, E. Therssen, P. Desgroux, and J. L. Destombes, Journal of Physics-Condensed Matter **18** (30), S1357 (2006).

[8] C. Riehn, C. Lahmann, B. Wassermann, and B. Brutschy, Chemical Physics Letters **197** (4-5), 443 (1992); R. N. Pribble and T. S. Zwier, Science **265** (5168), 75 (1994); S. Tanabe, T. Ebata, M. Fujii, and N. Mikami, Chemical Physics Letters **215** (4), 347 (1993).

[9] Y. He, W. Bo, R. K. Dukor, and L. A. Nafie, Applied Spectroscopy **65** (7), 699 (2011); J. Sadlej, J. C. Dobrowolski, and J. E. Rode, Chemical Society Reviews **39** (5), 1478 (2010).

[10] http://www.btools.com/vcd_general.htm.

[11] A. F. Drake, Journal of Physics E: Scientific Instruments **19** (3), 170 (1986).

[12] http://www.hindsinstruments.com/applications/polarization/dichroism/vibrational-circular-dichroism/.

[13] MacroModel (Schrödinger, LLC, New York, NY, 2010).

[14] M. J. Frisch, G. W. Trucks, H. B. Schlegel, G. E. Scuseria, M. A. Robb, J. R. Cheeseman, G. Scalmani, V. Barone, B. Mennucci, G. A. Petersson, H. Nakatsuji, M. Caricato, X. J. Li, H. P. Hratchian, A. F. Izmaylov, J. Bloino, G. Zheng, J. L. Sonnenberg, M. Hada, M. Ehara, K. Toyota, R. Fukuda, J. Hasegawa, M. Ishida, T. Nakajima, Y. Honda, O. Kitao, H. Nakai, T. Vreven, J. Montgomery, J. A. , J. E. Peralta, F. Ogliaro, M. Bearpark, J. J. Heyd, E. Brothers, K. N. Kudin, V. N. Staroverov, R. Kobayashi, J. Normand, K. Raghavachari, A. Rendell, J. C. Burant, S. S. Iyengar, J. Tomasi, M. Cossi, N. Rega, J. M. Millam, M. Klene, J. E. Knox, J. B. Cross, V. Bakken, C. Adamo, J. Jaramillo, R. Gomperts, R. E. Stratmann, O. Yazyev, A. J.

Austin, R. Cammi, C. Pomelli, J. W. Ochterski, R. L. Martin, K. Morokuma, V. G. Zakrzewski, G. A. Voth, P. Salvador, J. J. Dannenberg, S. Dapprich, A. D. Daniels, O. Farkas, J. B. Foresman, J. V. Ortiz, J. Cioslowski, and D. J. S. Fox, Gaussian 09, Revision A.02 (Gaussian Inc., Wallingford CT, 2009).

CHAPTER II

Conformational analysis of Quinine and its pseudo-enantiomer Quinidine: A combined jet-cooled spectroscopy and vibrational circular dichroism study

INDEX

List of figures

List of Tables

I. Introduction: Quinine, a Cinchona Alkaloid

Cinchona alkaloids (Figure 1), isolated from the bark of *Cinchona ledgeriana* trees, are mostly known for their medicinal use. They consist of Quinine and Quinidine, on which we shall focus in this work, and also Cinchonine and Cinchonidine, which are derivatives of the former, and are shown in Figure 1.

In early seventeenth century, the French scientists Pierre-Joseph Pelletier and Joseph Bienaimé Caventou discovered the antimalarial property of cinchona bark and isolated its active compound, Quinine. Since then, scientists have put lots of efforts to study in detail the structure of Quinine and its natural stereoisomers, all of which show antimalarial efficiency and are used in the treatment of various forms of cardiac arrhythmias[1]. Doing so, they hoped to synthesize the drug in bulkier amounts in order to cater to its rising demand. Pasteur in 1853, demonstrated that Quinine is laevorotatory and can be converted into the corresponding ketone, called Quinotoxine, by action of dilute acid. This discovery was soon complemented by Strecker by establishing the empirical formula of Quinine as $C_{20}H_{24}N_2O_2$. [2]

These experiments by Pasteur prefigured the use of Cinchona alkaloids as chiral resolving agents, after he started the era of racemate resolutions by the crystallization of diastereomeric salts [3] of tartaric acid. Till today, the unique combination of stereogenic centres in the Cinchona alkaloids are being utilized to obtain pure compounds by chiral separation and in homogeneous and heterogeneous catalysis. Cinchona alkaloids are efficient chiral modifiers used in the heterogeneous enantioselective hydrogenation of ketones[4]. Carbamates derivatives of cinchona alkaloids have been used for the separation of the two enantiomers of aminoacids derivatives[5].

Quinine has a typical alkaloid-like structure (Figure 1) with an N-containing aromatic Quinoline ring and a bicyclic aliphatic tertiary amine called Quinuclidine. These two bulky groups are joined by a chiral linker containing two asymmetric C atoms. In total, Quinine has 5 stereogenic centres (N_1, C_3, C_4, C_8 and C_9). All natural cinchona alkaloids have fixed chirality at N_1(S), C_3(R) and C_4(S) but vary by that of the C_8 and C_9 stereogenic centers located on the linker. The configuration of the chiral linker holds a crucial role in assigning the proper shape to the cavity formed by the two bulky groups.

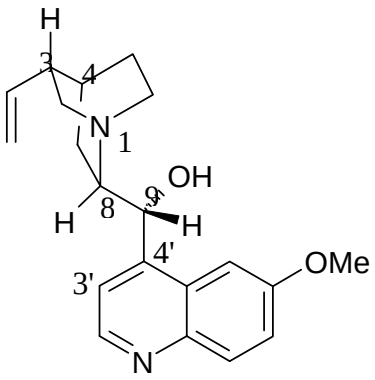

(-)-Quinine (Qn) (1S,3R,4S,8S,9R)

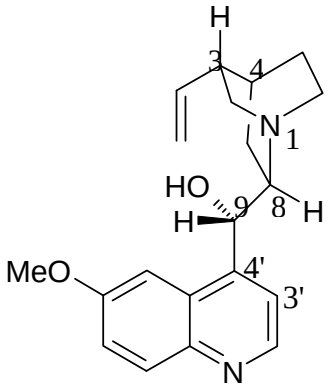

(+)-Quinidine (Qd)(1S,3R,4S,8R,9S)

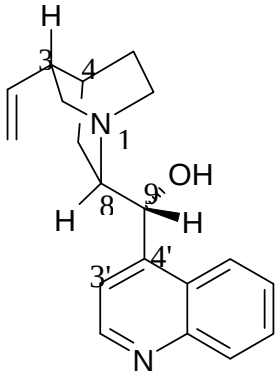

(-)-Cinchonine (Cn) (1S,3R,4S,8S,9R)

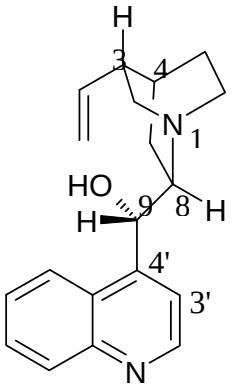

(+)-Cinchonidine (Cd) (1S,3R,4S,8R,9S)

Figure 1: *Structure of Cinchona alkaloids*

Changing the chirality of only the linker C_8 and C_9 atoms gives another cinchona alkaloid called Quinidine, which also exists as a natural substance from the cinchona bark. Strictly speaking, it should be diastereomeric to Quinine as it has two different chiral centres, C_8(R), C_9(S), compared to Quinine, C_8(S), C_9(R).[6,7] However, they behave as true enantiomers for a lot of applications, for example mass spectrometry[8]. But they also show small differences. For example, Quinidine has twice antimalarial efficacy compared to Quinine.[1] Earlier studies suggested that these differences can be explained in terms of distribution ratio (D) between aqueous and lipid phases so that there is a variation in the amount of drug entering the erythrocyte membrane into the parasite's vacuole. Owing to the similarity in their properties, they were renamed as pseudo-enantiomers. Just like Quinine and Quinidine, the other two Cinchona alkaloids Cinchonine and Cinchonidine, which are analogous to Quinine and Quinidine but lack the Methoxy substituent on the aromatic ring, also behave as pseudo-enantiomers.

Besides their medicinal, catalytical, and analytical properties, Quinine finds application in photophysics as a standard for measuring quantum yields. Indeed,

protonated Quinine shows a very high quantum yield (Q_F= 0.546 for λ_{exc}= 310 nm). This high quantum yield is due to the intense emission ($\pi \rightarrow \pi^*$) centered around 340-360 nm originating from the locally excited (LE) state of the Quinoline ring. This transition resembles that of neutral 6-methoxyQuinoline and that of similar methoxy naphthalene derivatives.[9] However, neutral Quinine shows different behaviour and is almost not fluorescent in solution due to the presence of a close-lying $n \rightarrow \pi^*$ transition. In non-polar solvents, only the weak LE transition is observed. As the polarity of the solvent increases, a second red-shifted band appears. This long wavelength emission ($n \rightarrow \pi^*$) corresponds to a fast photoinduced intramolecular charge transfer (ICT) from electron donor N of Quinuclidine to the photoexcited Quinoline ring. It has been studied that higher is the polarity of the solvent, stronger is the quenching of the LE emission leading to lower fluorescence quantum yields. Also, protonation of the Quinuclidine N or H-bond formation with water blocks the charge transfer because the nitrogen lone pair is involved either in a covalent bond or in a hydrogen bond interaction. It therefore restores the LE emission[10,11]. Its very low fluorescence quantum yield explains why there are very few records on the fluorescence of neutral Cinchona alkaloids in organic solvents. In our experiment we try to find out whether neutral Quinine when trapped in gas phase is at all fluorescent. We would also like to know whether such intramolecular charge transfer processes can exist in gas phase.

The group I am working in has recently undertaken a study of cinchona alkaloids in the gas phase. They have focused first on the photophysics of electronically excited protonated cinchona alkaloid dimers, trapped in a quadripolar trap into which they are injected with an electrospray.[6] Ultraviolet irradiation and subsequent mass spectroscopy studies on the fragmentation pattern of the protonated diasteromeric complexes of Cd, Qn and Qd indicated the possibility of formation of a Quinuclidinyl neutral radical fragment in the photoexcited state.[6] The fragment is formed due to a homolytic cleavage around the chiral linker atoms (C_8-C_9 in the α position of the Quinuclidine nitrogen). In our experiment we ablate neutral Quinine and Cinchonidine directly into a supersonic jet and then study the jet cooled electronic spectroscopy initially by two-photon two-colour ionization followed by laser-induced fluorescence. With the help of ionization we want to know whether only the monomer is the most

abundant species in the mass spectra. Further, we want to take a look at the mass of the possible fragments and dimers present in the jet and whether such fragmentation due to α-cleavage of bonds is possible in the radical cation as it is in the protonated species.

Fluorescence excitation and dispersed fluorescence emission studies on jet-cooled naphthalene derivatives β-substituted with an OCH_3 group show the presence of two conformers, which differ in their orientation of the methoxy group with respect to the naphthalene ring.[9] Since Quinine and Quinidine have a similar substitution on the Quinoline ring, it is very interesting to find out whether the same is applicable for Quinine and its pseudoenantiomer Quinidine too. Since all the above studies are done in isolated jet-cooled conditions, it is a great way to discover whether the small differences in pseudo-enantiomers can be evidenced from their vibrational fingerprint. We have had access to several complementary ranges, first the Franck-Condon active frequencies in the range below 2000 cm^{-1} thanks to fluorescence spectroscopy, then to the ν(OH) and ν(CH) stretch mode by means of IR-UV double resonance spectroscopy.

Vibrational circular dichroism is a highly sensitive technique which can detect the minute structural changes in the two pseudoenantiomers, in solution phase. By choosing an aprotic, nonpolar solvent, one can mimic the conditions of isolated gas phase and study in detail the various vibrational transitions of two pseudo-enantiomers in the fingerprint region. This gives us an excellent opportunity to establish whether neutral peudoenantiomers in solution still show difference in their physicochemical activity or in other words, do they behave as true enantiomers.

Hence from the above studies, we can analyze the photophysics of neutral Quinine, isolated in gas phase and compare them to properties in solution. Also, it helps us to understand in detail the reason behind the differences in chemical reactivity of the two pseudoenantiomers.

II. RESULTS OBTAINED FROM CALCULATIONS

II.1. Way of approach

The flexibility of Quinine around the chiral linker gives rise to numerous conformers of Quinine. All the calculations presented here have been done by K. Le Barbu-Debus in our group at the b3lyp/6-31+G(d,p) level of theory. The three most important dihedral angles around which the molecule is very flexible are called τ_1 ($C_{3'}$-$C_{4'}$-C_9-C_8), τ_2 ($C_{4'}$-C_9-C_8-N) and τ_3 (N-C_8-C_9-O).[12-14]

The first two backbone torsion angles define the open and closed nature of conformations. For e.g if the dihedral angle τ_2 is considered, it is mainly responsible for rotating the aliphatic Quinuclidine ring. In order to have minimum steric hindrance, the two tetrahedral C atoms (C_9 and C_8) favour staggered conformations with τ_2 torsion angles of +60° (hindered), -60° (closed) and $\pm$180° (open) as shown in Figure 2. When the Quinuclidine N is located far away from the Quinoline moiety it is termed as open and when its lone pairs are towards the Quinoline ring it is known as closed. The conformer which has both the bulky groups on top of one another is termed as hindered. The different conformations have different affinities towards solvents of different polarity. For e.g, the polar closed conformers are stabilized by polar solvents while non-polar solvents prefer the open conformer.[13 14] Since our molecule of interest is neutral Quinine we want to verify whether the open conformers are abundant in gas phase too.

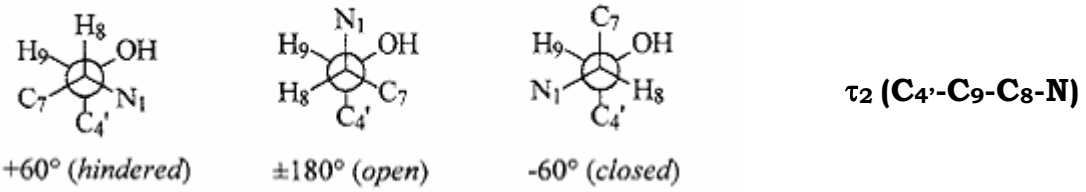

Figure 2: *Newmann Projection of torsion angles τ_2 for Quinidine.*[12]

In this work calculations been done taking into account the dihedral angles τ_1, τ_2 and τ_3 mentioned above. Additionally, the following nomenclature has been considered:

- The *cis* or *trans* position of the Methoxy group with respect to the $C_{4'}$-C_9 bond.
- The hydroxy torsion angle T_3 (C_8-C_9-O-H), which dictates the position of the hydroxy H between the C_8 and $C_{4'}$ atoms. As described by Caner et al[12], the

conformations are described as α, β and γ for values of T_3 +60°,-60° and ± 180° respectively (Figure 3).

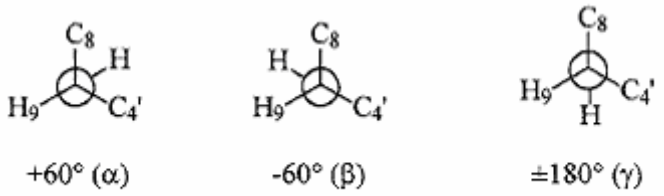

Figure 3: *Newmann projections of torsion angle T_3 of Quinidine*[12]

The utility of adding the above two nomenclatures is to take into account the possibility of intramolecular H bond formation between the Quinuclidine N and the Hydroxy H.

II.2. Quinine

Before introducing the solvent, all the possible stable structures of Quinine with ΔG < 1.5 kcal/mol have been calculated in gas phase at room temperature. The obtained structures are collected in

Quinine in vacuum	**ΔG**	**Population in %**	**τ_1 $C_3C_4C_9C_8$**	**τ_2 $C_4C_9C_8N$**	**τ_3 NC_8C_9O**	**T_3 C_9C_8OH**
cis-γ-open(3)	0.00	72	99	152	-83	174
cis-α-open(3)	1.11	11	104	151	-88	80
cis-γ-closed(1)	1.24	9	-107	58	-178	-180
trans-γ-open(3)	1.28	8	100	154	-82	172
Quinine in $CHCl_3$	**ΔG**	**Population in %**	**τ_1 $C_3C_4C_9C_8$**	**τ_2 $C_4C_9C_8N$**	**τ_3 NC_8C_9O**	**T_3 C_9C_8OH**
cis-γ-open(3)	0.00	92	100	155	-82	170
trans-γ-open(3)	1.46	8	100	158	-78	169
Quinidine in vacuum	**ΔG**	**Population in %**	**τ_1 $C_3C_4C_9C_8$**	**τ_2 $C_4C_9C_8N$**	**τ_3 NC_8C_9O**	**T_3 C_9C_8OH**
cis-γ-open(3)	0.00	78	-99	-153	83	-173
trans-γ-open(3)	1.15	11	-100	-156	81	-171
cis-γ-closed(1)	1.19	11	107	-59	176	178
Quinidine in $CHCl_3$	**ΔG**	**population in %**	**τ_1 $C_3C_4C_9C_8$**	**τ_2 $C_4C_9C_8N$**	**τ_3 NC_8C_9O**	**T_3 C_9C_8OH**
cis-γ-open(3)	0.00	59	-99	-157	79	-170
cis-γ-closed(1)	0.91	13	108	-57	178	-176
cis-α-closed(7)	0.96	12	-17	-58	176	76
cis-γ-closed(2)	1.05	10	-70	-59	-179	180
trans-γ-closed(2)	1.36	6	-69	-56	-177	-178

Table 1. From the calculations it has been observed that the most stable among them is the *cis-γ-open* (3) conformer with a population of 72%. Three more geometries namely *cis-α-open* (3) (11%), *cis*-γ-closed (1) (9%) and *trans-γ-open* (3) (8%) are also found to coexist in the gas phase. The calculated stable structures of Quinine in gas phase are shown below in Figure 4.

The notable features about the most stable conformer are as follows:

- It is to be noted that no OH…N hydrogen bond takes place in these structures as the hydroxyl hydrogen atom is opposite the N atom, with the O and N atoms in an almost *gauche* position, ($N_1C_8C_9O$ dihedral of about -83° or -178°).

- As observed in methoxy naphthalene and its derivatives[9,15], here too, the most stable conformation pertains to the *cis* position of the OMe substituent of the Quinoline ring.

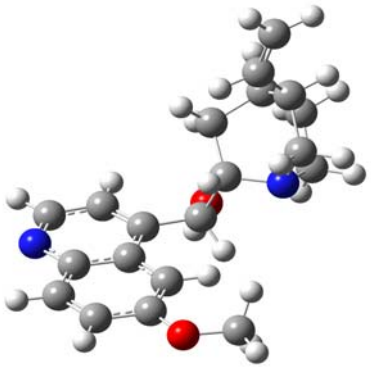

***cis*-γ-open(3)-most stable**

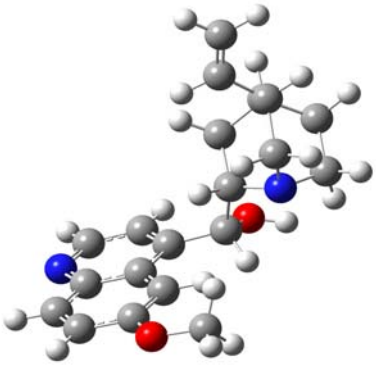

***cis*-α-open(3)**

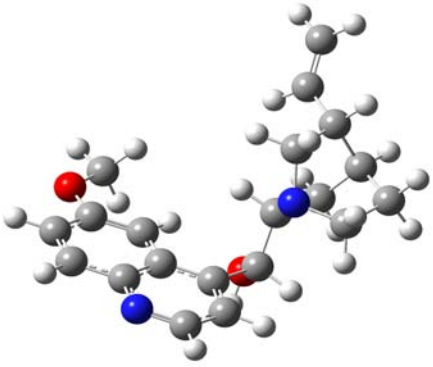

***cis*-γ-closed(1)**

Figure 4: *Calculated stable structures of Quinine in gas phase: cis-γ-open(3) (ΔG=0), cis-α-open(3) (ΔG=1.11 kcal/mol), cis-γ-closed(1) (ΔG=1.24 kcal/mol).*

On introduction of the solvent, only two predominant conformers are found, out of which the *cis-γ-open* (3) is still the most stable one with a higher population of 92% compared to the gas phase. The other conformer present has the *trans-γ-open* (3) geometry and a population of 8%. It is interesting to note that none of them are of closed geometry and that the possibility of intra molecular hydrogen bond remains very weak even in solution phase.

The two most stable structures of Quinine in solution are shown below.

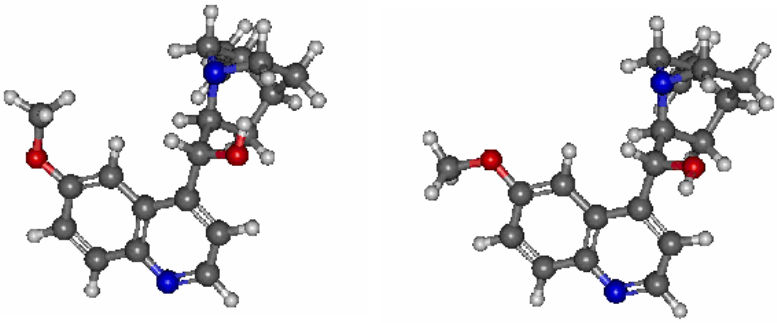

Figure 5: *The most stable geometries of Quinine in $CHCl_3$, cis-γ-open (3) (ΔG=0) left) and trans-γ-open (3) (ΔG=1.46 kcal/mol right).*

II.3. Quinidine

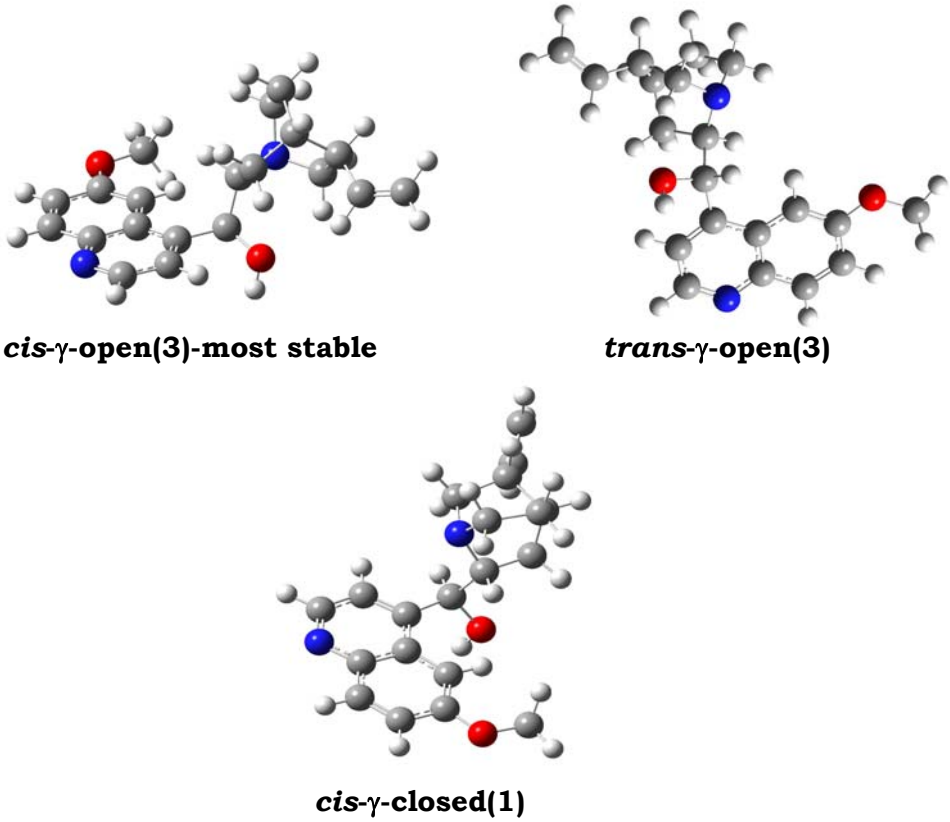

Figure 6: *The most stable calculated structures of Quinidine in gas phase: cis-γ-open(3) (ΔG=0), trans-γ-open(3) (ΔG=1.15 kcal/mol) and cis-γ-closed(1) (ΔG=1.19 kcal/mol).*

At the outset, the configuration of the chiral C_8 and C_9 carbon atoms are exactly the opposite of Quinine. This change in configuration leads to opposite values of the dihedral angles τ_1, τ_2, τ_3 too. However, it is to be noted that even

with the opposite values, the corresponding open and closed conformations are same for both the molecules.

Gas phase calculations yield the *cis-γ-open (3)* as the most stable structure with an *open* geometry. It is clearly the most abundant conformer with a Boltzmann population of 78%. It is followed by a second conformer (*trans-γ-open(3)*) with the methoxy substituent of the Quinoline ring in *trans* configuration, calculated at 1.15 kcal/mol higher in energy and contributing to the population by 11%. An almost isoenergetic structure (*cis-γ-closed(1)*) is found, with the methoxy in *cis* position; it corresponds to a *closed* geometry with the N atom of Quinuclidine ring standing above the Quinoline ring. In contrast to Quinine, a closed geometry is found among the most stable ones. The three-most stable structures of Quinidine in gas phase are shown in Figure 6.

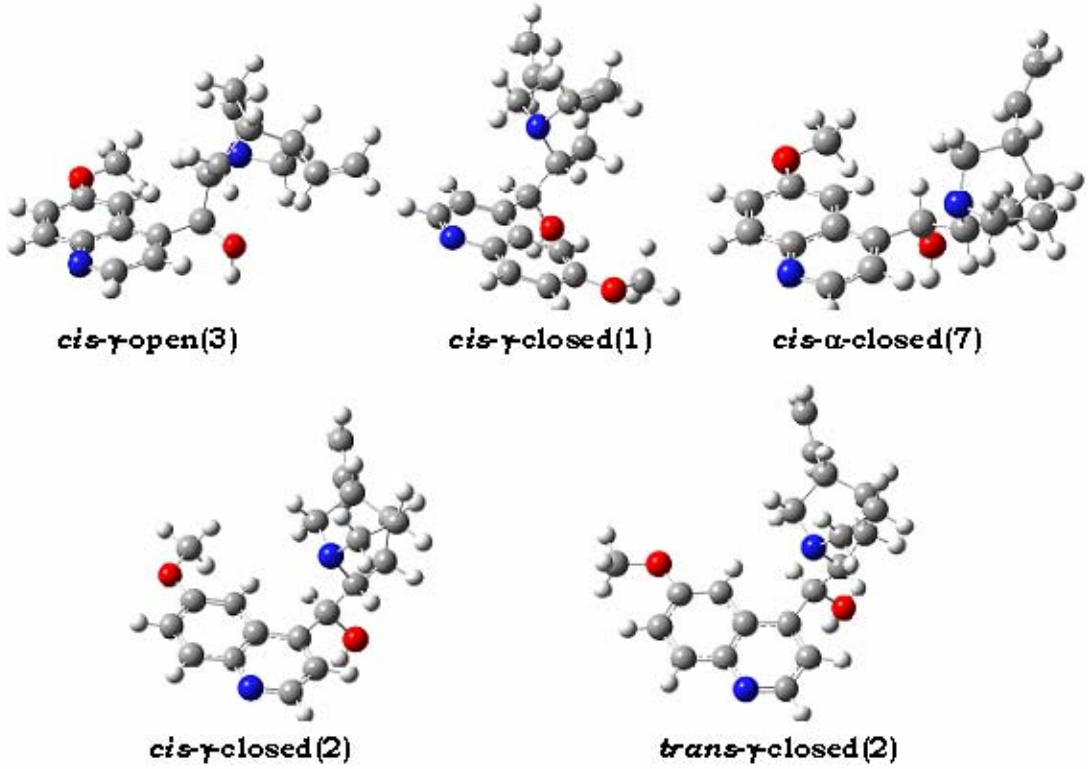

Figure 7: *Calculated stable structures of Quinidine in $CHCl_3$: cis-γ-open(3)(ΔG=0), cis-γ-closed(1)(ΔG=0.91kcal/mol), cis-α-closed(7)(ΔG=0.96 kcal/mol),cis-γ-closed(2)(ΔG=1.05kcal/mol)and trans-γ-closed(2)(ΔG=1.36 kcal/mol).*

After including the solvent, the *cis-γ-open(3)* remains as the most stable conformer. However, unlike Quinine, the percentage of abundance decreases from 78% to 59% in solution. Hence there is a coexistence of four other conformers in

solution. Out of which, *cis-γ-closed(1), cis-α-closed(7), cis-γ-closed(2)* are found with population nearly 10% and *trans-γ-closed(2)* exists as 6%.

The five most stable structures of Quinidine in solution are given in Figure 7.

Quinine in vacuum	**ΔG**	**Population in %**	**τ_1 C_3,C_4,C_9C_8**	**τ_2 C_4,C_9C_8N**	**τ_3 NC_8C_9O**	**T_3 C_9C_8OH**
cis-γ-open(3)	0.00	72	99	152	-83	174
cis-α-open(3)	1.11	11	104	151	-88	80
cis-γ-closed(1)	1.24	9	-107	58	-178	-180
trans-γ-open(3)	1.28	8	100	154	-82	172
Quinine in $CHCl_3$	**ΔG**	**Population in %**	**τ_1 C_3,C_4,C_9C_8**	**τ_2 C_4,C_9C_8N**	**τ_3 NC_8C_9O**	**T_3 C_9C_8OH**
cis-γ-open(3)	0.00	92	100	155	-82	170
trans-γ-open(3)	1.46	8	100	158	-78	169
Quinidine in vacuum	**ΔG**	**Population in %**	**τ_1 C_3,C_4,C_9C_8**	**τ_2 C_4,C_9C_8N**	**τ_3 NC_8C_9O**	**T_3 C_9C_8OH**
cis-γ-open(3)	0.00	78	-99	-153	83	-173
trans-γ-open(3)	1.15	11	-100	-156	81	-171
cis-γ-closed(1)	1.19	11	107	-59	176	178
Quinidine in $CHCl_3$	**ΔG**	**population in %**	**τ_1 C_3,C_4,C_9C_8**	**τ_2 C_4,C_9C_8N**	**τ_3 NC_8C_9O**	**T_3 C_9C_8OH**
cis-γ-open(3)	0.00	59	-99	-157	79	-170
cis-γ-closed(1)	0.91	13	108	-57	178	-176
cis-α-closed(7)	0.96	12	-17	-58	176	76
cis-γ-closed(2)	1.05	10	-70	-59	-179	180
trans-γ-closed(2)	1.36	6	-69	-56	-177	-178

Table 1: *List of the Boltzmann populations, Gibbs free energies and dihedral angles of the different conformers of Quinine and Quinidine present at room temperature.*

Thus Quinine and Quinidine behave a little differently when they are introduced in solution. While the number of conformers increases for Quinidine, in case of Quinine it's just the opposite. Also, what is interesting the predominance of open conformers of Quinine in solution compared to the closed

ones for Quinidine. The Boltzmann populations and Gibbs free energies of the most stable structures of Quinine and Quinidine have been listed in

Quinine in vacuum	**ΔG**	**Population in %**	**τ_1 C_3,C_4,C_9C_8**	**τ_2 C_4,C_9C_8N**	**τ_3 NC_8C_9O**	**T_3 C_9C_8OH**
cis-γ-open(3)	0.00	72	99	152	-83	174
cis-α-open(3)	1.11	11	104	151	-88	80
cis-γ-closed(1)	1.24	9	-107	58	-178	-180
trans-γ-open(3)	1.28	8	100	154	-82	172
Quinine in $CHCl_3$	**ΔG**	**Population in %**	**τ_1 C_3,C_4,C_9C_8**	**τ_2 C_4,C_9C_8N**	**τ_3 NC_8C_9O**	**T_3 C_9C_8OH**
cis-γ-open(3)	0.00	92	100	155	-82	170
trans-γ-open(3)	1.46	8	100	158	-78	169
Quinidine in vacuum	**ΔG**	**Population in %**	**τ_1 C_3,C_4,C_9C_8**	**τ_2 C_4,C_9C_8N**	**τ_3 NC_8C_9O**	**T_3 C_9C_8OH**
cis-γ-open(3)	0.00	78	-99	-153	83	-173
trans-γ-open(3)	1.15	11	-100	-156	81	-171
cis-γ-closed(1)	1.19	11	107	-59	176	178
Quinidine in $CHCl_3$	**ΔG**	**population in %**	**τ_1 C_3,C_4,C_9C_8**	**τ_2 C_4,C_9C_8N**	**τ_3 NC_8C_9O**	**T_3 C_9C_8OH**
cis-γ-open(3)	0.00	59	-99	-157	79	-170
cis-γ-closed(1)	0.91	13	108	-57	178	-176
cis-α-closed(7)	0.96	12	-17	-58	176	76
cis-γ-closed(2)	1.05	10	-70	-59	-179	180
trans-γ-closed(2)	1.36	6	-69	-56	-177	-178

Table 1.

III. GAS-PHASE SPECTROSCPOPY: EXPERIMENTAL RESULTS

III.1. Electronic And Vibrational Spectroscopy On Test Molecule Naproxen

Before starting with Quinine, a structurally similar molecule called Naproxen was used to characterize the ablation source. The structure of (S)-Naproxen is shown below.

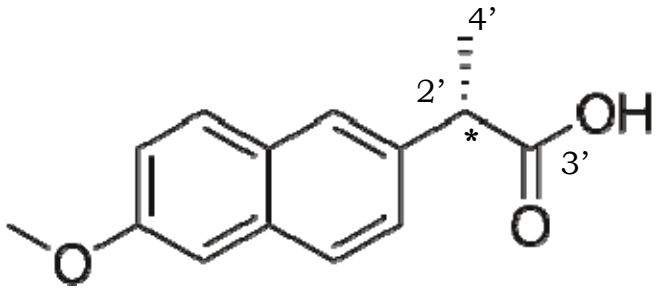

Figure 8: *Structure of naproxen showing the chiral centre.*

The reasons behind the choice of Naproxen are as follows:

- The electronic band origin is around the same wavelength region as that of methoxy-substituted naphthalene derivatives.[9]
- Naproxen exists as two conformers and their energy difference has been calculated precisely.
- The excited state life time of Naproxen is reasonably high, which makes it easy to study with 2-colour-2-photon spectroscopy. It has been measured to 22 ± 1 and 24 ± 1 ns, respectively, for the two conformers.[16]

  From the plot it is observed that the four prominent bands (0-0, 38, 47 and -101 cm $^{-1}$) are still visible when the delay between excitation and ionisation lasers increases.
- Naproxen has high laser ablation efficiency. It has been verified with the help of a heated source and a laser ablation source that, under jet-cooled conditions, both the sources can be utilized for approximately the same duration. Specifically in case of the latter, even with low power of ablation, an intense and cold signal is obtained.
- Naproxen shows an intense IR-UV depletion, and hence can be used to align the two lasers even at low laser powers (both IR and UV).

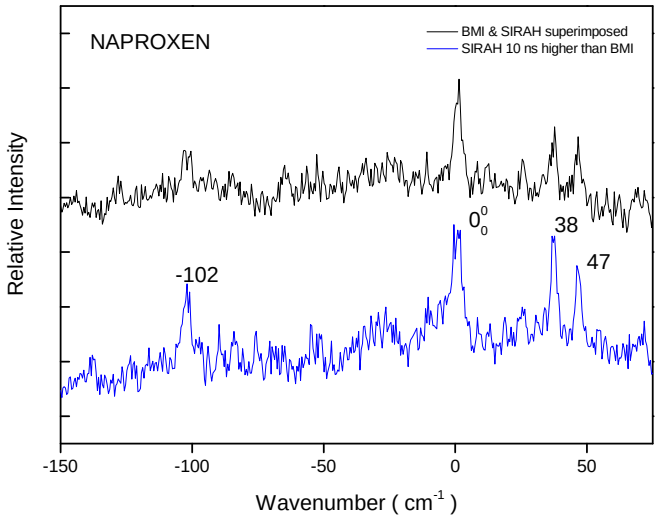

Figure 9: *Comparative study of REMPI excitation spectrum of Naproxen with change in delay between excitation and ionisation lasers. The zero of the x axis is the origin transition of the main conformer of naproxen.*

The IR-UV double resonance experiments in the laser-induced fluorescence set-up were tested initially with naproxen in a heated source and then followed by an ablation source. The plots below shows the intense dip obtained in both cases. The spectra show similar width and depletion efficiency whether the heated source or the ablation is used, which shows that the jet of Naproxen is cold.

The spectra presented below (Figure 10) have been obtained with different IR power. The IR power can be adjusted by decreasing the intensity of the OPA's pump by rotating a polariser located on the pump beam. The farther is the polariser from the optimal position of 40°, the smaller is the intensity.

It is to be noted that even at lower laser power, the half width maximum is 10 cm^{-1} and that the depletion is more than 70%, thereby indicating that the absorption is intense enough to be in the limit of saturation.

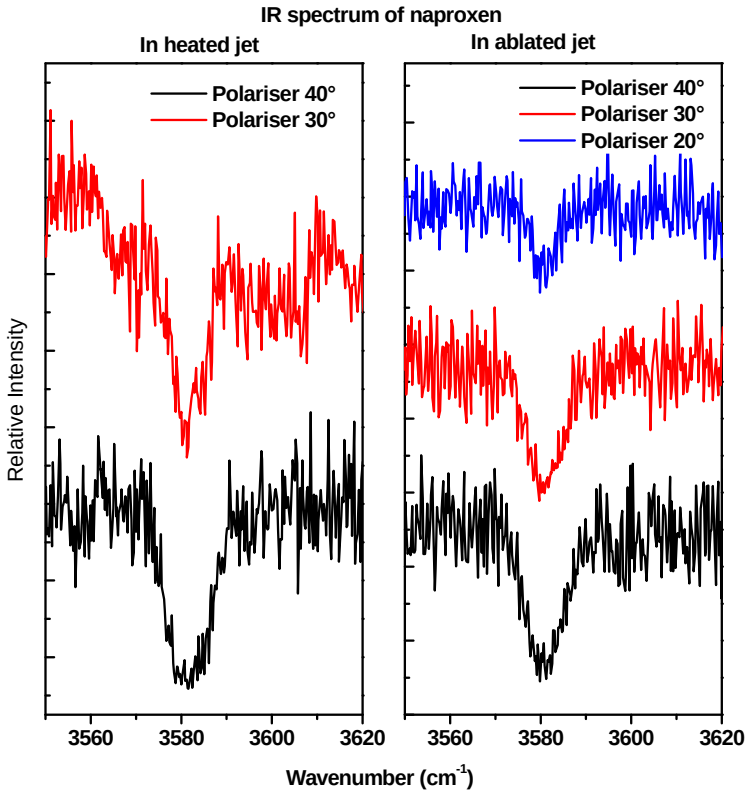

Figure 10: *IR-UV depletion of naproxen using a heated source and an ablation source*

III.2. Temperature Of Ablation Source

It is important to have an idea of the temperature of the ablation source because the population of conformers is dependent on it. At higher temperature, there is a growing tendency for hot molecules to be present. This absorption from the hot bands appears as a background in the absorption spectrum. This background might be due to the following reasons:

- Cluster formation especially when Ar is the carrier gas.
- Hot bands due to excitation from higher vibrational level of the electronic ground state to the vibrational levels of the excited electronic state.

With the following plot for naproxen as a reference, the Boltzmann calculations were done taking the intensities of its two conformers denoted as I_R and I_B. Naproxen has already been studied with a *heated* source [16] and the temperature used for the experiment was fixed at about the melting point of the molecule (around 150^{0}C). From the ratio of intensities of the two conformers in

the calculated plot and the temperature as mentioned above, the energy difference between the two conformers has been calculated in the following way:

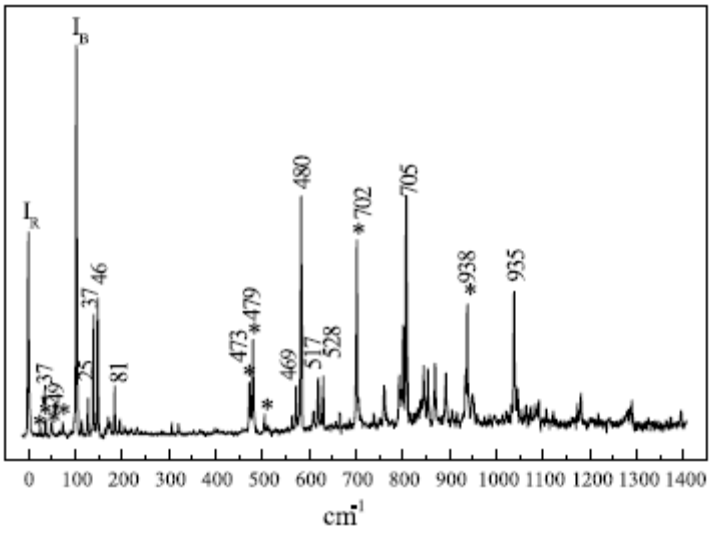

Figure 11: *Fluorescence excitation spectrum of bare S-Naproxen.*[16]

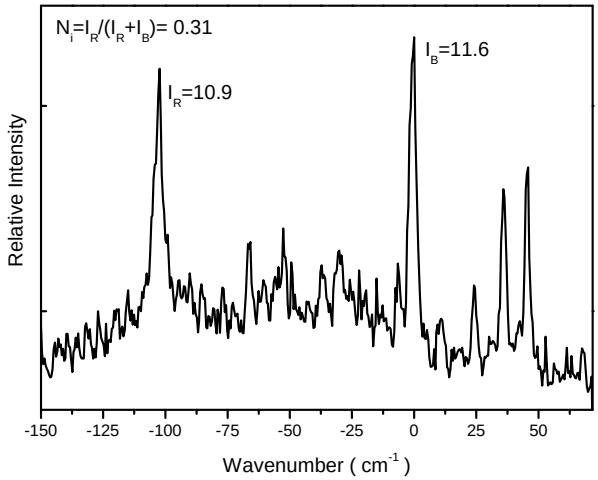

Figure 12: *Fluorescence excitation spectrum of naproxen using an ablation source.*

Using the Boltzmann distribution relation:

$$N_i = \frac{\exp^{-E_i/kT}}{Z} \qquad \textbf{Eq. 1}$$

where the proportion of the two calculated conformers N_i= 0.31, T = 150°C and k = 1.986 * 10^{-3} kcal K^{-1} mol^{-1}.

Using the above values E = 0.64 kcal mol^{-1}, which is lower than the calculated value of 1.24 kcal/mol [16]

With this difference in energy and the intensity ratio from the experimental plot (Figure 12), the temperature of the *ablation* source has been calculated as follows.

N_i = 0.7 (from Figure 12)

E= 0.64 kcal mol^{-1}, T= 833 K which is approximately 560°C.

Although the calculations are approximate, the difference in values clearly gives an indication that an ablation source is hotter than the heated source. This value is only indicative; the ablation conditions vary with the systems studied. Moreover, it is likely that the jet is in non-equilibrium conditions and that the temperature is difficult to define.

III.3. Time Of Flight Mass Spectroscopy Of Quinine And Related Molecules

As neutral Quinine does not fluoresce in solution, a hypothesis can be drawn that it would not fluoresce in gas phase either. Hence REMPI experiments for recording the S_0-S_1 spectrum of Quinine have been performed. To achieve that, initially a mass spectrum of Quinine has been recorded, with Naproxen as an internal standard. As mentioned in the experimental part, two colour-two photon ionisation is necessary as the $S_1 \rightarrow D_0$ energy is larger than the $S_0 \rightarrow S_1$ energy.

The challenging part of the REMPI experiment is therefore to reduce the 1-colour effect due to the ionisation laser. The following Figure 13 shows the time of flight mass spectrum done on a pellet containing a mixture of Quinine and naproxen using either ionisation laser only (266 nm radiation), or excitation laser only (325 nm radiation), or both. From the Figure 13 it is observed that the peaks obtained are intense only when the two lasers are superimposed. Also, the 1-colour effect due to the ionisation laser is higher than that of the excitation laser because two photons of the former are enough to ionise the system unlike the two photons of the latter. The 2-colour effect is dependent not only on the delay between the two lasers but also on the power of the laser. This is why the focalisation conditions of the ionisation laser have been carefully defined by avoiding focalisation on the jet position and by simply building an afocal system

of magnification 0.25 by means of two lenses of focal length 1000 mm and 250 mm. This allows minimising the 1-colour effect.

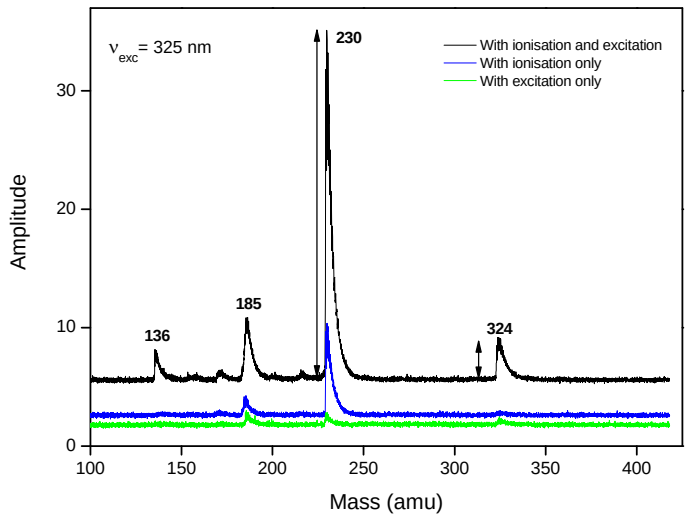

Figure 13: *The time of flight mass spectrum of Quinine and Naproxen. The black curve indicates the superimposition of both the excitation and ionisation lasers. The blue and green curves indicate the presence of the ionisation and excitation laser respectively.*

The time of flight mass spectrum given in Figure 13 above shows four prominent peaks. Among them, the two peaks at 230 and 324 amu have been assigned to the monomer of Naproxen and Quinine respectively. As shown in the spectrum above, the monomer of Naproxen is approximately 10 times more intense than that of Quinine thereby indicating that Quinine is more difficult to ablate than Naproxen.

The mass 185 amu corresponds to the loss of neutral COOH (45 amu) in Naproxen, with the charge being localised in the aromatic ring. The mass 136 amu corresponds to the loss of a Quinuclidine cation in Quinine. In this case, the charge is no longer on the aromatic ring which is ejected as a neutral fragment.

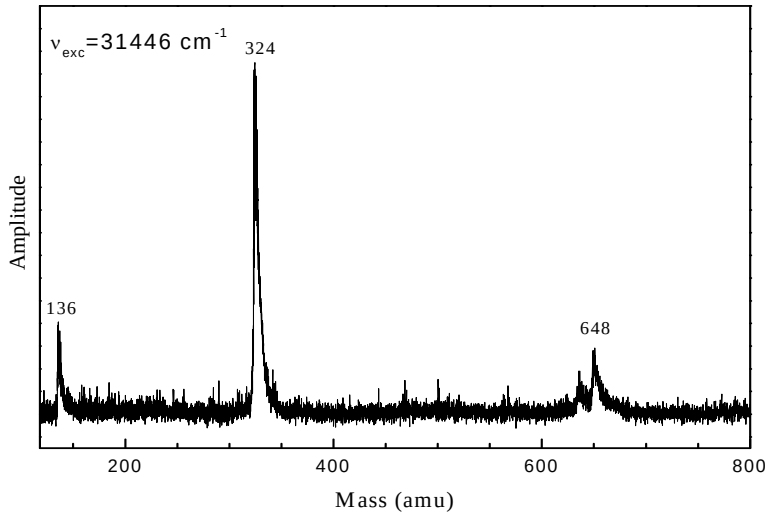

Figure 14: *The time of flight spectrum of Quinine (excitation laser at 318 nm laser at 266 nm).*

(a) Supersonic jet : Naproxen

$$\left(\underset{230}{C_{14}H_{14}O_3}\right) \xrightarrow{UV} \left(\underset{230}{C_{14}H_{14}O_3}\right)^{+} \longrightarrow \left(\underset{186}{C_{14}H_{13}O_3 - COOH}\right)^{+} + \underset{44}{COOH}^{\bullet}$$

(b) Ion trap: Protonated Quinine dimer:

$$\left(\underset{649}{C_{20}H_{24}N_2O_2}\right)_2 H^+ \xrightarrow{UV} \left(\underset{324}{C_{20}H_{24}N_2O_2}\right) + \left(\underset{325}{C_{20}H_{24}N_2O_2}\right)H^+$$

$$OR \quad \left(\underset{513}{(C_{20}H_{24}N_2O_2)_2 - C_9H_{15}N}\right)^{\bullet} H^+ + \underset{136}{(C_9H_{15}N)^{\bullet}}$$

(c) Supersonic jet: Quinine

$$\underset{324}{C_{20}H_{24}N_2O_2} \xrightarrow{UV} \left(\underset{324}{C_{20}H_{24}N_2O_2}\right)^{+\bullet} \longrightarrow \left(\underset{136}{C_9H_{14}N}\right)^{+\bullet} + \left(\underset{188}{(C_{20}H_{24}N_2O_2) - C_9H_{14}N}\right)^{\bullet}$$

Figure 15: *(a) depicts the resulting ions and neutral radical formed by REMPI in a supersonic jet seeded with naproxen.*

(b) shows the resulting ions observed after UVPD MS^2 on $(Qn)_2H^+$ complex in an ion trap.[6]

(c) shows the resulting neutral fragment, dimer and monomer after REMPI on a supersonic jet seeded with Quinine.

Figure 14 shows the time of flight spectrum of Quinine when excited by two UV lasers at 318 and 266 nm. Here along with the monomer (324 amu) and the photofragment (136 amu) a dimer of Quinine has been observed too at 648 amu.

The presence of the dimer is an indication of a cold jet. The photofragment at 136 amu is particularly interesting as it is a reminiscent of earlier studies done on protonated Quinine[6], despite being different in terms of charge state. Here, the cation radical fragment is formed due to a homolytic cleavage of the C_8-C_9 bond α to the Quinuclidine nitrogen in Quinine. This shows that the charge initially located on the Naphthalene ring after photoexcitation has migrated to the tertiary amine of the Quinuclidine. This is not surprising as the ionisation potential (IP) of Quinuclidine (IP = 7.5 eV) is lower than that of a Naphthalene ring (IP = 8.14 eV). While in the UV photodissociation experiments of protonated dimers, the Quinuclidine fragment at 136 amu is a neutral radical, here the 136 amu fragment is a radical cation. In the flowchart shown in Figure 15 we depict the results obtained by the two experiments.

III.4. Resonance Enhanced Multiphoton Ionisation On Laser Ablated Quinine And Quinidine

The S_0-S_1 spectrum of Quinine has been recorded and compared to that of (S)-Naproxen (Figure 16).

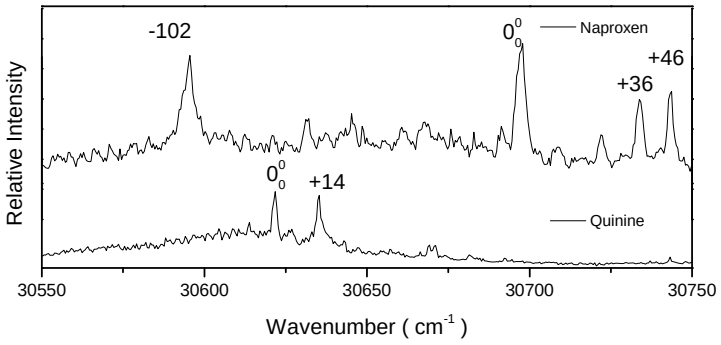

Figure 16: *REMPI spectrum of Quinine and Naproxen near the band origin of each molecule.*

The difference in the intensities of absorption of ablated Quinine and Naproxen in a REMPI experiment shows that the latter undergoes better ablation than the former. From the plot it is observed that the S_0-S_1 wavelength of Naproxen and Quinine differ by 75 cm^{-1} only, which is one of the main reasons behind the choice of the test molecule.

The following plot (Figure 17) depicts the mass-selected REMPI spectrum of Quinine in presence of Ar (black) and Ne (blue) as carrier gases. In each case, an intense absorption is observed at 30621 cm^{-1} which has been assigned to the band origin ($S_1 \leftarrow S_0$). In presence of Ar, several intense vibronic bands are observed at 14, 47, 121, 147 cm^{-1} to the blue; other bands are seen at 197, 178 cm^{-1} to the red. However, in presence of Ne, there occurs a substantial decrease in intensity of the bands to the red of the band origin along with that of the background. It is interesting to note that the band at +14 cm^{-1} continues to dominate as it is almost equally intense to the band origin irrespective of the carrier gas introduced. Hence the Figure 17 illustrates as an alternative way to decrease the background, simply by changing the inert gas Ar with Ne.

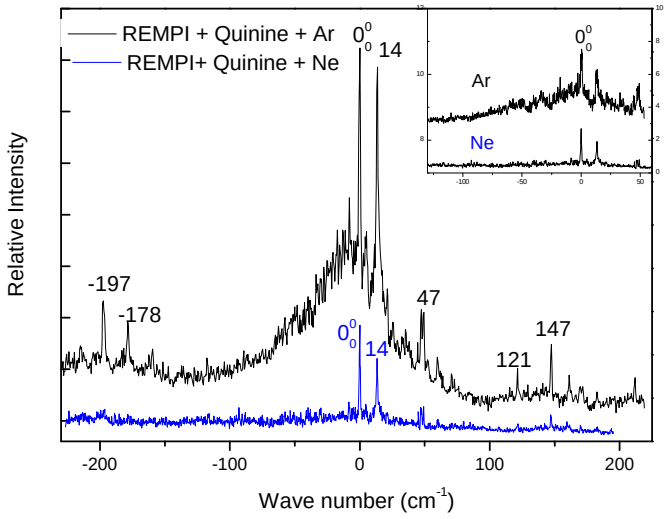

Figure 17: *REMPI Spectrum of Quinine in presence of Ne and Ar as carrier gas. The inset plot shows the difference in background within +/- 100 cm^{-1} of the band origin.*

A comparison of the total REMPI spectrum of Quinine and Quinidine in the range 30630 to 31630 cm^{-1} is shown in Figure 18.

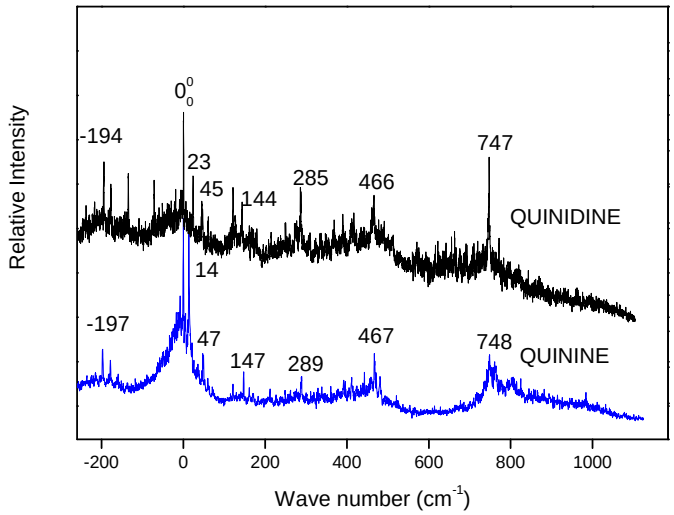

Figure 18: *A comparison between the REMPI spectrum of Quinine and Quinidine.*

Along with the bands observed in the earlier spectrum, two intense vibronic bands are observed at energies higher than 200 cm^{-1}. Among these two, the band at 467 cm^{-1} represents the $8b_{1g}$ vibronic mode of Naphthalene characteristic of the L_b $\pi\pi^*$ transition of Naphthalene derivatives. This band gains in intensity by a Herzberg-Teller coupling with the S_2 state (L_a transition) in Naphthalene. This particular mode is usually active in the excitation spectrum of Naphthalene derivatives even when substitution makes the transition Franck-Condon allowed.[9,16-18]. The other band at 747 cm^{-1} has been assigned to the $8a_{1g}$ mode of Naphthalene. A detailed study of the difference in absorption between Quinine and Quinidine particularly in the low frequency region will be discussed in the laser-induced fluorescence section.

III.5. Life-Time Measurement

The lifetime of Quinine was recorded by temporally displacing the excitation laser 10 ns before the optimum delay position (the delay at which the ionisation and the excitation lasers superimpose) and recording the intensity of absorption at a particular UV excitation wavelength (for *e.g* the S_0-S_1 excitation at 30621 cm^{-1}) as shown in Figure 19.

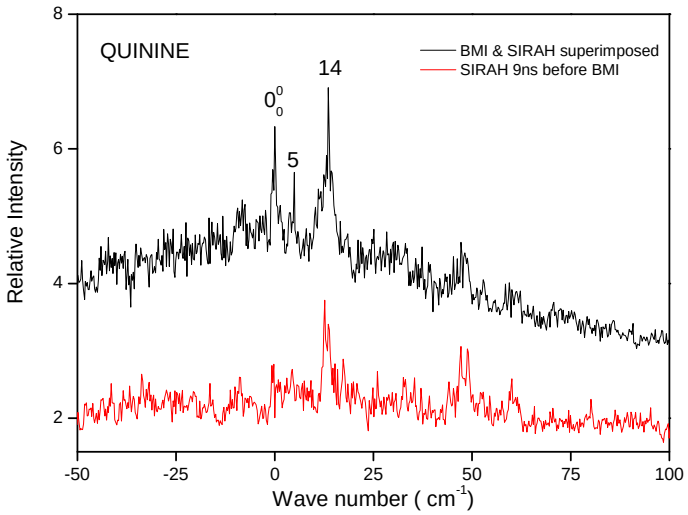

Figure 19: *Comparison between the excitation spectrum of Quinine with change in delay between and excitation in REMPI. The zero of the X axis is the S_0 → S_1 transition of Quinine.*

Hence, judging from the figures 9 and 19 an idea can be obtained about the longer lifetime of naproxen compared to Quinine. The curve obtained shows that Quinine absorbs the ionisation laser within 10 ns after being excited by the excitation laser. Since the pulse of the lasers used is 10ns, it can be safely said that the lifetime of Quinine lies within a pulse of a laser.

IV.Laser Induced Fluorescence On Quinine And Quinidine

IV.1. Laser Induced Fluorescence Excitation

The plot shown in Figure 20 is a comparison between laser-induced fluorescence and REMPI spectrum of Quinine in presence of Ne gas. As is evident from the spectrum, with laser induced fluorescence one can achieve a signal to noise ratio which cannot be attained in the REMPI spectrum, even with Ne as a carrier gas. The signal to noise ratio of the spectra recorded in fluorescence is at least 3 times more intense than REMPI with the FWHM of the 0-0 band being 1 cm^{-1} and 1.4 cm^{-1} for FLUO and REMPI respectively. This might be due to the fact that excitation of hot species to higher energy states can be detected in the form of ions but no longer as photons as these excited states in most cases are non-fluorescent.

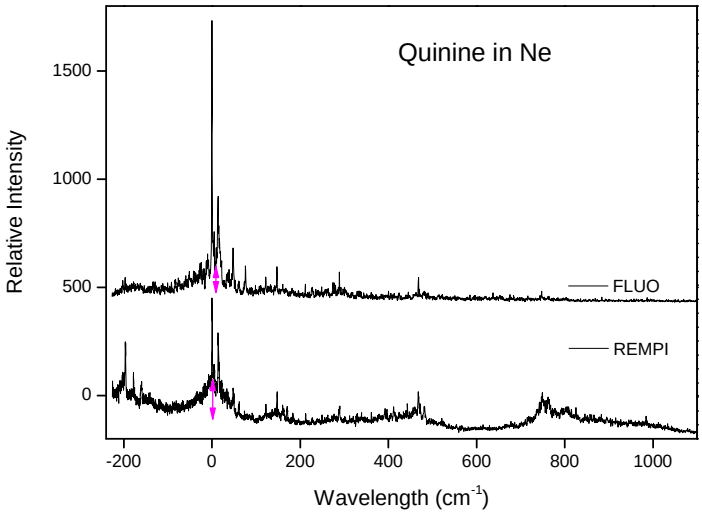

Figure 20: *Comparison between the REMPI and LIF spectra of Quinine in presence of carrier gas Ne. The zero of the scale has been taken as the 0-0 transition of both the pseudo-enantiomers. The magenta arrow shows the background due to hot species absorbing in the same range.*

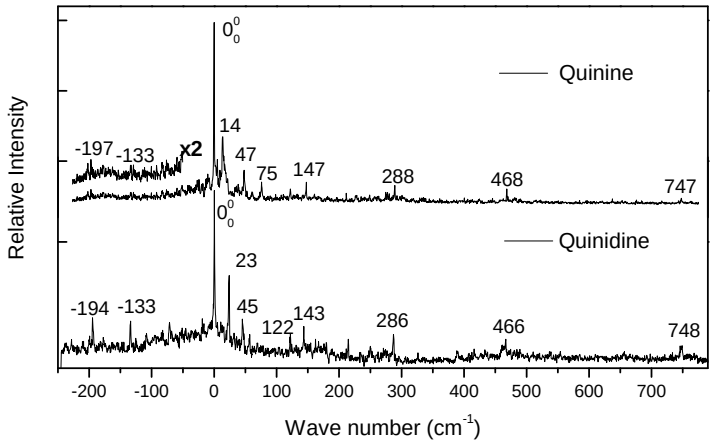

Figure 21: *Laser induced fluorescence excitation spectrum of a) Quinine and b) Quinidine under jet cooled conditions and in presence of inert gas Ne. The zero of the scale is set at the transition origin located at 30621 cm^{-1} for Quinine and 30641 cm^{-1} for Quinidine, respectively.*

The Figure 21 is the LIF spectra of Quinine and Quinidine together. Both the plots closely resemble the REMPI spectrum shown in Figure 16.

The main features observed in the above spectrum are as follows:

- We can divide the fluorescence excitation spectra of β-substituted Naphthalene in two distinct regions, the low-frequency modes region (30300-30500 cm^{-1}) where the modes located on the substituents are expected to appear, and the high frequency part (> 30500cm^{-1}) where we will observe the modes corresponding to the deformation of the aromatic ring. There is no sign of L_a absorption at higher energy (> 32000 cm^{-1}) in contrast to the rich vibronic spectrum observed in Naphthalene derivatives. There exists only a single region of absorption and unlike other structurally similar molecules there is no evidence of L_a transition (Figure 22).[19 20]
- Just like other β-substituted Naphthalene derivatives the origin transition is the most intense band in the entire excitation spectrum, because the observed transition is the Franck-Condon allowed L_b ππ* transition. This is in contrast to the fluorescence excitation spectrum of Naphthalene, which shows no 0-0 transition but is built on the Herzberg-Teller allowed $8b_{1g}$ transition acting as a false origin for the L_b transition.

In Naphthalene, an accidental cancellation of the transition moment occurs which cancels out the oscillator strength to the lowest excited state S_1 of Naphthalene inspite of being symmetry allowed.

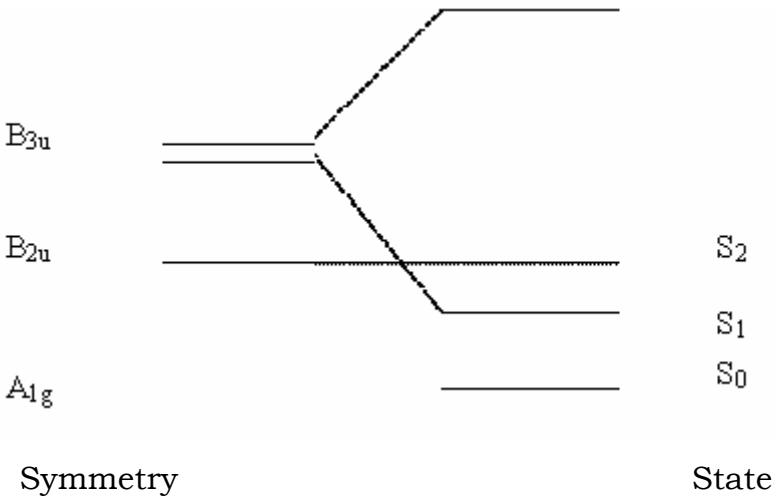

Figure 22: *Symmetry and states of Quinine.*

Thus the electronic $S_1 \leftarrow S_0$ spectrum of Naphthalene has a weak origin transition and intense Herzberg-Teller induced bands. However, when substitution of an H atom of the Naphthalene subunit is done, the symmetry is reduced. Hence the $S_1 \leftarrow S_0$ transition moments are no longer directed parallel to either the long (a-axis) or the short (b-axis), but a mixture of both. The fluorescence excitation spectra of jet-cooled Naphthalene,

1-Methylnaphthalene, 2-Methylnaphthalene, Naproxen and Quinine have been shown together in Figure 23 to depict the enhancement of origin with loss in symmetry of the chromophore.

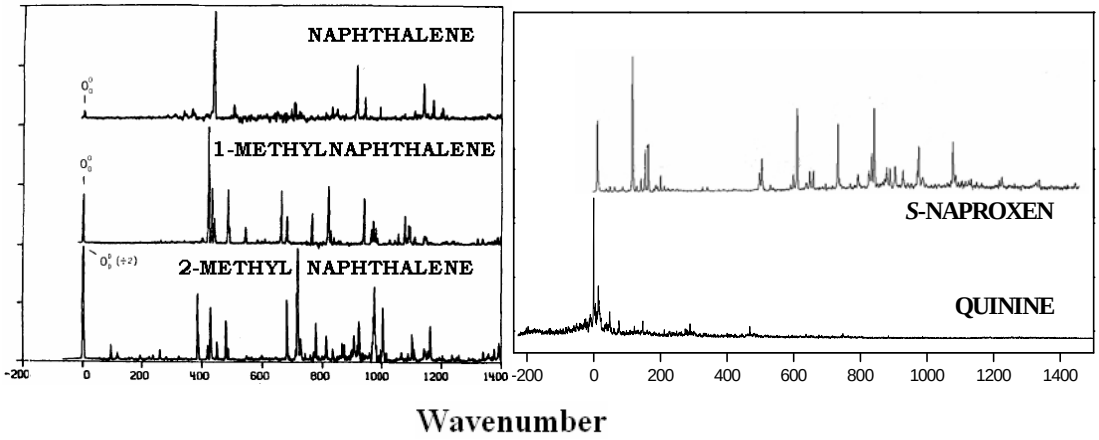

Figure 23: *Comparison of the intensities of the origin transitions for Naphthalene,1-Methylnaphthalene,2-Methylnaphthalene[21], S-Naproxen[16] and Quinine.*

The 0-0 transition of Quinidine is shifted 20 cm^{-1} to the blue compared to Quinine and bears strong resemblance to the latter. Especially, the frequencies located on the Quinoline frame appear at very similar values. The main difference between the vibronic bands of both the pseudoenantiomers appears in the low frequency region. In order to check whether this difference comes from a hot jet or the inherent properties of the molecule it is important to focus on the low frequency region of the two pseudoenantiomers.

The low-frequency region of the spectrum given in Figure 24 (a) shows a marked difference in the position of bands for the two molecules. The similarity between the two plots is that the bands in each case do not really follow a vibrational progression. This is due to a band very close to the band origin (14 cm^{-1} for Quinine and 23 cm^{-1} for Quinidine) which varies in intensity with the cooling conditions of the jet. This band is more intense than all the other bands in the spectrum except the band origin for both the molecules. Hence it is interesting to find out whether the source of this band is due to a hot jet. Systematic studies have been done by changing the delay between the ablation laser and the excitation laser.

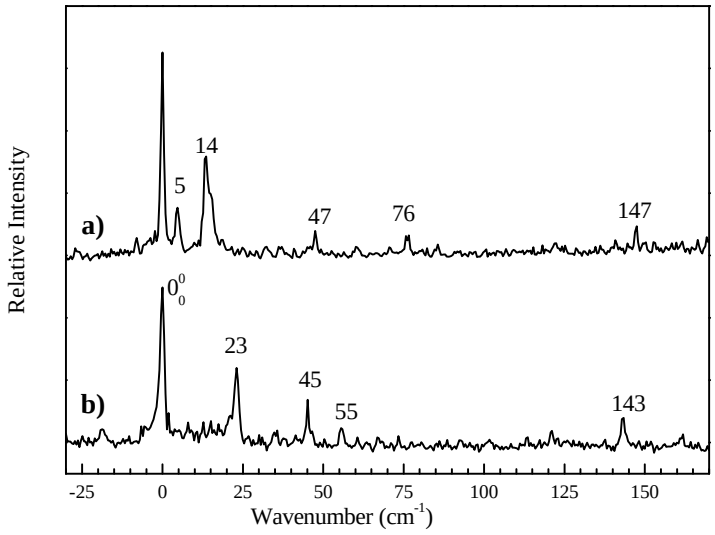

Figure 24: *Comparative study of the LIF ($S_0 \rightarrow S_1$) spectrum of a) Quinine and b) Quinidine showing the first 200 cm^{-1} towards blue. The 0-0 transition for each has been taken as the zero of the scale.*

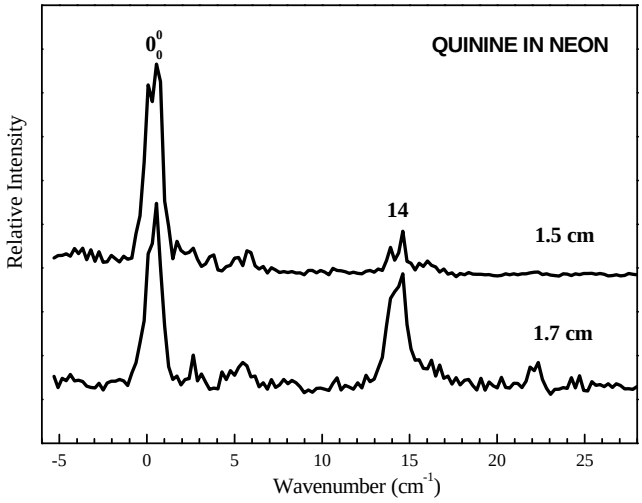

Figure 25: *The variation in intensities of the band at 14 cm^{-1} to the 0-0 transition with change in the distance from the nozzle. Please note the delay between the excitation and ablation lasers has been changed accordingly from 19 to 21 µs.*

A slight change in the cooling conditions has a greater impact on the band at 14 cm^{-1} than on the band origin. For example, Figure 25 shows the same spectrum taken at different distances from the nozzle. A supersonically expanded Neon has a velocity of 7.9 10^4 cm/s. Hence a delay of ~20 µs between ablation

and excitation lasers corresponds to a distance of ~1.7 cm from the nozzle. The distance between the nozzle and the excitation laser has been gradually changed. The delay between ablation and excitations lasers has been modified accordingly so that the excitation laser reaches the shifted ablated molecules. When doing this, the intensity of the +14 cm^{-1} dramatically decreases. This observation holds true for the band at 23 cm^{-1} of Quinidine too. The group of Focsa et al[22] did a similar kind of study on of a frozen aqueous solution of formaldehyde, by changing the delay between the desorption and excitation lasers. They found out that on doing so two ablation regimes have been created. The fast component among the two is named "explosive vaporization" and mainly focuses on the spatial region next to the sample surface where desorbed species exhibit a high number of collisions. This region corresponds to a narrow temperature range. The slower component belongs to a "normal vaporization" regime which can take place in a wider temperature range. We can conclude from our experiments that the +14 cm^{-1} band does not arise from the same ground state as the origin transition. It is either a hot band or a second conformer. This observation will be further complemented with IR-UV double resonance studies as discussed in the next section.

- It is interesting to note that in case of Quinine, except the bands at 5 and 14 cm^{-1} all the other bands above 14 cm^{-1} are located approximately at the same position as Quinidine (Figure 24). Hence the cluster of bands in the low frequency region can be divided into two sets of bands one which is similar for both the molecules and the other containing bands which are different for the two molecules. The fact that there is absence of any vibrational progression is common for both the sets.
- Increase in ablation gives rise to new bands, an example of which is the 55 cm^{-1} band to the blue of the band origin of Quinidine (Figure 26). The figure below depicts the variation in the intensity of this band with change in cooling conditions. In this case a change in cooling conditions is introduced either by changing the power of ablation laser or changing the nature of matrix used in the pellet. The black and green plots have been recorded using graphite as matrix with high and low power of ablation respectively. As shown in the spectra below, an increase in ablation power increases the intensity of the band at 55 cm^{-1}, while at low power it is hardly observed. Next the same scan

is repeated with a matrix containing C-black which has been tested to yield cold bands with high signal to noise ratio at low ablation power. So, the spectrum given in red depicts primarily the bands arising from cold species in the jet. However, one cannot proceed further with this pellet as C black renders it brittle and hence it has a very short life-time (approximately 30 minutes). As observed in the red spectrum, the band at 55 cm^{-1} does not appear thereby indicating that it is an example of hot band which appears only in a hot supersonic jet.

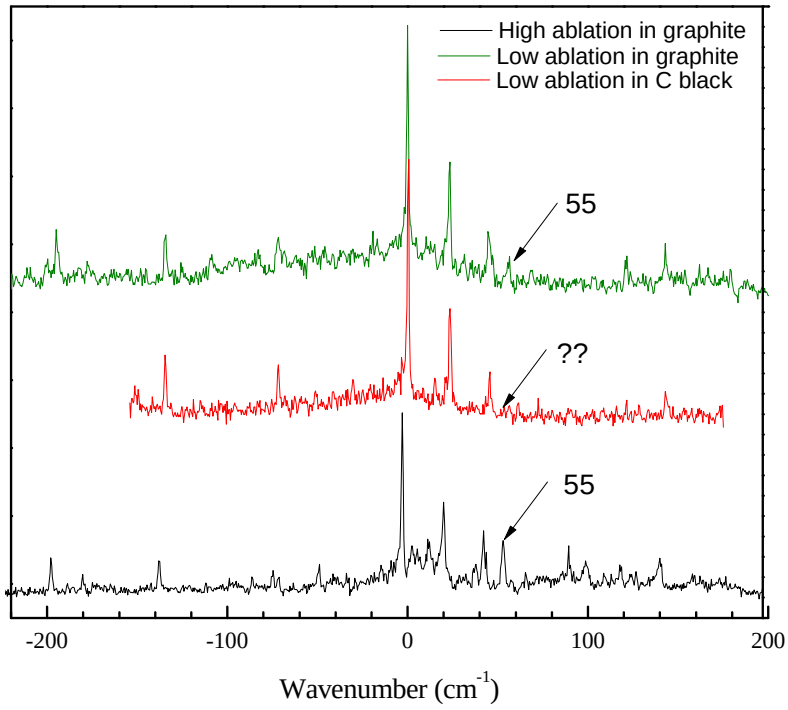

Figure 26: *LIF excitation spectrum of Quinidine with graphite and carbon black as matrix elements. The green and black plots denote high and low ablation respectively on a pellet made of graphite and Quinidine.*

IV.2. Laser Induced Fluorescence Emission

Just like in REMPI, in LIF the entire set up is tested first with naproxen before proceeding towards Quinine. Hence the low-resolution fluorescence emission spectrum below (Figure 27) compares the emission intensity of the three molecules Naproxen, Quinine and Quinidine. The objective of recording the spectrum is to have an idea about the nature of the emissive state.

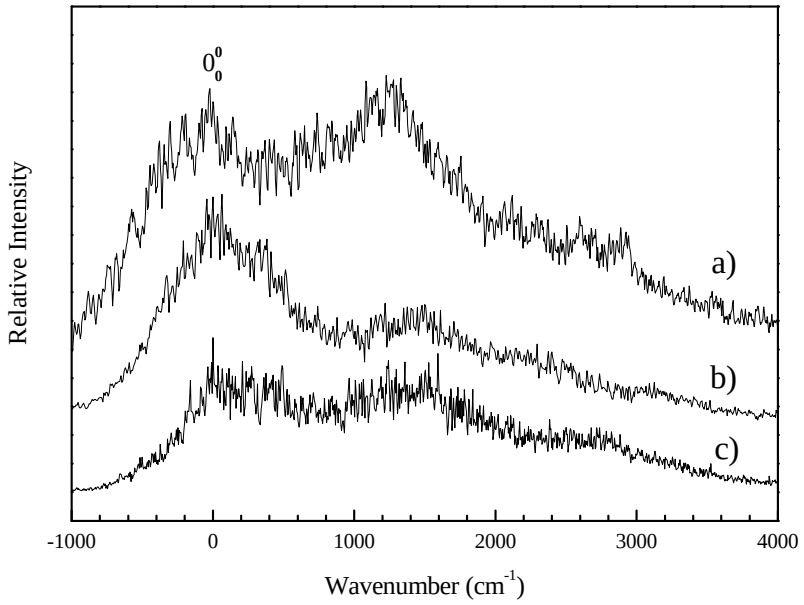

Figure 27: *Low-resolution fluorescence emission spectrum of a) Quinidine, b) Quinine and c) Naproxen, each being excited at its respective 0-0 transition.*

From the above spectrum the following points are observed:

- Naproxen, a 2-Methoxy Naphthalene derivative, emits from a ππ* state (0-0 transition of the most stable isomer being 30594 cm^{-1}). It is observed that for each of the three molecules the emission maxima lies in the region 1300-1400 cm^{-1}, which is characteristic of the S_0-S_1 spectrum (ππ*) of all Naphthalene derivatives (originating from the totally symmetrical $5a_g$ mode).
- Since (S)-Naproxen does not contain any lone pair containing N atoms it does not show any emission due to an nπ* transition. The case of Quinine is quite different in solution as it undergoes a fluorescent charge transfer in presence of polar aprotic solvents.[10] The Stokes shift of this CT emission is about 2000 cm^{-1}. From the low-resolution spectra, it is difficult to assess whether the low-energy part of the emission spectrum is due to this CT emission or to a vibronic band. Indeed from 2000 cm^{-1} onwards and more towards the red

there is a weak emission in Quinine and Quinidine which is not prominent in case of naproxen. As a proof for the observations obtained from low resolution emission spectrum, the following plot in Figure 28 shows the fluorescence dispersed emission for the three molecules Quinine, Quinidine and Naproxen respectively, obtained with a better resolution.

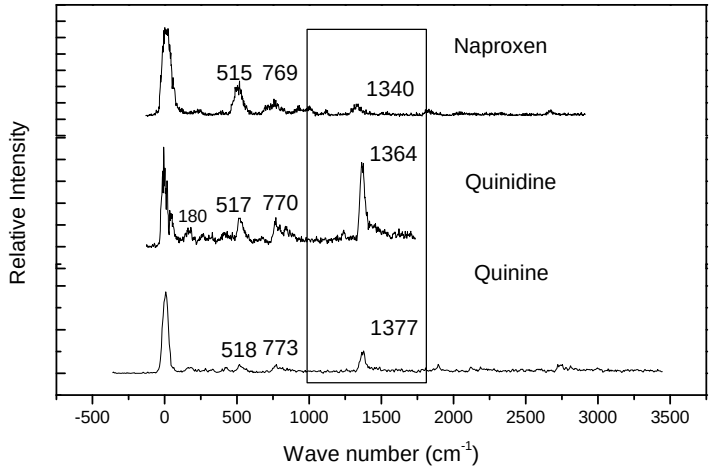

Figure 28: *Dispersed fluorescence emission spectrum of a) Quinine b) Quinidine resulting from excitation of the transition origin. Energies are given relative to the excitation wavelength.*

Since the resolution of the monochromator used to record the fluorescence emission (~90 cm^{-1}) is larger than the difference in wavenumbers of their respective band origin (20 cm^{-1} for Quinine-Quinidine and 75 cm^{-1} for Quinine-Naproxen), the emission bands obtained for all the three molecules are nearly at the same position.

As observed in the low-resolution fluorescence emission spectrum, here too the bands due to the $5a_{1g}$ mode at 1377 and 1364 cm^{-1} for Quinine and Quinidine respectively, are the most intense in the entire spectrum. Among the other vibronic bands observed, the one at ~770 cm^{-1} corresponds to the $8a_{1g}$ transition. While the other at ~ 515 cm^{-1} is most likely to be be the vibration in S_0 of the Hertzberg Teller active mode observed at 467 cm^{-1} in S_1 (Figure 8).

Also, to be noted is the weak emission in the low energy region at 180 cm^{-1} which is counterpart of that observed at ~140 cm^{-1} in S_1. The mode observed at ~280 cm^{-1} corresponds to that at 286 cm^{-1} in the excited state of Quinine.

Quinine S_0	Quinine S_1	Calculated Frequency Quinine	Quinidine S_0	Quinidine S_1	Calculated Frequency Quinidine	Naphthalene	Assignment
	47	53	-	45			Bending along τ_1
180	147	215	180	143	208		Bending of the methoxy substituent
281	288	279	268	286	280		Rocking of the C=C coupled with deformation of Quinuclidine
424		440	433		442		8 b_{1u} by analogy with Methoxy-Naphthalene
518	467	548	511	488	548	508	8 b_{1g}
773	747	769	760		769	761	$8a_{1g}$
1376			1364			1380	$5a_{1g}$
1905						1893	$8b_{1g}$ $5a_{1g}$
3619		3821	3619	-	3822		ν(OH)stretch

Table 2: *Main vibrations of Quinine and Quinidine in their ground and electronic excited state. Calculated frequencies are not scaled.*

The principal transitions observed in the fluorescence excitation and the dispersed fluorescence emission spectra of Quinine and Quinidine have been listed in the following table together with their assignment and calculated values. Due to similarity in the structure of the chromophore, most of the transitions due to vibrations localised on the aromatic ring match with those observed in Naphthalene and 2-Methoxynaphthalene[9]. The band due to the $5a_g$ mode at 1376 and 1364 cm^{-1} for Quinine and Quinidine stands out as the most intense in the studied region of the dispersed fluorescence spectra. The other observed vibrational modes correspond to the Naphthalene $8a_{1g}$ transition at ~770 cm^{-1}. The ~510 cm^{-1} mode is the counterpart in S_0 of the Hertzberg-Teller active $8b_{1g}$ mode observed at 467 cm^{-1} in S_1.

IV.3. Vibrational Spectroscopy In Gas Phase: An IR-UV Double Resonance Study

The results from the electronic spectroscopy experiments are not sufficient enough to properly assign a structure to the observed species and to know whether the low-frequency bands observed in the LIF spectrum are due to conformers or hot bands. Hence the following part is devoted to the IR-UV double resonance studies on Quinine and Quinidine.

IV.3.a. Quinine

The IR-UV double resonance spectrum of Quinine has been recorded by setting the UV probe at the electronic band origin (30621 cm^{-1}) and scanning the Infrared pump laser in the ν(OH) and ν(CH) stretch modes region. Unlike the case of Naproxen, the IR-UV signal for Quinine is much less intense. While an increase

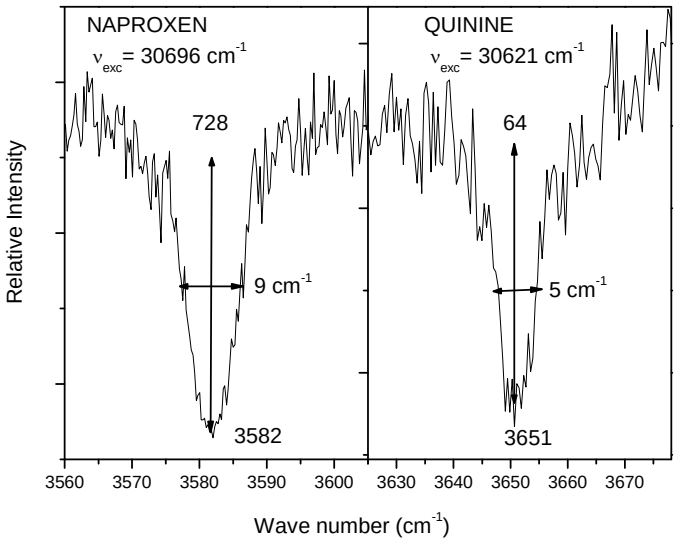

Figure 29: *Difference in IR-UV depletion intensities and FWHM of naproxen and Quinine.*

in ablation power can increase the UV signal intensity in Naproxen, maintaining an intense depletion, the same is not observed in Quinine. A slight change in the ablation conditions is enough to decrease the depletion efficiency in case of Quinine. As the depletion efficiency is very sensitive to the fact that the molecule is cold or not, we can conclude from this observation that it is difficult to have a cold jet of Quinine.

The Figure 29 above compares the depletion intensities of Naproxen and Quinine. In fact, Naproxen shows a dip which is easily saturated, with a percentage of depletion reaching 100% in good cases. In contrast, the percentage of depletion hardly reaches 40% for the ν(OH) stretch of Quinine, which is

expected to have similar oscillator strength as that of Naproxen. Also, the dip for Naproxen is more saturated with a half width maximum of about 9 cm^{-1} compared to Quinine (5 cm^{-1}).

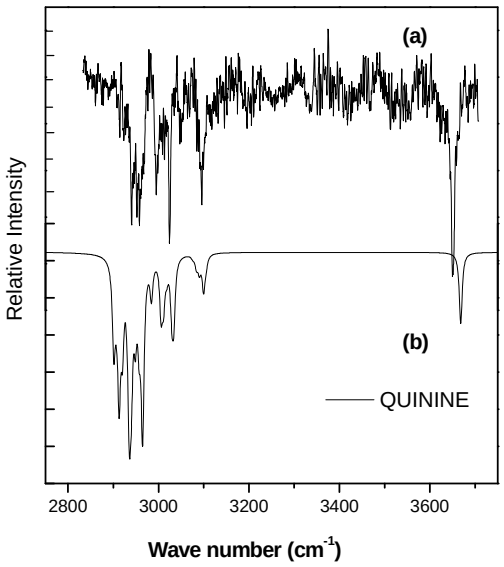

Figure 30: *(a) Experimental IR spectrum obtained with the probe set on the origin transition of Quinine. (b) calculated spectrum obtained at the 6-31+G(d,p) level of theory and scaled by a scaling factor of 0.96 for the cis-γ-open(3) conformer of Quinine.*

As shown in Figure 30 (a) the IR depletion is observed for a single band at 3651 cm^{-1} in the free OH region, as expected for a single OH oscillator containing molecule. The Figure 30(a) below shows that the OH region is more intense than the CH region. This is due to the power of the IR laser used which is higher in the OH stretch region compared to the other. Also, the region of the CH stretch modes is quite congested in contrast to the former. The aromatic CH absorb around 3096 cm^{-1}, followed by a cluster of bands in the aliphatic CH region at lower energy, absorbing at 3024, 2995, 2954 and 2941 cm^{-1}.

The ***ν(OH) stretch region*** of Quinine has been studied in two different ways:

As discussed in the earlier section the bands at +5 and +14 cm^{-1} are the points of difference between Quinine and Quinidine. Hence in order to probe whether it is due to an absorption by a conformer specific to Quinine or a hot band, the low-frequency region of the UV excitation spectrum (Figure 24 (a)) has been studied. First the UV pump laser is fixed at each excitation band and then the IR pump laser is scanned in the the free OH wavelength region.

***UV fixed at band origin, +5, +14 cm $^{-1}$ and the background*:**

The following Figure 31 shows the IR depletion spectrum of Quinine with the UV fixed at the electronic band origin (30621 cm $^{-1}$) and at 5 and 14 cm^{-1} to its blue as well as at the background at +9 cm^{-1}. The sole intention of placing the bands at these positions is to verify whether the bands that are absorbing at the free OH wavelength is really cold or always has a contribution of absorption by the background in them.

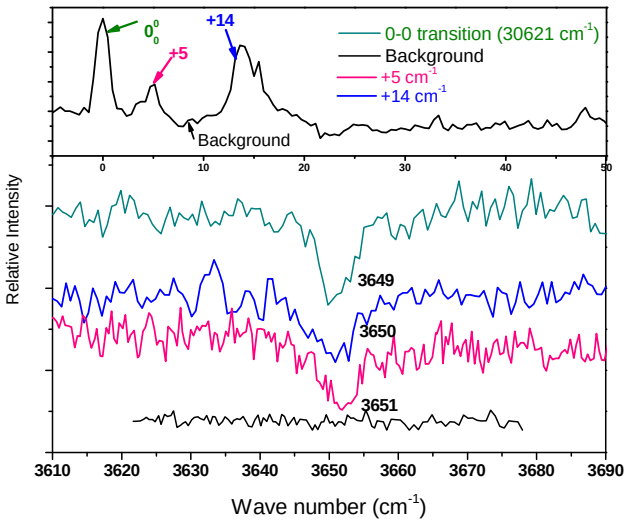

Figure 31: *The spectrum above is a fluorescence excitation spectrum of Quinine in the first 50 cm^{-1} from the band origin. The plot below is the IR-UV double fluorescence with the UV fixed at the band origin, +5, +14 cm^{-1} and the background of the excitation spectrum. The IR has been scanned in the ν(OH) region.*

It is interesting to note that the efficiency of depletion induced by the IR decreases as the UV laser is moved from the band origin to the band at +5 cm^{-1}. However the depletion of UV signal kept at the band origin and at +14 cm^{-1} are nearly the same. The background shows no absorption in this range. All the three intense bands in the UV spectrum absorb the IR laser around the same wavelength, *i.e.* 3651 ± 2 cm^{-1}. A band much to the red of the band origin at -196 cm^{-1} was also probed in the same manner as the bands in the low frequency region. For it too, the IR absorption is nearly at the same position (3654 cm^{-1}).

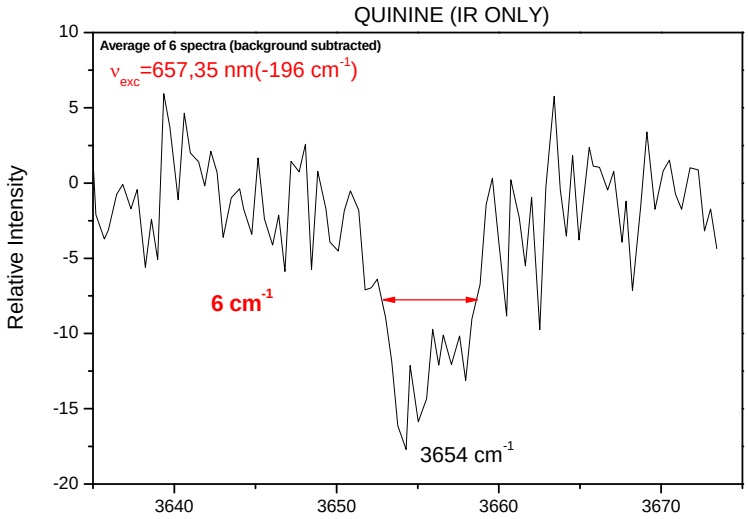

Figure 32: *IR-UV depletion spectrum of Quinine with UV fixed at the band 196 cm^{-1} to the red.*

Since they absorb exactly at the same IR wavelength (3651 ± 2 cm^{-1}) it can be said that they arise from the same conformer of Quinine, or at least conformers with same ν(OH) stretch frequencies.

The second method of studying the ν(OH) region is by keeping the IR wavelength fixed at 3648 cm^{-1} (slightly to the red of the actual free OH wavelength) and then probing the UV laser from the band origin towards 150 cm^{-1} to the blue. As hot bands tend to absorb slightly more to the red than cold ones, the differences we'll observe, if any, will tell us whether these bands are hot bands or not. The following Figure 33 is such an example. From the figure it can be said that the band origin and the one at +14 cm^{-1} undergo 50% depletion, while the band at +5 cm^{-1} depletes totally. It is hard to conclude the fate of the bands at 47 and 147 cm^{-1} because of their weak intensity.

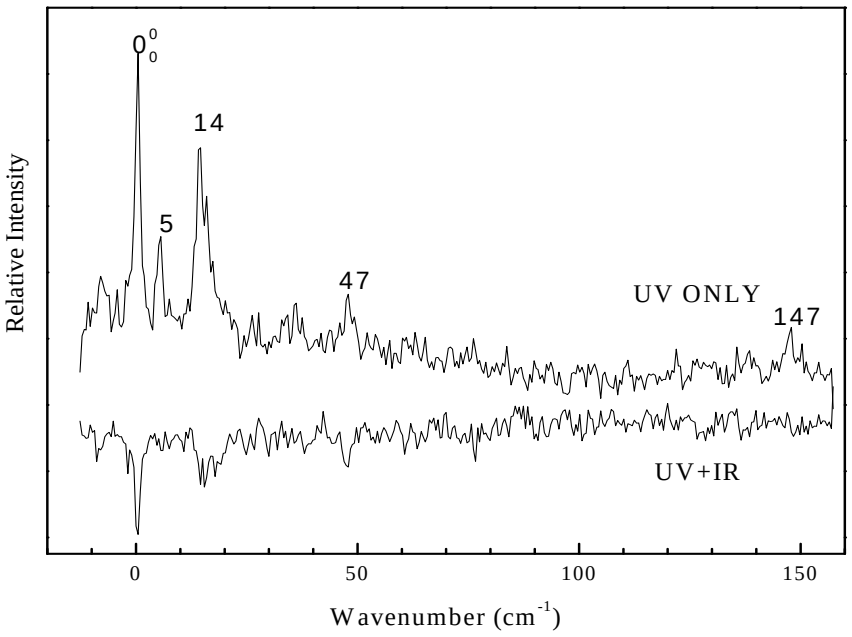

Figure 33: *Comparison between the S_0-S_1 excitation spectra obtained with and without IR laser present. The IR probe is set slightly to the red of the ν(OH) stretch mode frequency, at 3648 cm^{-1}.*

The ***ν(CH) stretch region*** is congested compared to the ν(OH) region and has been studied in the following way:

The UV excitation spectrum of Quinine in the low frequency region (200 cm^{-1} to the blue of the electronic band origin) does not show any vibrational progression. If these bands correspond to different species, it is interesting to find out whether the three most intense bands in this region (0^0, +5 and +14 cm^{-1}) also absorb the IR at different wavelengths. Since the ν(CH) region has a cluster of bands, it is useful to study the above mentioned difference in detail.

The following plot (Figure 34) shows the IR absorption in the ν(CH) range (2830 to 3130 cm^{-1}) with the UV fixed at the electronic band origin first followed by the two bands at +5 and +14 cm^{-1}. The plot shows that the UV excitation bands at 0-0 and +5 cm^{-1} absorb the IR laser differently at 2993 and 2998 cm^{-1}. Thus they seem to belong to two different conformers. However, the band at +14 cm^{-1} shows a broad absorption in the entire range 2980-3000 cm^{-1} making it difficult to conclude whether it is the same as any of the two conformers, a contribution of both, or a hot band. As mentioned earlier, the broadening might be related to the fact that it is sensitive to the cooling conditions of the jet.

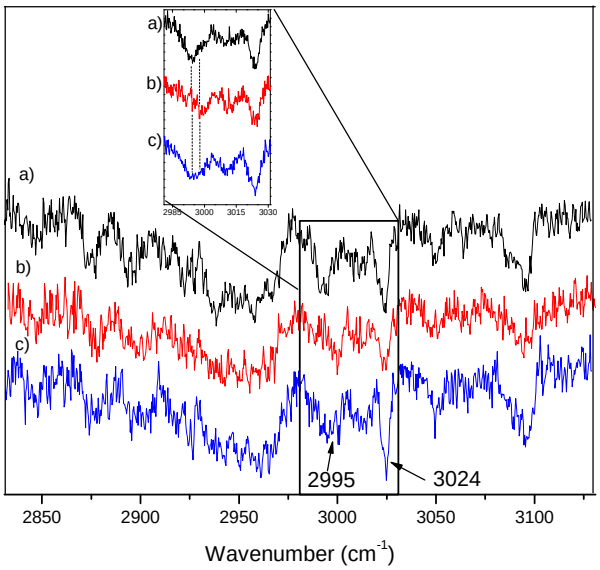

Figure 34: *The plot shows the comparative study of C-H stretch mode region (2800-3130cm^{-1}) for UV excitation at a) 0, b) +5 and c) +14 cm^{-1} of Quinine.*

As shown in the Figure 34 above, in the ν(CH) stretch region most intense absorption is obtained at 3024 cm^{-1}, a value which is common to the three spectra recorded by setting the probe on 0-0, +5, and +14 cm^{-1}. In contrast, the band at 2995 cm^{-1} appears more strongly in the spectrum obtained when probing 0-0, +14 cm^{-1} than when probing +5 cm^{-1}.

To confirm this observation, it is necessary to probe the three bands at the same time, getting rid of the possible fluctuations of the source. Hence once again we use the technique of fixing the IR at 3024, 2995 cm^{-1} and scan the UV near the band origin. The Figure 35 is an example of such a scan.

The Figure 35 shows that the bands at 0-0 and +14 cm^{-1} absorb the IR wavelength approximately in the same ratio. For the small band at +5 cm^{-1} there is 50% depletion at λ_{IR} =3024 cm^{-1}, just like the other two. For the IR absorption at λ_{IR} =2995 cm^{-1} it is difficult to conclude as the band is hardly visible in the channel containing only the UV signal. Thus the point to be noted is at an intense absorption wavelength of IR there is same magnitude of depletion for all the conformers.

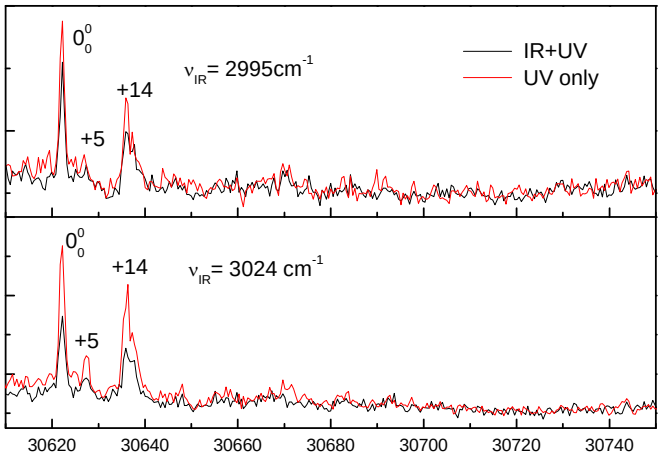

Figure 35: *Comparison between the absorption intensities fixed at two different IR wavelengths of the pump IR laser (2995, 3024 cm^{-1}) with the UV scanned near the electronic band origin.*

IV.3.b. Quinidine

The entire IR depletion spectrum for Quinidine is shown in Figure 36.

In order to test whether the depletion efficiency is better with a different matrix, the IR-UV spectrum has been recorded with a pellet containing C-black and Quinidine. Carbon-black ablates faster than graphite, thereby forming a larger plume containing Quinidine and a colder jet within a short span of time. However, since it is more sensitive to ablation, it decreases the lifetime of the pellet. In the plot shown above short scans have been done in the CH and OH stretch regions, 2890-2960 cm^{-1} and 3620-3700 cm^{-1} respectively. Indeed, in both graphite and C-black, Quinidine absorbs the IR wavelength at 3650 ± 2 cm^{-1} in the ν(OH) stretch range along with a congestion of bands between 3100-2895 cm^{-1} in the ν(CH) region. The bands appear broad in both the probed regions. Hence although being a faster source of a cold jet, carbon black fails to show IR-UV depletion with low bandwidths and hence has not been used much in our experiments.

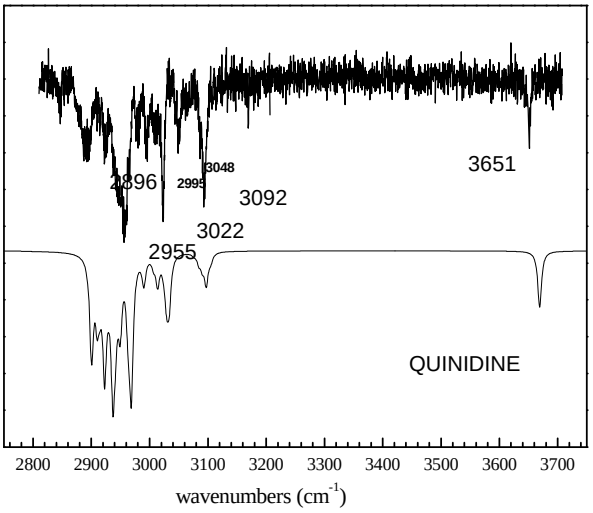

Figure 36: *IR depletion spectrum for Quinidine in graphite matrix.*

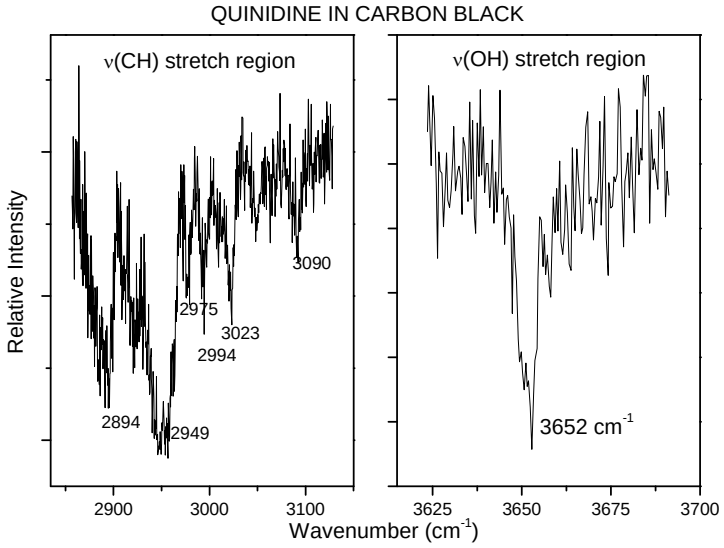

Figure 37: *IR depletion spectrum of Quinidine mixed with Carbon black, in the ν(OH) stretch range (top) and in the ν(CH) region (bottom).*

Just like Quinine, its pseudoenantiomer Quinidine also absorbs intensely in the ν(OH) and ν(CH) wavelength. However the absorption intensity in the ν(OH) region seems to be lesser than Quinine. Here too, a detailed study has been done in all the intense bands present in the low frequency region of the UV excitation spectrum. They follow the observation of Quinine mostly by absorbing at nearly the same Infrared wavelength. It is also interesting to note, that when a band at much higher frequency and far from the band origin like the band at +747 cm^{-1} is

studied, it also shows the same wavelength of absorption in the ν(OH) region, which confirms their assignment to vibronic transitions arising from the same ground-state species.

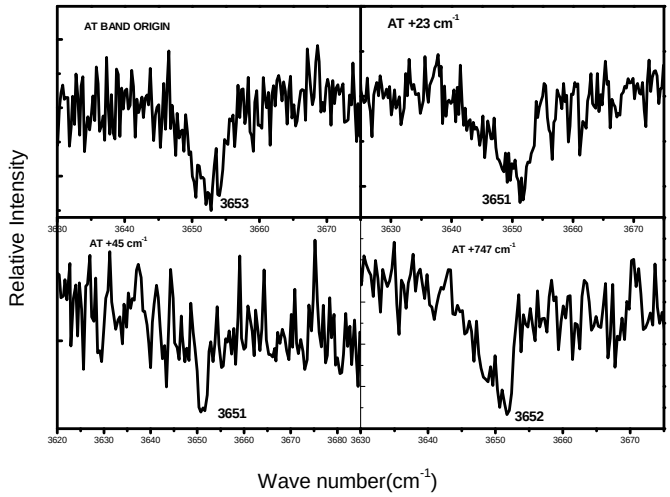

Figure 38: *The IR-UV double fluorescence of Quinidine with the UV fixed at the band origin, +23, +45cm^{-1} and at a band to the extreme blue (747 cm^{-1}) of the excitation spectrum. The IR has been scanned in the ν(OH) region.*

The other bands to the blue are too weak in intensity, and hence depletion if any, lies within the background.

The following plot (Figure 39) depicts the IR depletion spectrum in the range (2830-3135 cm^{-1}) with the UV fixed at the above mentioned three wavelengths.

From the above plot it is observed that at all the three probed wavelengths the IR absorption is relatively similar, except a minute difference at 2923 cm^{-1}. In order to verify if it's really true, the two bands at 0-0 and +23 cm^{-1} have been scanned in the small region (2890-2960 cm^{-1}), three times each and then averaged. This way it is confirmed whether the dip in the wavelength appear always or not.

Clearly the spectrum given in Figure 39 confirms the fact that there is no difference in IR absorption for all the three bands (0-0, +23 and +45 cm^{-1}) in the UV excitation spectrum (Figure 24 (b)). Hence they indeed come from the same conformer.

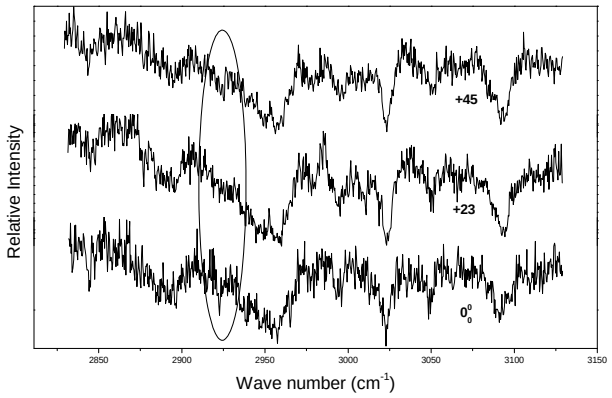

Figure 39: *IR absorption in the ν(CH) range with UV fixed at the band origin, +23 and +46 cm-1.*

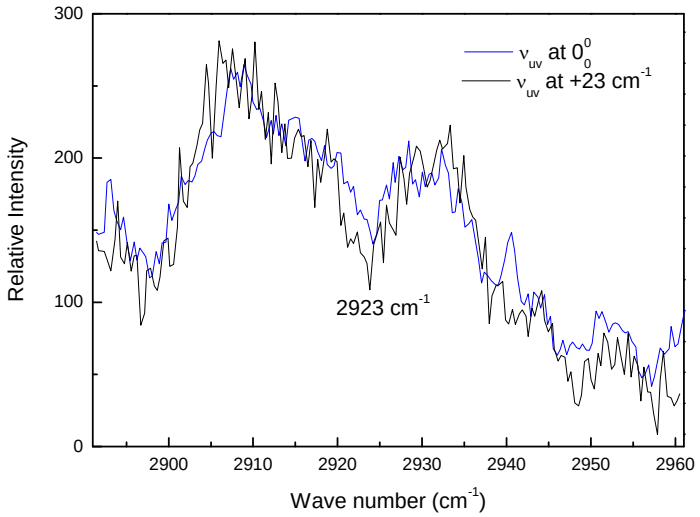

Figure 40: *Averaged spectrum of scans done in the IR wavelength region (2890-2960 cm-1), keeping UV fixed at the electronic band origin and at +23 cm-1.*

IV.3.c. Comparison with calculated results

The differences in the IR-UV absorption of the low frequency bands of Quinine can be due to absorption by a different conformer.

If the above hypothesis is true, then these differences should be visible in the spectra calculated for Quinine in gas phase. The following Figure 41 shows the calculated spectra of the most stable conformers of Quinine and that of Quinidine.

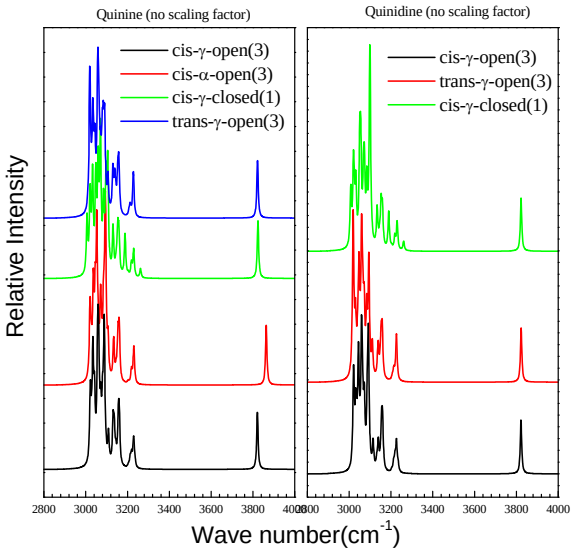

Figure 41: *Calculated spectra of the most stable conformers of Quinine and Quinidine in the gas phase.*

In the case of Quinine, the ν(OH) absorption takes place at a wavelength 3822 cm^{-1} which is true for all the γ conformations of Quinine irrespective of the fact whether they are open or closed, *cis* or *trans*. An exception is observed in the α conformer, which absorbs at a slightly high ν(OH) frequency (3863 cm^{-1}). The reason behind this shift is due to the geometry of the two conformers. The lone pair of O-H in the chiral linker points towards the Quinoline ring and hence can interact with the hydrogen atom of the $C_{3'}$-H bond in the α conformer. This is not true for the γ conformer as the O-H lone pair is above the plane of the Quinoline ring and hence cannot take part in any intramolecular H bonding. This is reflected by a shorter distance (2.35 Å) in α relative to γ (2.47 Å). This explains the small blue shift in the ν(OH) stretch of α relative to the γ conformer. However, no such shift has been observed in the experimental spectra thereby confirming the fact that all the major absorption frequencies in the UV excitation spectrum are due to only γ conformers.

As observed in the experimental ν(CH) stretch region of Quinine, in the calculated ones too there exists slight differences in absorption by different conformers. Unlike the earlier case, the differences in this region are characteristic of the *open* or *closed* geometry of the conformers. For e.g a band is observed at 3190 cm^{-1} belonging to the closed form which is absent in the other

open conformers. Thus the differences if any are observed mostly due to the $C_{3'}H$ stretching mode.

In case of Quinidine, the ν(OH) absorption is at the same wavelength of 3822 cm^{-1} (calculated) and 3651 cm^{-1} (experimental) for all the conformers. The difference in frequencies is because the calculated frequency has been shown without considering a scaling factor. It is interesting to point out the fact that the differences in IR absorption in the two molecules Quinine and Quinidine are more due to the conformation characteristic to the most stable conformer than the pseudo-enantiomerism involved in the two molecules.

Despite the fact that we cannot completely rule out the possible existence of more than one conformer of each molecule in the gas phase, we have tentatively assigned the bands near the origin band to hot bands. However, calculations have predicted the existence of higher-energy conformers, which could be observed at room temperature. One hopes to find out whether these conformers exist in solution, and whether their existence manifests itself in the VCD spectra.

IV.4. Vibrational Circular Dichroism

Optical enantiomers have equal in magnitude and opposite in sign absorption in VCD. We want to see whether this relation holds for pseudo enantiomers. To do that, we have to compare the experimental spectra to those simulated. We will first recall the limits of such simulations

- A good rapport between calculated and experimental spectra is obtained when the calculations done take into account all the conformers present in the solution.
- However, differences are observed when comparing experimental and calculated VCD spectra. These differences arise from mostly due to change in the sign and magnitude of the rotational strength of the normal modes. Detailed theoretical studies have found out that[23] :
    1. Not all normal modes exhibit a change in sign of their rotational strength in the same manner.
    2. The same perturbation can induce either a change in sign or a change in magnitude of the rotational strengths.

The rotational strength of a given normal mode *i*, is actually a dot product of electric and magnetic dipole transition moment and so it depends on the magnitude of the angle between the two vectors. As this angle approaches 90 degrees, the slightest perturbation can change it beyond 90 degrees, thereby resulting in a change of sign. Such normal modes with the angle close to 90 degrees are known as non-robust modes. While those with angles far from 90 degrees are not perturbed by slightest perturbations are known as robust modes. The presence of these modes in case of Quinine has been discussed later in the assignment section following the plots below.

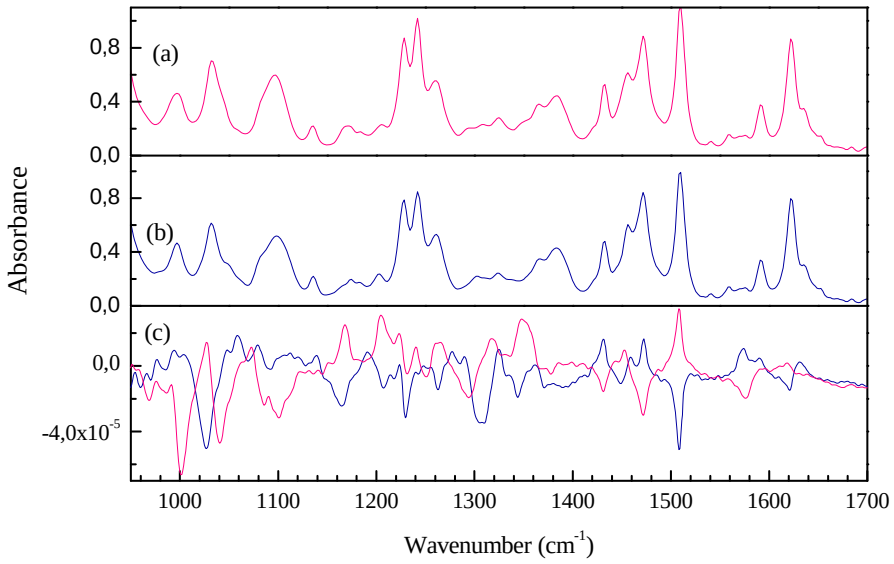

Figure 42: *Comparison of the VCD and IR spectra of the measured Quinine molecule and its pseudoenantiomer Quinidine.*

(a) IR absorbance in the fingerprint region of a solution of pure Quinine in $CDCl_3$ solvent.

(b) IR absorbance in the fingerprint region of a solution of pure Quinidine in $CDCl_3$ solvent.

(c) Comparative study of the VCD spectrum of the two enantiomers.

The Figure 42 (a) and (b) below depicts the IR absorbance spectra of (–) Quinine (8S,9R) and (+) Quinidine (8R,9S). For each spectrum the absorbance from the solvent $CDCl_3$ has been subtracted. The differences if any between Quinine and Quinidine is not observed in the Infrared absorption spectra. In fact, they are identical to each other, just like true enantiomers.

Figure 42 (c) is the VCD spectrum of Quinine and Quinidine in the fingerprint region (1350-1700 cm^{-1}). As observed in the plot, the characteristic

mirror image relationship of enantiomers exists between 1320-1640 cm^{-1}. Moving towards the red, from 1300 cm^{-1}, this relationship is partially lost.

Figure 43 is a comparative study between the experimental VCD spectra for Quinine and Quinidine with their respective calculated one. The calculations have been done in presence of $CHCl_3$ solvent. In case of Figure 43(b) the calculated spectrum (red) is actually a weighted average of the two most predominant conformers of Quinine in solution phase.

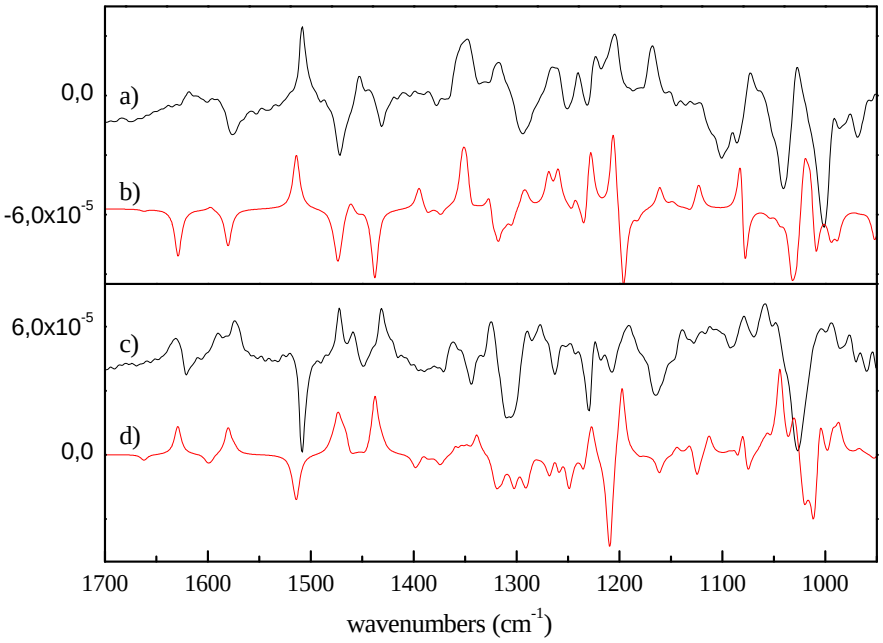

Figure 43: *Comparison of observed and calculated VCD spectra of Quinine and Quinidine.*

a) experimental VCD spectrum of Quinine,

b) calculated VCD spectrum of Quinine; the Boltzmann average of two lowest energy conformers have been considered.

c) experimental VCD spectrum of Quinidine,

d) calculated VCD spectrum of Quinidine; the Boltzmann average of five lowest energy conformers have been considered.

The frequencies have been scaled by a scaling factor of 0.98.

Compared to Quinine, the number of stable conformers is greater (five), in case of Quinidine. A weighted average of these five conformers results in the red spectrum as shown in Figure 43 (d).

IV.4.a. Assignments of bands in the VCD spectra

Assignments will be done starting from the region showing good mirror image relationship (1350-1700 cm^{-1}). Here the intense peak at 1577 cm^{-1} corresponds to an in-plane bend of the Quinoline ring. Again, the intense peak showing good mirror image symmetry at 1506 cm^{-1} originates from a CH in-plane bending mode of the Quinoline moiety. These in-plane CH bending modes have also been shown to be optically active in benzene derivatives.[24] Moving more to the red, the vibrations at 1471 and 1438 cm^{-1} are mainly due to bending of the methyl group of OMe attached to the 6' position of the Quinoline ring. Hence these vibrations occur far from the chiral centre. In fact the activity of such asymmetric C-H vibrations of methoxy group have also been observed in carbamoylated Quinine and Quinidine derivatives.[25]

The situation becomes a little complex below 1300 cm^{-1}. Here, there is a partial loss of mirror image relationship. A lot of modes in this region are completely delocalized on the entire molecule, but some of them are localized on the Quinuclidine ring. However, the band at 1169 cm^{-1} can be marked as an exception and it corresponds to a bending mode localized on the chiral linker.

Calculations on the vibrational circular dichroism properties of complex molecules by the group of Nicu et al [26] brought forward the predominance of non-robust modes in Quinine. In fact, out of 132 total modes, only 9 are robust with two of them lying in the fingerprint region. As calculated by them, such a non-robust molecule can undergo change in the sign and magnitude of rotational strength by slightest changes in the experimental conditions or in the method of calculation used. So, the discrepancy between the calculated and experimental plots below 1200 cm^{-1} in Figure 23 might arise from the functional used in the calculation or the difference in intensities of the two robust modes in the conformers present in solution.

The observation to be noted comes as a contrast to the results obtained by the group of Nicu et al which postulated that modes far from the chiral center behave like achiral modes. In case of Quinine, an intense normal mode far from the chiral centre does not behave identical to an isolated achiral group on which the mode is localized. In fact the vibrations observed are dependent on the chirality of the whole molecule. The band at 1506 cm^{-1} testifies the last statement. It being CH bending mode located on the non-chiral aromatic ring still

shows a strong VCD intensity and good mirror-image relationship between Quinine and Quinidine.

V. DISCUSSION

V.1. Existence of several isomers in the gas phase

The detailed study on the possible stable conformations of Quinine and Quindine in gas phase leads to the observation that for both the molecules the cis-γ-open(3) structure attains the highest stability. Thus the next question arises regarding the different bands in the low frequency region of the two molecules which are characteristic of each molecule. The origin of such weak bands within 200 cm^{-1} to the blue, has been discussed below taking two viewpoints:

V.2. From the electronic spectroscopic point of view

The congested bands in the low frequency region might arise from a coupling between the $S_1 \leftarrow S_0$ transition and a close lying transition. The validity of such a hypothesis can be explained in the following ways:

- The chromophore of the studied molecule being a Quinoline ring, is expected to show a close-lying weak nπ* from Quinuclidine nitrogen to the aromatic ring, and a strong L_b ππ* transitions in the gas phase within the range of 300-320 nm.[27], along with a L_a transition at higher energy. Since coupling with the L_a transition has been observed much higher in energy, above 2000 cm^{-1}, in β-substituted Naphthalene derivatives, it is not likely that it can be responsible for the congestion of bands we observe here.
- In order to know whether the nπ* transition of an electron from the lone pair of Quinoline nitrogen to the lowest π* orbital of the aromatic ring takes place, it is important to know the energy difference between the nπ* and ππ* transition. Earlier studies reveal that ππ* transition dominates the absorption spectrum in condensed phases as well as rare gas matrices due to the weak oscillator strength of the nπ* transition.[28] [29] Moreover, substitution of the Quinoline ring lowers the ππ* transition energy without affecting the nπ* transition as observed in Hydroxy-Quinoline derivatives[11]. One therefore expects that the

lowest-energy transition of Quinine is the ππ* transition, because of the presence of the OCH_3 substituent. Indeed, attempts made on recording the $S_0 \rightarrow S_1$ spectrum of Cinchonidine under similar jet cooled conditions remain unsuccessful. Since Cinchonidine has no substituent at the Quinoline ring, it has a high ππ* transition energy thereby supporting the above hypothesis.

- Lastly, there is a possibility of a nπ* transition occurring due to electron transfer from the lone pair of the Quinuclidine nitrogen to the π* orbital of the aromatic ring.[10] For alkaloids similar to Quinine (Dihydroquinidine and 9-Benzylcupreidine) the excited state reached by such a transition is weakly fluorescent and shows a red-shifted emission in toluene (approx. 2300 cm^{-1}). Since no such red-shifted emission have been observed in the gas phase emission of Quinine, this nπ* transition is most likely to lie at higher energy than the L_b transition.

A large molecule like Quinine, which is very flexible around its chiral linker is expected to undergo a lot of torsional movements involving its side chains (Methoxy, Vinyl-substituted Quinuclidine). The low-frequency bands due to such torsional motions are analogous to the 35 cm^{-1} band observed in 2-ethylnaphthalene-methanol.[18] Thus the pair of frequencies at 47 and 147 cm^{-1} (Quinine) and 45 and 143 cm^{-1} (Quinidine) in the experimental spectrum, can be due to such low-frequency modes. Indeed, comparison between observed and calculated frequencies allows assigning the band at 47 and 147 cm^{-1} or 45 and 143 cm^{-1} to the frequencies calculated at 53 and 214 cm^{-1} which correspond to a bending along the τ_1 angle and a coupled motion mixing rotation around the τ_1 angle and bending of the methoxy substituent, respectively (see Table 2). The mode observed at ~280 cm^{-1} in the ground state has been assigned to a rocking motion of the C=C substituent coupled with a deformation of the Quinoline frame.

Last, it is to be noted that the fact that Quinine and Quinidine are very flexible molecules make them much more difficult to ablate and cool down than the test molecule Naproxen® containing a similar chromophore. Hot bands can appear due to insufficient cooling of the laser-ablated species, as well as different isomeric forms. Comparison with the electronic spectra obtained at different jet-conditions and vibrational spectra with the probe set on different bands, allow discussing these hypotheses. It is clear from the dependence of the bands located

at -197, +5, +14 cm^{-1} in Quinine upon the cooling conditions that they correspond to different ground-state species.

V.3. Comparison with calculated structures

The calculated IR-UV spectrum of Quinine shows that the ν(OH) stretch frequency is identical for the different conformers present at room temperature, except the ones with α conformation. Hence it is likely that all the species probed by the lasers belong to the γ conformation irrespective of the *cis* or *trans* position of the OMe substituent or *open* or *closed* nature of the two bulky moieties.

The ν(CH) stretch region is characteristic of the open or closed conformation. Indeed, a band appears at 3230 cm^{-1} in the calculated spectrum of the closed form, which is absent in that of the others. It mainly corresponds to the C_3'H stretching mode. Small differences between conformers also appear below 3140 cm^{-1} which are characteristic of the α or γ conformations, but are difficult to rationalise.

The slight differences observed in the ν(CH) stretch region, makes the UV absorption at 5 cm^{-1} an ideal case to discuss about the origin of low frequency bands. According to the calculated spectra, the only other conformer apart from the most stable one which shows a spectrum in the ν(CH) stretch region compatible with the experimentally observed one is the trans-γ-open(3). This particular conformer absorbs two bands at the aliphatic C-H stretch mode region (3072 and 3122 cm^{-1}), differently compared to the cis-γ-open(3) conformer. However this band at 5 cm^{-1} is less likely to belong to this conformer due to the following reasons:

- Calculations of the transition energies at the TD-DFT level for the two conformers, give a difference of transition energies more than 1000 cm^{-1}, with the trans conformer always at a higher energy compared to the cis-γ-open(3)[9].
- Moreover, in Methoxy naphthalene, the electronic origin transitions of the *cis* and *trans* conformers are separated by ~660 cm^{-1}, which is much larger than the 5 cm^{-1} observed in case of Quinine[9].

These two arguments are not in favour of the assignment of the 5 cm^{-1} band to the *trans*-γ-open(3). The other possibility is that the 5 cm^{-1} band corresponds to a hot band, with vibrational energy deposited in modes either

located on the CH or coupled with the ν(CH) stretch, which explains the different spectroscopic fingerprints.

Next, we have assigned the band located at +14 and -197 cm^{-1} to hot bands. Indeed, despite peaking on the same wavelength as that of the cold 0-0 transition, their spectrum is slightly broader than that obtained when probing the transition origin, which is typical of hot bands. Lastly it should be mentioned that either the bond at +5 cm^{-1} or at +14 cm^{-1} are observed in the vicinity of higher energy vibronic bands. This tends to confirm their assignment to hot bands.

All the bands probed for Quinidine show the same vibrational spectrum in the ν(CH) and the ν(OH) stretch regions as well, which indicates that either Quinidine only shows one conformer in our experimental conditions. The +23 cm^{-1} band has been assigned to a hot band using the same arguments as discussed before.

V.4. Manifestations of Pseudo-enantiomerism

As we have seen above, the additional band observed at +5 cm^{-1} in Quinine might arise from a higher energy conformer, despite this hypothesis being not likely. It is difficult to give a quantitative interpretation of the presence of two isomers in the gas phase for Quinine and only one for Quinidine, but calculated energetics give the same trend. To do that, we would have to know the pre-expansion temperature (temperature of the ablation source). It has been estimated to ~560°C by measuring the ratio between the two isomers of a known molecule, Naproxen ®, put in the gas phase with the same ablation source. However, even at temperatures higher than the room temperature used in this work to define the ΔG hence the relative abundances of the conformers, it is difficult to explain the differences between Quinine and Quinidine by their gas-phase thermodynamics. The differences arise probably more from their properties in the condensed phase. Quinidine is much easier to ablate than Quinine, which is probably due to the structure of its crystal. Indeed, crystallographic measurements show different packing properties between Quinine and Quinidine[30]. It is therefore possible that Quinidine is colder in the expansion than Quinine, because it can be ablated with lower ablation power.

VCD spectra show more differences between the two pseudo enantiomers than IR or UV absorption results do, especially in the region below 1300 cm^{-1}. This is the region in which vibrational modes localised on the alkaloid sub-units are to be found. As two of the chiral centres of the alkaloid subunit are identical in the two pseudo enantiomers, it is not surprising that these modes don't obey mirror image relation in the VCD spectra. Moreover, the region below 1300 cm^{-1} also contains modes completely delocalised on the whole molecular frame. These modes are expected to be sensitive to long-range stereochemical effects.

VI. Conclusion

Quinine and its pseudo enantiomers Quinidine have been studied in the gas phase as well as in $CDCl_3$ solutions. They display very similar spectroscopic properties, with S_0-S_1 spectra shifted from each other by 20 cm^{-1} only. Both of them are very flexible molecules, the S_0-S_1 spectrum of which shows numerous hot bands and low-frequency modes. The lowest-energy transition is located on the Quinoline ring and is typical of the ππ* transition common to 2-substitued Naphthalene derivatives. No evidence for an nπ* charge-transfer state has been evidenced in the gas phase, which makes Quinine or Quinidine weakly fluorescent in isolated conditions. This contrasts with what was observed in solution; the presence of a solvent seems therefore to be mandatory for the CT state to be stabilised.

In the gas phase, the most stable conformer is the *cis*-γ-open(3) form for both the molecules. The vibrational pattern in the 3 μm region is similar in the two molecules. The same isomer is *cis*-γ-open(3) is the most stable form for both molecules in $CHCl_3$ solution and the IR spectra of Quinine and Quinidine recorded in the fingerprint region are identical.

However, the two pseudo-enantiomers show some slight spectroscopic differences. Quinidine is experimentally easier to ablate and shows only the dominant *cis*-γ-open(3) conformer in the gas phase. An ambiguous band which has been assigned either to a *trans*-γ-open(3) conformer or more likely to a hot band has been observed for Quinine. The differences in the gas-phase spectroscopy of the two pseudo enantiomers is not thought to arise from the gas-phase thermodynamics but more to different solid-state structures which result

to different ablation efficiency. More pronounced differences between the pseudo-enantiomers appear in solution than in the gas phase. While Quinine mostly exists in the *cis*-γ-open(3) form in $CHCl_3$, conformers of higher energy are stabilised too in the case of Quinidine. Moreover, while the VCD spectra of Quinine and Quinidine show good mirror-image relation in the range above 1300 cm^{-1}, the mirror-image relation is lost in the range below 1300 cm^{-1}, especially for the deformation modes located on the alkaloid sub-unit.

The proposed explanation of the difference between the two pseudo enantiomers by a larger flexibility of Quinidine is therefore true in condensed phase but does not hold in the gas phase. The spectroscopic manifestations of pseudo-enantiomerism are in the case presented here very tiny, which contrasts with other systems, both neutral and ionic[31]. This is probably due to the fact that the asymmetric centres the chirality of which is not changed are located on a very rigid frame, the alkaloid sub-unit, which is not interacting so much with the rest of the molecule.

VII. References

1 J. F. Lai, Z. Ma, L. Mink, L. J. Mueller, and F. Zaera, Journal of Physical Chemistry B 113 (34), 11696 (2009).

2 T. S. Kaufman and E. A. Ruveda, Angewandte Chemie-International Edition 44 (6), 854 (2005).

3 C. E. Song, *AN OVERVIEW OF CINCHONA ALKALOIDS IN CHEMISTRY*. (September 2009).

4 O. J. Sonderegger, G. M. W. Ho, T. Burgi, and A. Baiker, Journal of Catalysis 230 (2), 499 (2005).

5 N. M. Maier, S. Schefzick, G. M. Lombardo, M. Feliz, K. Rissanen, W. Lindner, and K. B. Lipkowitz, Journal of the American Chemical Society 124 (29), 8611 (2002).

6 D. Scuderi, P. Maitre, F. Rondino, K. Le Barbu-Debus, V. Lepere, and A. Zehnacker-Rentien, Journal of Physical Chemistry A 114 (9), 3306 (2010).

7 D. Scuderi, K. Le Barbu-Debus, and A. Zehnacker, Physical Chemistry Chemical Physics 13 (40), 17916 (2011).

8 K. A. Schug and W. Lindner, Journal of Separation Science 28 (15), 1932 (2005).

9 T. Troxler, B. A. Pryor, and M. R. Topp, Chemical Physics Letters 274 (1-3), 71 (1997).

10 W. W. Qin, A. Vozza, and A. M. Brouwer, Journal of Physical Chemistry C 113 (27), 11790 (2009).

11 F. Lahmani, A. Douhal, E. Breheret, and A. Zehnacker-Rentien, Chemical Physics Letters 220 (3-5), 235 (1994).

12 H. Caner, P. U. Biedermann, and I. Agranat, Chirality 15 (7), 637 (2003).

13 T. Burgi and A. Baiker, Journal of the American Chemical Society 120 (49), 12920 (1998).

14 A. Urakawa, D. M. Meier, H. Rugger, and A. Baiker, Journal of Physical Chemistry A 112 (31), 7250 (2008).

15 L. Alvarez-Valtierra, J. W. Young, and D. W. Pratt, Chemical Physics Letters 509 (4-6), 96 (2011); F. Lahmani, A. Zehnacker-Rentien, L. H. Coudert, and K. A. Zachariasse, Journal of Physical Chemistry A 107 (38), 7364 (2003).

16 F. Lahmani, K. Le Barbu-Debus, N. Seurre, and A. Zehnacker-Rentien, Chemical Physics Letters 375 (5-6), 636 (2003).

17 J. A. Warren and E. R. Bernstein, Journal of Chemical Physics 85 (5), 2365 (1986); F. Lahmani, E. Breheret, A. Zehnackerrentien, and T. Ebata, Journal of the Chemical Society-Faraday Transactions 89 (4), 623 (1993).

[18] A. R. AlRabaa, E. Breheret, F. Lahmani, and A. Zehnacker, Chemical Physics Letters 237 (5-6), 480 (1995).

[19] H. Gattermann. and M. Stockburger., The Journal of Chemical Physics 63 (10), 4541 (1975).

[20] M. Stockburger., H. Gattermann., and W. Klusmann., The Journal of Chemical Physics 63 (10), 4519 (1975).

[21] J. A. Warren., J. M. Hayes., and G. J. Small., Journal of Chemical Physics 80 (5), 1786 (1983).

[22] C. Focsa, C. Mihesan, M. Ziskind, B. Chazallon, E. Therssen, P. Desgroux, and J. L. Destombes, Journal of Physics-Condensed Matter 18 (30), S1357 (2006).

[23] N. J. Nicu VP, Baerends EJ, J Phys Chem A 112 (30), 6978 (2008).

[24] A. Bouchet, T. Brotin, D. Cavagnat, and T. Buffeteau, Chemistry-a European Journal 16 (15), 4507.

[25] O. Julínek., M. Urbanová., and W. Lindner., Analytical and Bioanalytical Chemistry 393 (1), 303 (2009).

[26] V. P. Nicu. and E. J. Baerends., Physical Chemistry Chemical Physics (2009).

[27] Atsunari Hiraya, Yohji Achiba1, Katsumi Kimura, and E. C. Lim, Chemical Physics Letters 185 (3-4), 303 (1991).

[28] C. Crepin, V. Dubois, F. Goldfarb, F. Chaput, and J. P. Boilot, Physical Chemistry Chemical Physics 7 (9), 1933 (2005).

[29] M. F. Anton and M. Nicol, Journal of Luminescence 18-9 (JAN), 131 (1979).

[30] B. J. Oleksyn, L. Lebioda, and M. Ciechanowicz-Rutkowska, Acta Cryst. B 35, 440 (1979); B. J. Oleksyn, Acta Cryst. B 38, 1832 (1982).

[31] P. Butz, R. T. Kroemer, N. A. Macleod, and J. P. Simons, Physical Chemistry Chemical Physics 4 (15), 3566 (2002); R. C. Dunbar, J. D. Steill, and J. Oomens, International Journal of Mass Spectrometry 297 (1-3), 107 (2010).

CHAPTER III

Electronic and vibrational spectroscopy of Hydroquinine and Hydroquinidine - Comparison with Quinine and Quinidine

INDEX

List of figures

List of Tables

I. INTRODUCTION

Soon after the discovery of Quinine as a preventive drug against malaria, there was an increase in demand of alternative drugs with better antimalarial efficacy compared to Quinine, Chloroquine being an example.

However, within the next two decades, the strain of *Plasmodium falciperum* modified itself to become Chloroquine-resistant. This led to Quinine becoming the only drug available to the masses for the treatment of Chloroquine-resistant malaria. Unfortunately, with the protozoan-parasite becoming even resistant to Quinine, there was an urgent demand for an alternative to Quinine. A study done by Smith & Edstein[1] discovered that when Hydroquinine is added in small proportions (10% by weight) to commercially available intravenous Quinine, it results in a recovery of the antimalarial activity for Quinine-resistant malaria. Although the proportion of Hydroquinine in plasma is 10% to that of Quinine, their binding efficiencies are same. In-vitro experiments showed that there is no interaction between the two molecules when introduced together. In fact, as studied by White et al,[2] Hydroquinine shows a significant contribution to the antimalarial activity only after Quinine has been administered. This clearly indicates that the structural differences between the two molecules, even if minor, differentiate their biological activities.

The three pairs of naturally occurring cinchona alkaloids are shown in Figure 1. They being structurally similar, show very close chemical and biological activities. Hydroquinine and Hydroquinidine denoted by HQn and HQd in the figure 1 differ from Quinine (Qn) and Quindine (Qd) by the presence of an ethyl group instead of a vinyl group in the Quinuclidine part of each molecule. The configurations of chiral centres for Qn, HQn and Cinchonidine (Cd) are C_8(R), C_9(S) while it is just the reverse, C_8(S), C_9(R) for Qd, HQd and Cinchonine (Cn). However, as one probes into their fundamental physico-chemical properties, differences come into forefront.

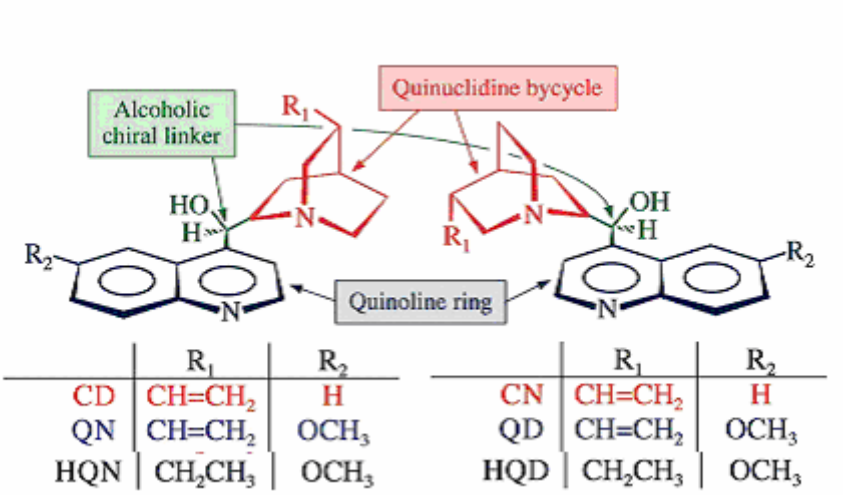

	R_1	R_2
CD	$CH=CH_2$	H
QN	$CH=CH_2$	OCH_3
HQN	CH_2CH_3	OCH_3

	R_1	R_2
CN	$CH=CH_2$	H
QD	$CH=CH_2$	OCH_3
HQD	CH_2CH_3	OCH_3

Figure 1: *The six important naturally occurring cinchona alkaloids with their three principal functional moieties (Quinoline ring, Quinuclidine group and alcoholic chiral linker) highlighted.*[3]

As pointed out by Zaera et al,[3] this reversal in chirality at the linker atoms (C_8 and C_9 as shown in Figure 2), keeping fixed the configurations of the other three chiral centres (N_1, C_3, C_4) on the molecule, causes a difference in the orientation of the vinyl group. According to them, this structural difference gives rise to energetic and entropic changes in the molecule which manifest themselves as variation in physico-chemical properties.

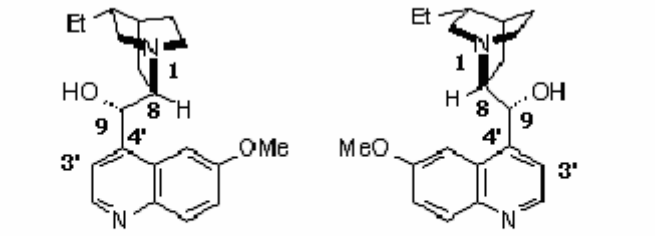

Figure 2: *Structure of Hydroquinine and Hydroquinidine showing the chiral centres in the two molecules.*

The group of Zaera et al explored the above mentioned differences by performing a crystallographic study of the structure of solid cinchona alkaloids. According to them, the formation energy of the crystal is larger in

the case of Cinchonine than Cinchonidine. In fact, it is the difference in the position of the vinyl group in Cinchonine which improves its packing ability compared to its pseudo-enantiomer.

Next, they complemented the above results with experiments done in solution, where they found that:

- All cinchona alkaloids having the chirality of Cinchonidine (for example Quinine, Hydroquinine) are more soluble than those with opposite chirality at the linker atoms.
- Saturation of the vinyl group leads to a decrease in solubility. This observation is valid irrespective to the nature of solvent.

Quantum mechanics calculations support these trends in energetics among cinchona alkaloids in solution. These calculations also point out that differences in energetics in solution, if any, are observed only in case of high-energy conformations in which the vinyl group is close to the Quinoline ring (closed form). As experiments in solution are done at room temperature, in order to explain properly the differences in solubility of cinchona alkaloids, calculations of enthalpy terms are insufficient and changes in entropy have to be considered too. Finally, they conclude that it is the change in the position of vinyl group which dictates a change in the properties ultimately leading to variation in the entropy of dissolution.

As the density of states brought by a non-saturated chain is larger than that brought by the vinyl substituent, the difference between the entropy contribution between the two pseudo-enantiomers is expected to be more prominent for the Hydroquinine/Hydroquinidine pair than it is for the Quinine/Quinidine pair. Thus in this chapter, we try to find out whether in gas phase too, we observe a similar change in the properties for Hydroquinine and Hydroquinidine. In order to do so, we perform a combined electronic and vibrational spectroscopic study of the two molecules and try to find out whether:

- Hydroquinine and Hydroquinidine act as pseudoenantiomers with different properties as observed in crystallographic studies.
- Compared to Quinine and Quinidine, their conformers, if any, show similar or different vibronic absorption.

- Also, temperature-dependent NMR and CD spectroscopic studies, combined with molecular mechanics calculations done on Hydroquinidine in solution, show the existence of two conformations.[4] According to them, two conformers of Hydroquinidine, anti-open (80-90%) and syn-closed (10-20%) exist in solution. We want to find out whether the same population of conformers is observed in gas phase too.

II. RESULTS OBTAINED FROM CALCULATIONS

Calculations of the electronic ground state of Hydroquinine and Hydroquinidine have been done at the same level as Quinine and Quinidine (b3lyp/6-31+G(d,p)) with the Gaussian 09 suite of programs.[5] The results gave two most stable structures for each molecule in gas phase, which are as shown in Figure 3.

The details of the nomenclature and configurations of atoms have already been discussed in the earlier chapter. The two structures of Hydroquinine shown in Figure 3 have a great deal of structural similarity to the most stable isomer of Quinine in gas phase (cis-γ-open(3)). For instance, both the molecules are stabilised by the cis position of the OMe group and the lone pair of Quinuclidine N away from the Quinoline ring (open conformation). The configuration of atoms around the chiral linker is exactly the same for Hydroquinine and Quinine (8R,9S) and that of Hydroquinidine and Quinidine (8S,9R). In contrast to Quinine, there are two conformers of similar energy for Hydroquinine (ΔG =0.16 kcal/mol at room temperature). These two conformers differ by the orientation of the peripheral ethyl group. The CH_2-CH_3 unit is pointed towards the plane of the Quinoline ring in case of cis-γ-open(3a) while it is directed away for the cis-γ-open(3b) isomer. The same observation is true for the cis-γ-open(3a) and cis-γ-open(3b) isomers of Hydroquinidine. Among the two, cis-γ-open(3a) and cis-γ-open(3b) are the most stable conformers of Hydroquinine and Hydroquinidine respectively.

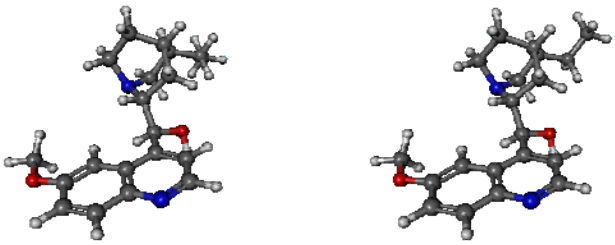

HQd-cis-γ-open(3a) HQd-cis-γ-open(3b)

ΔG =0.02 kcal/mol

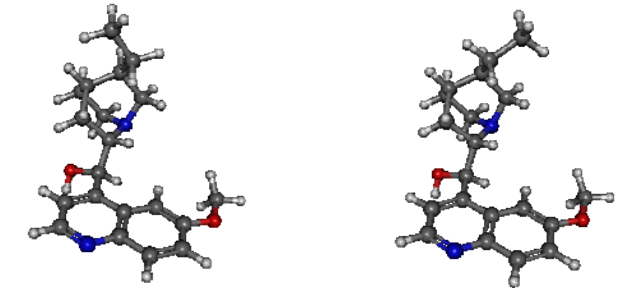

HQn-cis-γ-open(3a) HQn-cis-γ-open(3b)

ΔG =0.16 kcal/mol

Figure 3: *The most stable structures of Hydroquinidine (top) and Hydroquinine (below).*

The important dihedral angles and Boltzmann populations of conformers whose ΔG values are lesser than 1.6 kcal/mol at room temperature have been tabulated below.

From the table it can be concluded that the two pseudo enantiomers behave the same in terms of lower-energy conformers; they both show two quasi iso-energetic conformers of identical structure. In Hydroquinidine apart from the two iso-energetic conformers there are no higher energy conformers with $\Delta G \leq 1.5 \text{kcal/mol}$. In contrast, there are four higher energy conformers in case of Hydroquinidine among which three are of "closed" type with the important dihedral angles differing a lot from its stable counterpart. It is therefore expected that experiments at room temperature will show more differences between Hydroquinine and Hydroquinidine than they do between Quinine and Quinidine.

Molecule	Conformers	ΔG (kcal/ mol)	Population at 298.15 K (%)	τ_1	τ_2	τ_3	T_3
HYDROQUININE	cis-γ-open(3a)	0	54.6	99	154	-82	173
	cis-γ-open(3b)	0.16	41.6	99	152	-84	173
	cis-β-closed(7b)	1.57	3.8	13	55	-179	-82
			100				
HYDROQUINIDINE	cis-γ-open(3b)	0	37.7	-99	-154	82	-173
	cis-γ-open(3a)	0.02	36.5	-98	-153	83	-174
	cis-γ-closed(1b)	1.15	5.4	111	-53	-179	173
	cis-γ-closed(1a)	1.17	5.3	107	-57	178	179
	cis-α-closed(2b)	1.39	3.6	-12	158	176	82
	trans-γ-open(3b)	1.50	3.0	-100	-157	79	-170
	trans-γ-open(3a)	1.51	2.9	-100	-157	79	-170
	cis-α-closed(2a)	1.52	2.9	-11	-58	176	82
	cis-γ-closed(2b)	1.54	2.8	-73	-61	178	175
			100				

Table 1: *A list of the important dihedral angles, the ΔG values and the Boltzmann populations of the most stable conformers of Hydroquinine and Hydroquinidine.*

II.1. Calculated Spectra

The calculated frequencies have been plotted in the range of ν(OH) and ν(CH) stretch modes for the two stable conformers of Hydroquinine and Hydroquinidine (Figure 4). The vibrational spectrum has been simulated by calculating the harmonic frequencies at the same level of theory and convoluting the frequencies by a Lorentzian line shape of 3 cm^{-1} FWHM. No scaling factors have been introduced.

On comparing the calculated spectra of the two stable conformers of Hydroquinine and Hydroquinidine (Figure 4), one can find out that there are more differences between the spectra of the most stable conformers of Hydroquinine and Hydroquinidine than between the two most stable

conformers of a given molecule. Indeed, conformers cis-γ-open(3a) and cis-γ-open(3b) of the same pseudo-enantiomer exhibit only minor differences in the spectra shown in Figure 4. We shall therefore focus on the comparison between Hydroquinine and Hydroquinidine in the following sections.

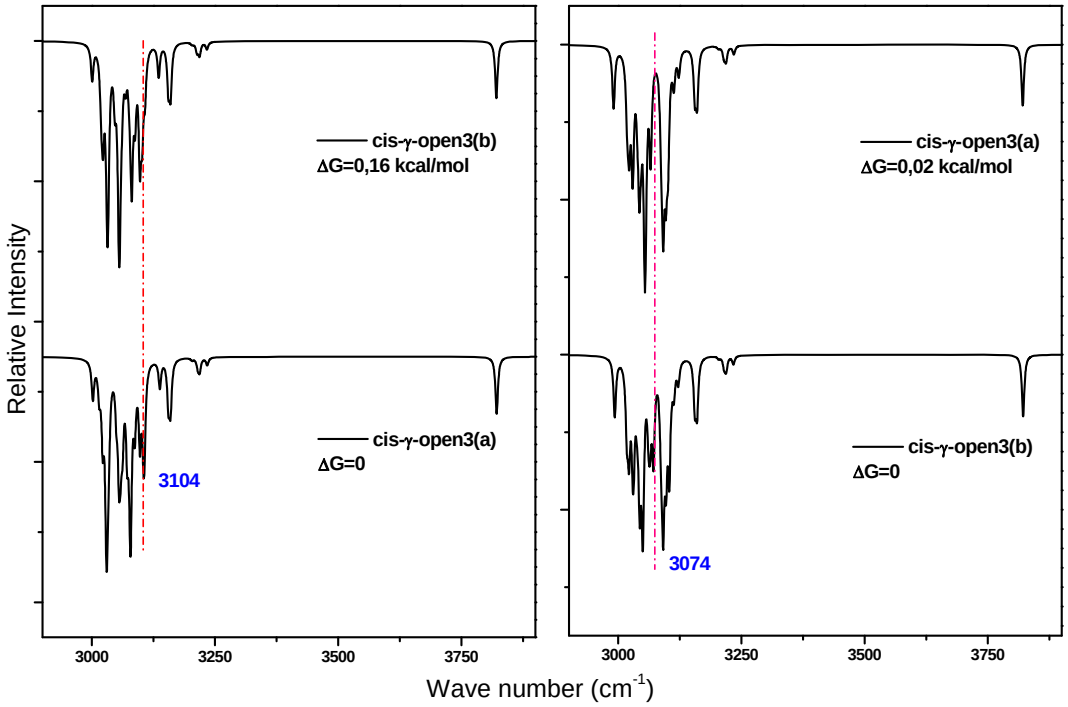

Figure 4: *Calculated spectra of the cis-γ-open-(3a) and cis-γ-open-(3b) conformers of Hydroquinine and Hydroquinidine. No scaling factors have been introduced.*

Since the experiments have been done only in the infrared range 2900-3700 cm^{-1}, the simulated plots have been illustrated only in the mentioned range. However, the frequencies corresponding to the low and middle frequency regions have been tabulated in the table 2.

II.2. The comparison between the most stable conformers of Hydroquinine and Hydroquinidine

From the plots shown in Figure 4 and the frequencies tabulated in the table 2, the vibrational transitions occurring in the two molecules can be categorized in the following three wavelength regions:

HYDROQUININE			HYDROQUINIDINE			ASSIGNMENT
EXPERIMENTAL (cm^{-1})		CALCULATED (cm^{-1})	EXPERIMENTAL (cm^{-1})		CALCULATED (cm^{-1})	
S_o	S_1		S_o	S_1		
		9			20	Torsion of the sub-units.
		26		25	25	Wagging of the sub-units.
		82			97	Wagging of the ethyl chain.
		160			179	Deformation in Quinuclidine.
		323			317	Bending of OH.
474	463	476	531	467	548	$8b_{1g}$
795	748	772	811	750	772	$8a_{1g}$
1326		1468	1413		1418	$5a_{1g}$ coupled with methoxy umbrella motion.
		1414,1424			1415,1428	CH bend localized on the chiral linker.
		1631			1632	$C_{3'}$-$C_{4'}$ stretch and $C_{4'}$H in plane bend.
2873		3002	2874		2992	Asymmetric CH stretch near the Quinuclidine N.
2893		3014	2894		3017	Symmetric CH stretch modes localised in the Ethyl group.
2915		3035	2924		3037	C_9H stretch in the chiral linker.
2921		3049	2927		3049	Symmetric CH stretch modes in Quinuclidine.
2959		3087	2962		3086	Asymmetric CH stretch of OMe .
2940		3062	2956		3063	Symmetric CH stretch modes in Quinuclidine localized on the C_8 atom.
2981		3106	2979		3103	Symmetric CH_3 stretch on Et.
3005		3137	2987		3121	Symmetric CH stretch modes in Quinuclidine close to N.
3050		3159	3050		3159	Aromatic CH stretch.
3091		3218	3090		3218	Aromatic CH stretch.
3651		3821	3651		3821	OH stretch.

Table 2*: List of frequencies obtained experimentally and calculated for the cis-γ-open(3a) and cis-γ-open(3b) conformers of Hydroquinine and Hydroquinidine respectively along with their assignments.*

II.2.1. Low-frequency region (< 200 cm-1)

This region mainly consists of out-of-plane rocking vibrations of the two bulky units along the important dihedral angles τ_1, τ_2, τ_3 and T_3. For

instance, the vibration at 9 cm^{-1} for Hydroquinine and 20 cm^{-1} for Hydroquinidine corresponds to torsion of both the bulky units. The vibrations with frequencies of 82 and 97 cm^{-1} for Hydroquinine and Hydroquinidine respectively correspond to a wagging motion of the ethyl chain. Again, a deformation localised on the Quinuclidine unit is observed at 160 and 179 cm^{-1} for Hydroquinine and Hydroquinidine respectively. This deformation also involves slightly the ethyl group of the Quinuclidine unit. Among the frequencies in the low-frequency region (< 200 cm^{-1}), only the above three differ by more than 10 cm^{-1} between the two pseudo enantiomers. The others with smaller differences (<10 cm^{-1}) are mainly due to relative torsion of the two bulky units.

II.2.2. Middle-frequency region (200-2800 cm-1)

The frequencies lying in the region mostly correspond to out-of-plane twisting and bending of the two molecules. An out of the COH plane bending vibration of the OH group attached to the chiral linker is observed at 317 and 323 cm^{-1}. The vibration at 1631 cm^{-1} (Hydroquinine) and 1632 cm^{-1} (Hydroquinidine) is mostly localised on the aromatic $C_{3'}$-$C_{4'}$ stretch coupled with the $C_{4'}H$ in plane bend. The two CH bending vibrations localized on the chiral linker are also calculated at 1414/1424 and 1415/1428 cm^{-1} for Hydroquinine and Hydroquinidine, respectively. At 1418 cm^{-1}, there exists an umbrella motion of a Methyl group in the Ethyl chain for both the molecules.

II.2.3. High-frequency region (> 2800 cm-1)

This region can be further divided into two sub-categories:

- The ν(OH) region: An intense absorption corresponding to the OH stretch mode has been calculated in both the molecules at 3821 cm^{-1}.
- The ν(CH) region: Both the molecules show a dense spectrum due to numerous C-H stretch modes in this particular range (2900-3200 cm^{-1}). The calculated frequencies between 3000-3160 cm^{-1} are mostly comprised of symmetric and asymmetric aliphatic CH stretch modes localized on the Quinuclidine unit and the linker carbon atoms. The lower frequency modes

include aromatic CH stretch modes (> 3160 cm^{-1}) localized on the Quinoline ring. The vibrations with frequencies in between 3160 and 3240 cm^{-1} are due to aromatic CH stretch modes and appear at the same frequencies for both the pseudoenantiomers. This is not surprising because these vibrations are far away from the chiral centres. It is also observed that all the modes localized on the methoxy-substituted Quinoline have identical frequencies and oscillator strengths with increasing frequencies both for the aromatic ν(CH) stretches and ν(OH) stretch.

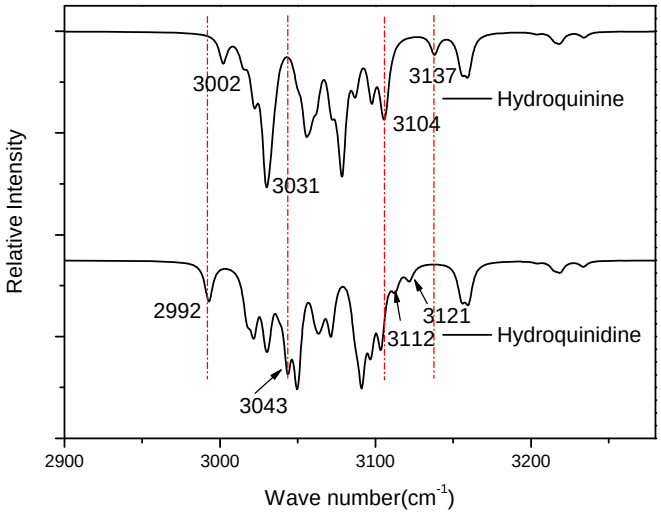

Figure 5: *Plot showing the ν(CH) region (2800-3300 cm^{-1}) of the most stable conformers of Hydroquinine and Hydroquinidine.*

Since the two pseudo enantiomers differ in the configuration of atoms around the chiral center, it is expected that the vibrations of atoms constituting the chiral linker might differ. However, the C_9H stretch appears at the same frequencies 3035 cm^{-1} (Hydroquinine) and 3037 cm^{-1} (Hydroquinidine). The differences arise only in the ethyl substituted Quinuclidine ring. In the Figure 5, the frequencies 3137 and 3121 cm^{-1} for Hydroquinine and Hydroquinidine respectively, are both due to an asymmetric CH stretch vibration localized on the CH_2 (C_2 atom of quinuclidine) unit adjacent to the alkaloid nitrogen. The bands at 3104 and 3112 cm^{-1} are due to an asymmetric CH stretch vibration involving the CH_2 unit of the Quinuclidine ring adjacent to the C_8 atom of the chiral linker. The frequencies 2992, 3043 cm^{-1} (Hydroquinidine) and 3002, 3031 cm^{-1}

(Hydroquinine) are due to vibrations involving most of the CH stretch modes in the Quinuclidine unit. It is interesting to note that only the CH stretches localized on Quinuclidine are different between the two pseudo-enantiomers. All the notable frequencies in the ν(CH) range have been mentioned in the table 2.

III. EXPERIMENTAL RESULTS

Spectroscopic studies on Hydroquinine and Hydroquinidine have been performed following the same methodology as given in the earlier chapter. For electronic spectroscopy, we have limited ourselves to laser-induced fluorescence as our experience on Quinine and Quinidine showed that identical results are obtained in LIF and REMPI. The electronic ground state and first excited state of the two molecules have been studied with the help of laser-induced fluorescence excitation and emission. Next in order to get structural information of the electronic ground state, IR-UV double resonance experiments have been performed. It must be noted that all the experiments have been recorded in identical conditions, and Ne has been used as a carrier gas to decrease the presence of hot species in the supersonic jet.

III.1. UV excitation spectra

Hydroquinine and Hydroquinidine share the same Quinoline chromophore attached to a bulky Quinuclidine ring as Quinine, and hence are expected to show similar absorption typical of a ππ* transition in the same frequency range. Laser-induced fluorescence excitation spectra of Hydroquinidine and Hydroquinine recorded in the region 29850-32000 cm^{-1} (Figure 6), confirm that indeed it is true. No L_a transition is observed at higher frequencies, as expected for molecules whose lifetime becomes shorter with increase in excitation energy.

In each case, the most intense band has been assigned to the transition origin. However, the assignment of the electronic band origin for

both the molecules is complicated by the presence of several bands of similar intensity and will be discussed later in detail. It is to be noted that Hydroquinidine being very sensitive to ablation generally gives a noisier UV signal.

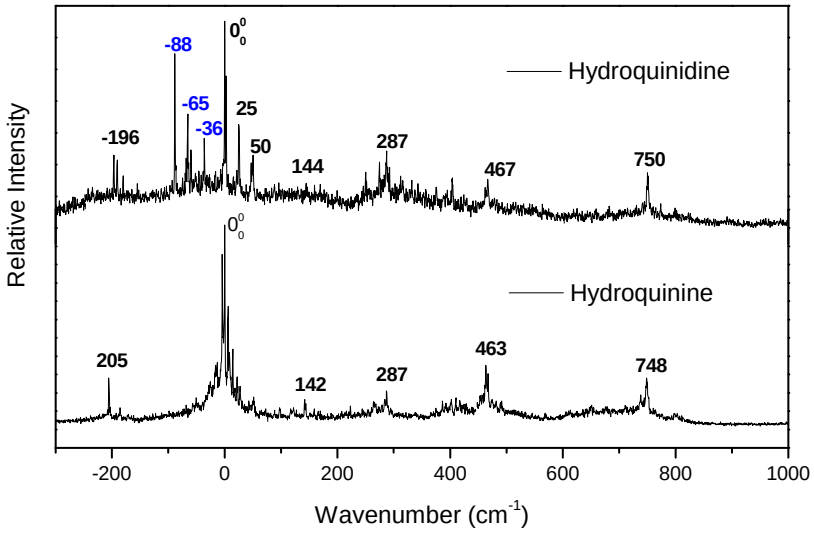

Figure 6: *LIF excitation spectra of Hydroquinidine and Hydroquinine. The origin transition of each molecule has been taken as their respective scale origin. The bands shown in blue are the points of difference between the two molecules.*

III.1.1. High-frequency region

The higher-energy bands which are to the blue of the origin transition at 748 cm^{-1} and 750 cm^{-1} in Hydroquinine and Hydroquinidine, respectively, as observed in Figure 6 are also observed in the electronic spectrum of Quinine. They have been assigned to the $8a_{1g}$ vibration mode. Similarly the bands at 463 and 467 cm^{-1} for Hydroquinine and Hydroquinidine respectively, have been assigned to the $8b_{1g}$ vibrational mode of the Naphthalene ring. Additionally, the 144, 287 cm^{-1} bands are common to the two molecules. The former corresponds to a bending motion of the Methoxy substituent while the latter corresponds to a rocking motion of the CH_2-CH_3 substituent coupled with deformation of the Quinuclidine frame as already seen in Quinine.

III.1.2. Low-frequency region

From the transitions which are similar for both the molecules, special mention has to be made about the one which is much to the red (-196, -205 cm^{-1}) of the electronic origin of both the molecules. Just like Quinine, these low-energy bands seem to vary in intensity with changes in the cooling conditions of the jet and can be assumed to be hot bands.

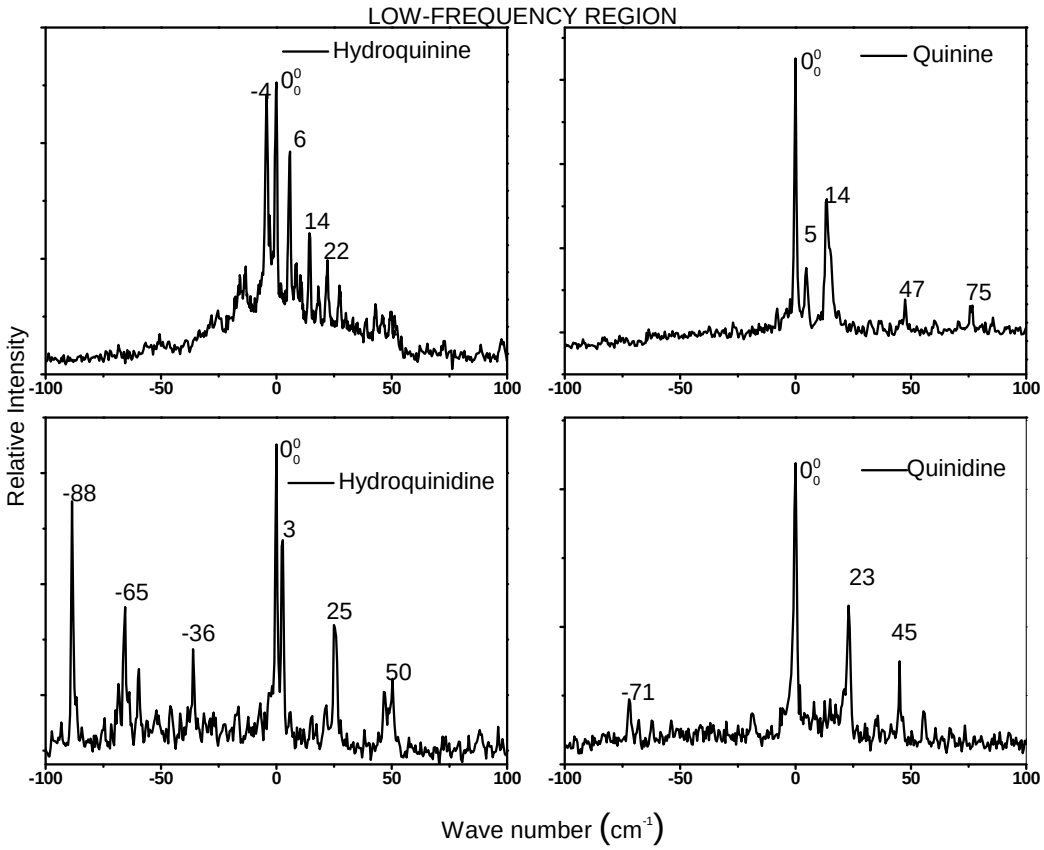

Figure 7: *Fluorescence excitation spectrum of Hydroquinine, Hydroquinidine, Quinine and Quinidine in the low-frequency region. The origin transition of each molecule has been taken as their respective scale origin.*

The 0-0 ± 100 cm^{-1} part of the low-frequency region is particularly interesting as the two molecules absorb at distinctly different frequencies. The Figure 7 shown below gives a closer view of the low frequency region at ±100 cm^{-1} to the supposed band origin. Additionally spectra of Quinine and Quinidine have been shown to highlight the differences between the four molecules.

In the case of Hydroquinine there is a congestion of bands close to the band origin (± 100 cm^{-1}). In particular, there are two bands, the supposed origin and that at -4 cm^{-1}, which are almost equal in intensity. From now on, the bands at -4, 0-0, +6, +14 and +22 cm^{-1} will be termed as A, B, C, D and E. The spacing between the A, B, C, D, E bands is below 10 cm^{-1} and is not regular, which prevents their assignment to a vibrational progression. This irregularity in the bands close to the origin has already been observed in Quinine (0-0, +5, +14 and +47 cm^{-1}).

Unlike Hydroquinine, Hydroquinidine does not show any spectral congestion near the supposed $S_0 \rightarrow S_1$ transition origin. Instead, Hydroquinidine stands out with an intense absorption at 88 cm^{-1} to the red in addition to the supposed band origin. While the expected band origin is followed by two bands at +25 and +50 cm^{-1} which look like a vibrational progression built on a low-frequency mode of 25 cm^{-1}, the absorption at -88 cm^{-1} is followed by two other small bands at -65 and -36 cm^{-1}. These three bands to the red also seem to form a vibrational progression built on a similar low-frequency mode as is observed in case of the supposed band origin. There is also a band at +3 cm^{-1} to the supposed electronic origin which is almost as intense as the 0-0 and the -88 cm^{-1} band.

III.1.3. Determination of the transition origin

Before probing into the reason behind the differences observed in the excitation spectrum of the two molecules, it is very important to know for sure the correct position of their transition origins. Hence the next section has been devoted to ascertain the true electronic band origin of the two molecules.

HYDROQUININE

In order to verify whether a correct assignment of the electronic origin has been done for Hydroquinine, the following experiments have been performed. In these experiments the dependence between the relative intensities of bands A and B on the delay between excitation and ablation lasers has been studied. Each experiment has been performed in the

presence of two different cooling conditions, one with Ne as the carrier gas and the other with Ar.

Ne as carrier gas

The initial spectrum has been recorded by keeping the delay between the pair of lasers (excitation and ablation) at a value of 21.6 µs at which both the bands (A and B) are almost equal in intensity. This delay corresponds to a distance of 1.69 cm between the nozzle and the excitation laser. Next the delay is changed on either side of this value till the point is reached when the ratio between the two peaks is changed. For example, when the delay is moved to 21.8 µs, A is more intense than B and when it is at 20.5 µs, the reverse occurs. If the delay is shifted higher than 21.8 µs, the band A is still

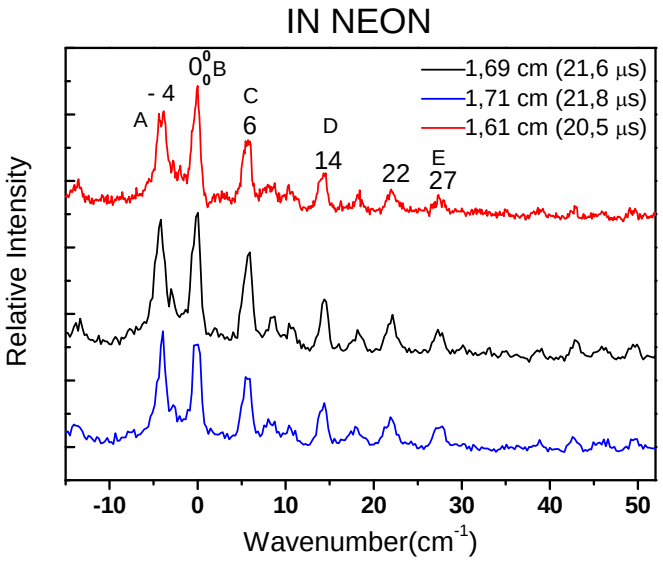

Figure 8: *Comparative study of excitation band intensities in the low frequency region with change in delay between excitation and ablation lasers in presence of Ne.*

more intense than B. Similarly, B remains more intense than A when the delay is lesser than 20.5 µs. Now, since the change in the delay is actually an image of the distance between the ablation plume and the excitation laser, the band B is more intense than A at a distance shorter than 1.61 cm, and the intensity is reversed when the jet is kept at distance larger than 1.71 cm. Thus it can be supposed as we did in the previous chapter that the shorter is the distance and lower the delay, higher is the chance of the lasers

to interact with better cooled molecules. Following the hypothesis, the red curve of Figure 8 is an image of a cooler jet than the blue. If that is true, then in a cold jet, the band at 30646 cm^{-1} (band B) is clearly the band origin. Also, it is to be noted that the ratio between the band B and the other bands of weaker intensities is almost similar in all the three plots. This proves that the band at 30642 cm^{-1} (band A) is more sensitive to the temperature of the jet and thus can be arising from a hot species.

Argon as carrier gas

Argon, when used as a carrier gas, tends to give more bands and background in the excitation spectrum compared to neon. From the plot below it is observed once again that at shorter delays between the two lasers (that is, shorter distance between the jet and lasers), the band at 30646 cm^{-1} (band B) is the most intense among all the bands and can be termed as the electronic band origin. The other one (band A) is either a hot band or the transition origin of another conformer.

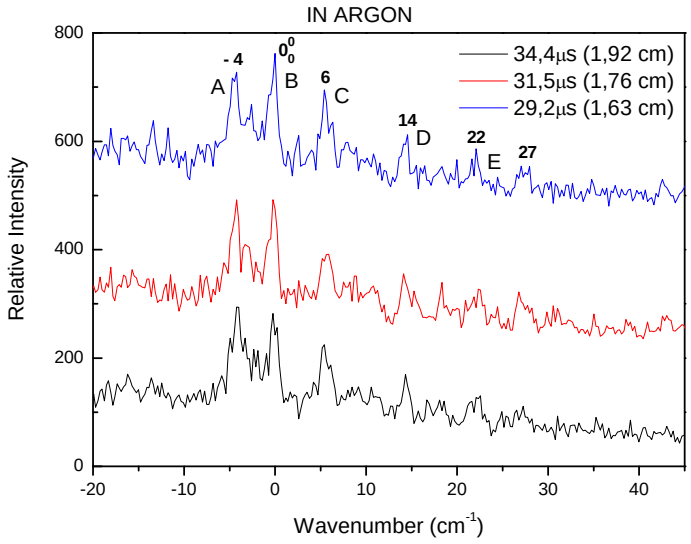

Figure 9: *Comparative study of excitation band intensities in the low frequency region with change in delay between excitation and ablation lasers in presence of Ar.*

HYDROQUINIDINE

From the plot (Figure 7) of Hydroquinidine it is clearly observed that the band at 88 cm^{-1} to the red is almost equal in intensity to the supposedly

band origin (30647 cm^{-1}). However, the former is not considered as the band origin. This is because it is an isolated band with no counterpart in the blue at the characteristic wavelengths of 468 cm^{-1} or 750 cm^{-1}. These frequencies being characteristic to the $8b_{1g}$ and $8a_{1g}$ vibronic modes of naphthalene are bound to exist for structurally similar cinchona alkaloid molecules.

As mentioned earlier, there exists another band at +3 cm^{-1} which does not follow any vibrational progression but almost as intense as the bands at 0-0 and -88 cm^{-1}. The relative intensities of the 0-0 and +3 cm^{-1} bands have been studied with change in the distance between the ablation plume and excitation laser, following the same method as has been done in Hydroquinine. The inert gas used is Ne. As given in the Figure 10, shorter the distance and greater is the interaction between the laser with cold molecules, lesser is the intensity of +3 cm^{-1} band compared to the band origin. This leads us to assume that the band at +3 cm^{-1} might be a hot band. One cannot entirely rule out the possibility of it being another conformer, this will be verified later with IR-UV double resonance spectroscopy.

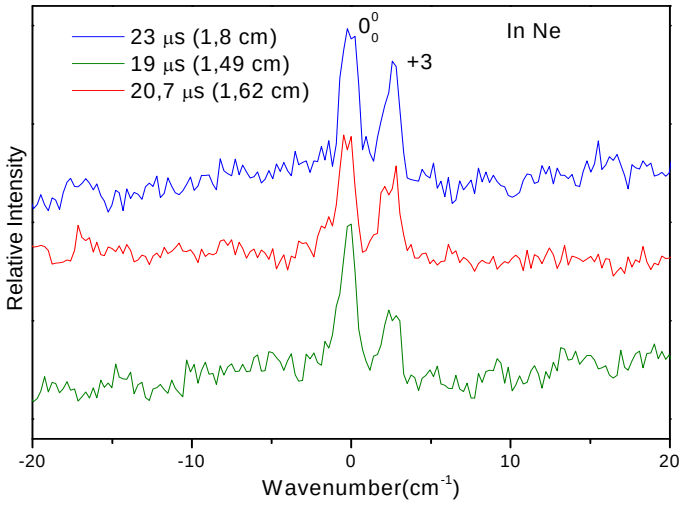

Figure 10*: Comparative study of excitation band intensities in the low frequency region with change in delay between excitation and ablation lasers in presence of Ne.*

The origin transition frequencies of each molecule have been given in the table 3.

Origin transition frequencies (cm^{-1})	QUININE	QUINIDINE	HYDROQUININE	HYDROQUINIDINE
	30621	30641	30646	30647

Table 3 *List of the electronic origin transitions of all the four cinchona alkaloids.*

III.2. UV emission spectra

The fluorescence emission spectrum resulting from the excitation of the transition origin of the two pseudo-enantiomers is given in Figure 11. Both the molecules emit at the prominent $5a_g$ transition localised on the Naphthalene ring. Apart from that, the bands at 795 cm^{-1} and 474 cm^{-1} represent the $8a_{1g}$ and $8b_{1g}$ modes of Naphthalene respectively in case of Hydroquinine.

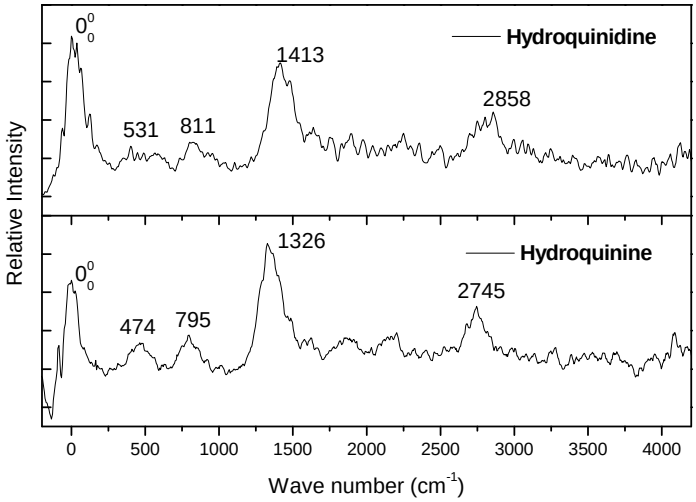

Figure 11: *Laser induced dispersed emission spectrum of Hydroquinine and Hydroquinidine. Scattered light has been subtracted in each plot.*

The bands at 2858 cm^{-1} and 2745 cm^{-1} for Hydroquinidine and Hydroquinine respectively are clearly observed in the emission spectrum. In case of Quinine and Quinidine this particular transition is very weak and has been assigned to 2 quanta of the $5a_{1g}$ mode vibration of naphthalene.

From the above spectrum, this assignment stands valid for Hydroquinine and Hydroquinidine too.

Emission spectra of bands A and B of Hydroquinine have been recorded. Doing so, an intense emission is observed in the 1300-1400 cm^{-1} range for both (1391cm^{-1} for the band A and 1326 cm^{-1} for the band B respectively). It is also interesting to observe a relatively more intense emission at 2745 cm^{-1} for band A compared to that at 2733 cm^{-1} for band B.

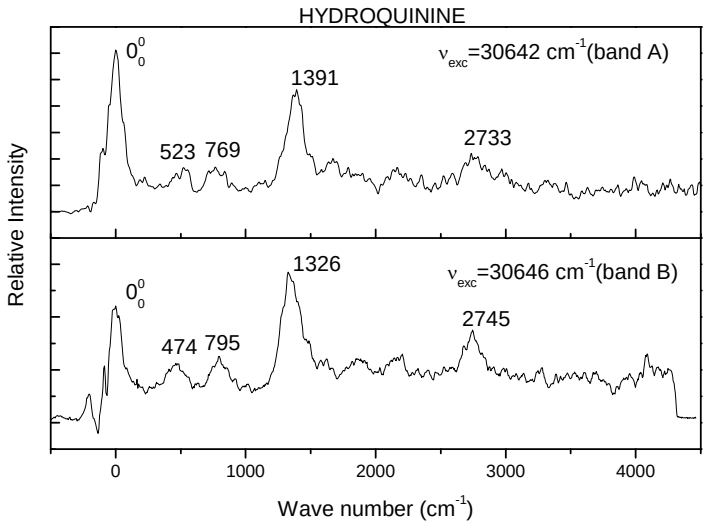

Figure 12: *High-resolution dispersed fluorescence of Hydroquinine with excitation laser kept at bands A and B.*

The differences observed in the excitation spectrum of Hydroquinine cannot be observed in the fluorescence emission spectrum. Indeed, we don't have the resolution for distinguishing origin transitions separated by a few cm^{-1}.

III.3. Vibrational Spectroscopy In Gas Phase: IR-UV Double Resonance

The calculations done on the two pseudoenantiomers indicate the presence of two stable conformers for each molecule. Hence an IR-UV double resonance study gives an idea about the nature of the ground state of each such conformer. It also helps to distinguish between bands originating from

hot molecules and actual conformers. The method used for this study is exactly the same as followed with Quinine. First, the IR depletion has been studied for both the molecules keeping the UV fixed at their respective band origins, next a detailed study has been done for UV fixed at different transitions for each molecule. Each time, the infrared laser has been scanned in the ν(CH) (3150-2800 cm^{-1}) and the ν(OH) (3500-3750 cm^{-1}) stretch wavelength region.

III.3.1. Probe set on the band origins

The IR-UV depletion spectra have been recorded with the UV kept fixed at the respective band origins of Hydroquinine and Hydroquinidine located at 30646 cm^{-1} and 30648 cm^{-1} respectively.

The figures Figure 13 and Figure 14 depicts the IR-UV depletion spectrum of the two molecules in the ν(OH) and ν(CH) stretch regions. As observed in Figure 13, both the molecules absorb at a single wavelength (3651 cm^{-1}) in the OH stretch region similar to Quinine and its pseudoenantiomer.

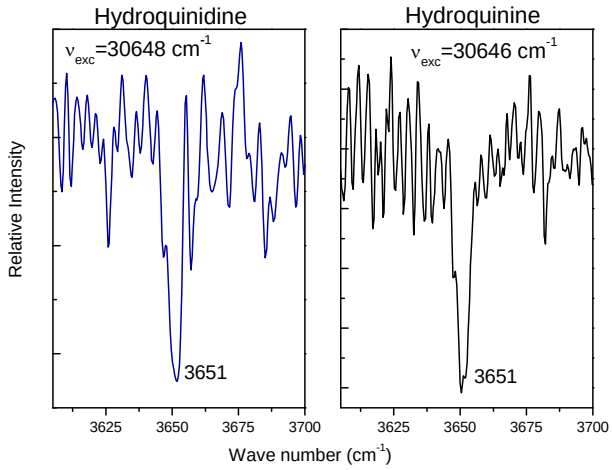

Figure 13*: IR-UV depletion spectrum of Hydroquinine and Hydroquinidine in the ν(OH) stretch region (3500-3750 cm^{-1}).*

The ν(CH) stretch region is typically congested as is expected for molecules with above 20 aliphatic and aromatic C atoms. The typical CH stretch mode frequencies which are observed in the two molecules are given in the Figure 14.

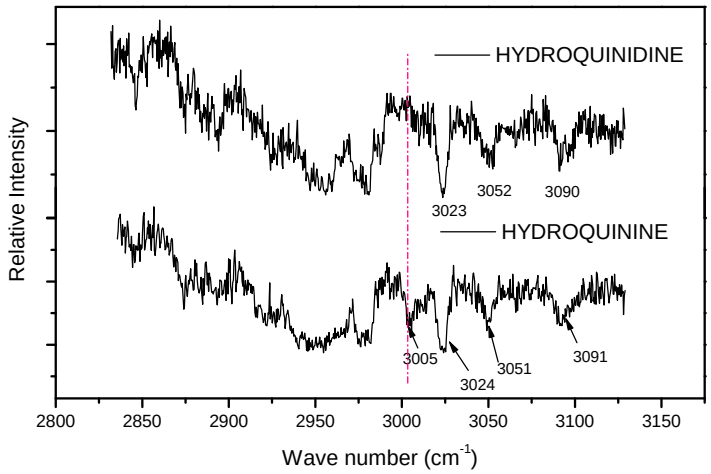

Figure 14: *IR-UV depletion spectra of Hydroquinidine and Hydroquinine probed at their respective electronic origin. The IR laser has been scanned in the ν(CH) region. The wavenumber shown by a red dashed line is a unique transition of Hydroquinine.*

From the Figure 14, it can be said that the two molecules absorb almost identically in the infrared range. This similarity is a contrast to the markedly different electronic absorption (Figure 6) shown by the two molecules. The only point of difference appears at an aliphatic symmetric CH stretching frequency observed at 3005 cm^{-1} in case of Hydroquinine. It is clearly not observed for Hydroquinidine in the given spectrum. Comparison with calculated frequencies says the same. In fact the calculated frequency at 3121 cm^{-1} in case of Hydroquinidine, and assigned to the asymmetric CH_2 stretch localised on the C atom of the Quinuclidine ring next to the alkaloid nitrogen, differs from its counterpart calculated at 3137 cm^{-1} for Hydroquinine.

However, there are frequencies like the one at ~3050 cm^{-1} which are equally intense for both the molecules and well supported by calculations as well. This particular frequency is due to an aromatic CH stretch vibration in CH units close to the aromatic N in the Quinoline ring. The detailed assignment of the different vibrational modes in the total infrared region has been tabulated in table 2. The calculated frequencies given in the table have not been multiplied by their scaling coefficients and hence are higher than their corresponding experimental frequencies.

The Figure 15 compares the IR-UV depletion spectrum of both the molecules in the entire studied infrared range (2850-3700 cm^{-1}).

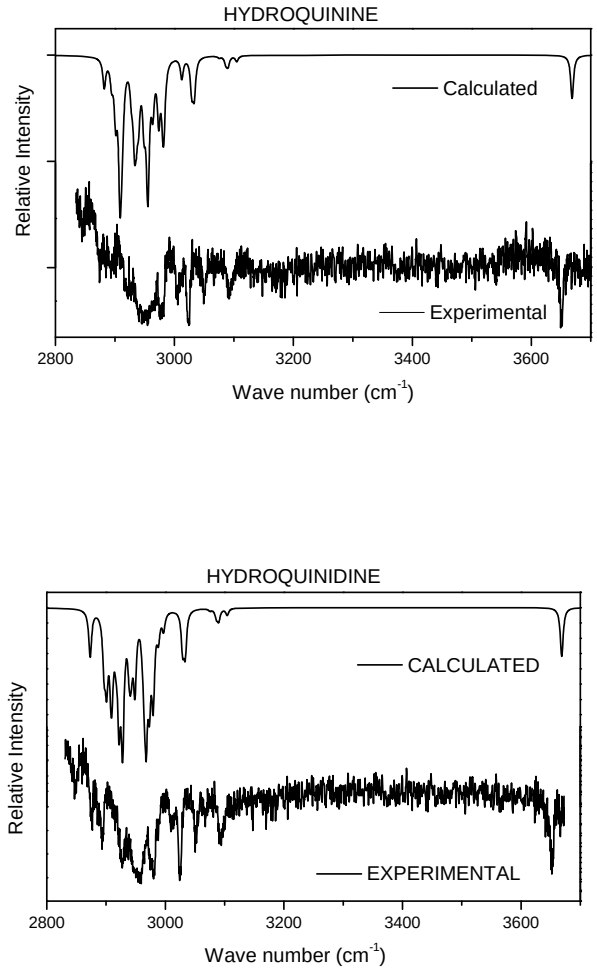

Figure 15: *Comparison between the experimental and calculated spectra in the infrared region (2800-3700 cm^{-1}). The simulated spectra have been multiplied with a scaling coefficient of 0.96.*

The experimental spectra of Hydroquinine and Hydroquinidine are well reproduced by one of the most stable conformers cis-γ-open(3a) or cis-γ-open(3b). However, due to the similarity between the calculated spectra of cis-γ-open(3a) and cis-γ-open(3b) mentioned earlier and the very low calculated energy, it is impossible to give a more precise argument.

III.3.2. Probe set on the bands in the low-frequency region

For both the molecules, the ν(CH) region in the IR-depletion spectrum gives more information than the single absorption observed in the ν(OH) region. So, the ν(CH) region is a key to find out whether the excitation frequencies in the low-frequency region (Figure 7) arise from hot bands or isomers that are different from the one giving rise to the band origin. Thus in the following section we have rapidly mentioned the ν(OH) stretch results and focussed more on the ν(CH) region of each molecule. The latter has been probed with the UV laser fixed individually at all the intense bands in their respective electronic excitation spectrum.

HYDROQUININE

IR-UV double resonance studies on the bands A and B

Since Hydroquinine contains a free OH group along with an abundance of aromatic and aliphatic carbon atoms, it shows depletion in the fluorescence intensities in these two regions. Hence when scanned in and around the free OH region (3500-3750 cm^{-1}), it shows a dip corresponding to the ν(OH) frequency at 3650 cm^{-1}.

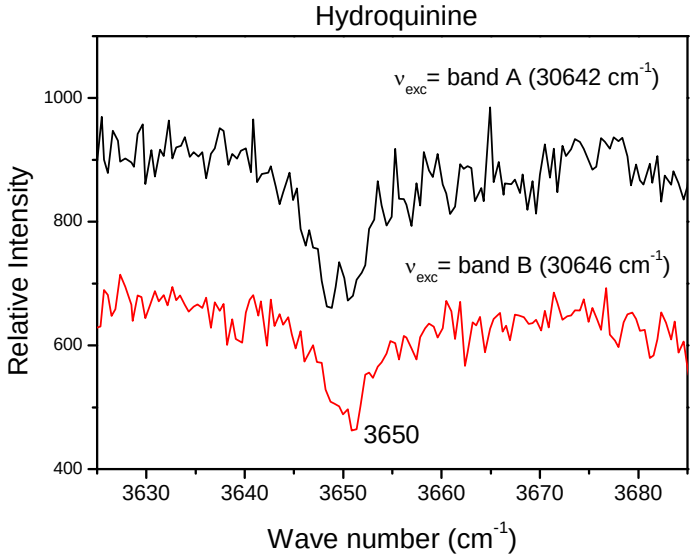

Figure 16: *IR-UV depletion spectrum of Hydroquinine with the probe excitation laser kept at bands A and B.*

There are no differences between bands A and B in this region of the infrared spectrum. Thus the ν(CH) region is probed next and some

interesting results are obtained from it. As shown in the Figure 17 discrepancies in the absorption wavelengths have been observed for the two excitation bands at the IR wavelength region of 3040-2980 cm^{-1}.

The IR-UV depletion plots for the two important bands have been kept diagonally in the Figure 17. It is clear that the band B depletes at 3004 cm^{-1} and not at 2997 cm^{-1}. For the other band A, it is exactly the opposite. While the spectrum obtained keeping the probe at C follows the same trend as band A, the band D is too weak to be probed and assigned unambiguously. Also, at 3024 cm^{-1}, there is depletion for the spectrum obtained keeping the UV probe at all the bands discussed before.

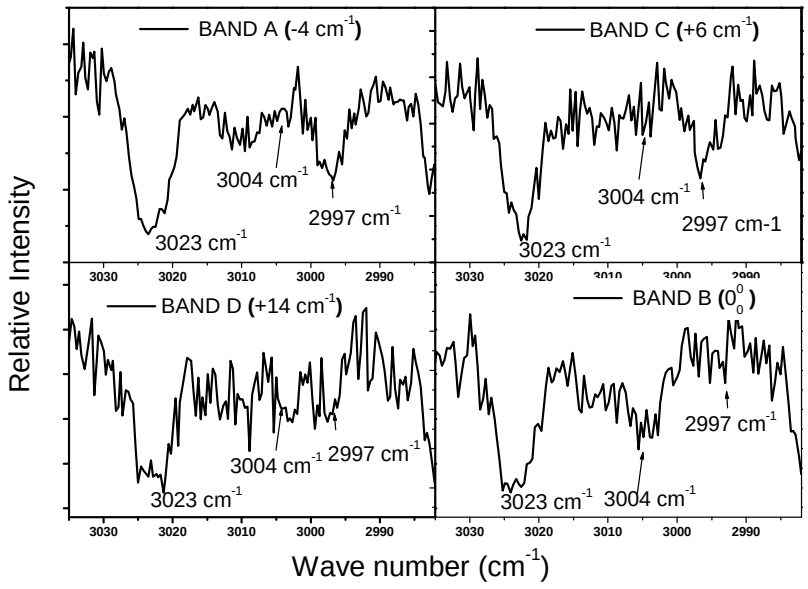

Figure 17*: IR-UV depletion spectra of Hydroquinine, recorded with the excitation laser fixed at bands A, B, C and D.*

The above study has been complemented by a second experiment in which the IR laser has been kept fixed at the wavelengths (2997, 3004 and 3023 cm^{-1}) while the UV laser has been scanned in a small region around bands A and B. The wavelength 3023 cm^{-1} has been chosen because it is absorbed intensely when the UV is kept at the bands A, B, C and D. The band at 2997 cm^{-1} is absorbed by A and C and partly by D. While the one at 3004 cm^{-1} is absorbed by B and partly by D. So, on one hand the wavelength at 3023 cm^{-1} serves as a reference for the maximum depletion observed, on

the other hand the bands at 2997 and 3023 cm^{-1} help to differentiate between bands A and B. Band D is too weak to be probed confidently and we cannot conclude on its nature.

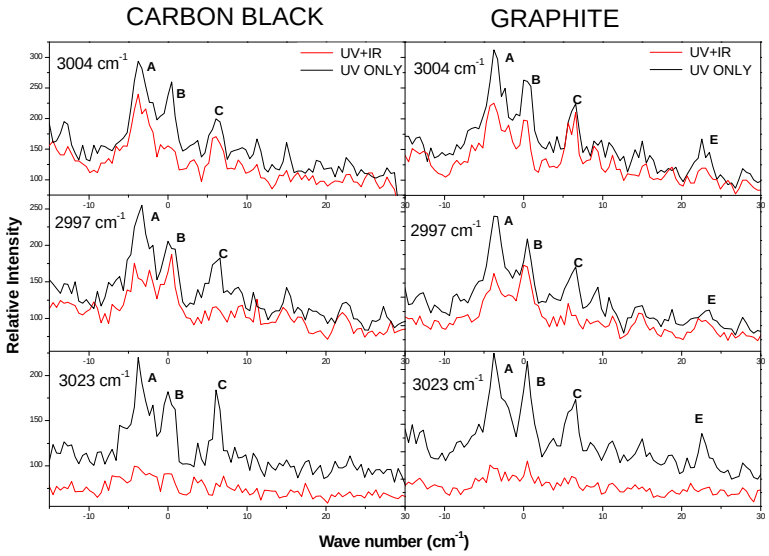

Figure 18*: IR-UV depletion spectrum of Hydroquinine in C black (left) and graphite (right) as matrix for laser ablation. In each case, the IR pump laser has been fixed at 3004 cm^{-1} (top), 2997 cm^{-1} (middle), and 3023 cm^{-1} (bottom) and the UV laser probed around the electronic band origin.*

The scans have been repeated with a C black pellet to re-check the extent of depletion in different cooling conditions of the jet. In the earlier chapter, it has been discussed that when C-black is used as a matrix for laser ablation it results in a cooler jet of ablated molecules. However, since it is more fragile than graphite, it decreases the lifetime of the pellet. That is why a short region, (about 50 cm^{-1} to the blue of the band origin) has been scanned to have an idea of the depletion of cold bands in the low frequency region. In both cases, we have the following observations:

- Both the bands A and B get depleted at IR wavelength 3023 cm^{-1}. It acts as a reference to the extent of depletion in these two bands in case of different IR wavelengths.

- At 3004 cm^{-1}, the bands B and E show more depletion than any other bands in the low-frequency UV range. This might indicate that band E might be a progression of band B. Moreover, we see a weak band at +44 cm^{-1} which can be the second member of this progression (see Figure 8).
- At 2997 cm-1, the bands A and C deplete more than the other bands thereby proving the hypothesis that the band C is indeed from the same conformer as A or at least a conformer showing some IR absorption.
- The band D is missing in all the plots, but it is weak in intensity and so does not allow us to conclude.

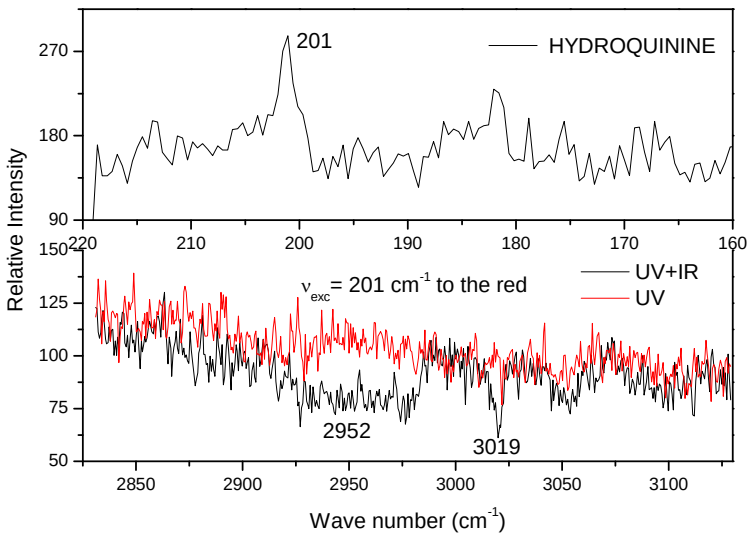

Figure 19*: Top: Fluorescence excitation spectrum of Hydroquinine showing the band at -201 cm^{-1}. Bottom: IR-UV depletion spectrum in the νCH) range with the UV fixed at the band to the red (-201 cm^{-1}).*

Also, it is curious to find out whether the band to the red of the excitation spectrum of Hydroquinine (at -201 cm^{-1}) is from the same conformer which gives rise to the band origin. However, it is to be noted that this excitation band at lower energy is weak in intensity thereby making it difficult to obtain a good depletion in the IR-UV experiments. An example of studies done on this band is given in Figure 19.

The main problem of recording an excitation spectrum in the low energy range is the appearance of background as is observed in the plot shown in Figure 19. Hence the intensity of the signal is not much and so is the depletion observed at 3019 cm^{-1} and 2952 cm^{-1} compared to the bands at and close to the 0-0 (Figure 7).

HYDROQUINIDINE

In order to find out the origin of the band located at -88 cm^{-1} to the red, which is unique to Hydroquinidine, attempts have been made to record an IR-depletion spectrum with the IR laser scanned in the ν(CH) range and the UV laser kept fixed at the band origin, a band at 25 cm^{-1} to the blue and the band at 88 cm^{-1} to the red. The objective is to compare the IR absorbance of the two transitions on either side of the band origin and find out whether they are different.

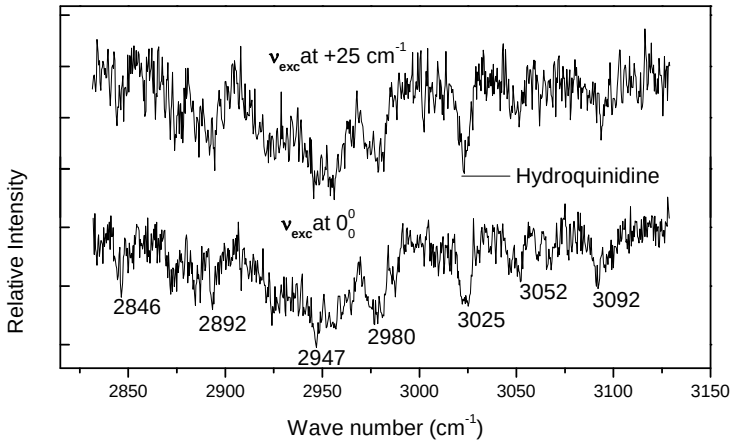

Figure 20*: IR-UV depletion spectra of Hydroquinidine in the ν(CH) range with the UV laser fixed at the electronic origin and the band at +25 cm^{-1}.*

As observed in the IR depletion spectrum of Figure 20, the species responsible for both the UV excitation bands at (0-0 and 25 cm^{-1}) absorb at the same wavelengths in the ν(CH) region. Hence the band at 25 cm^{-1} is most probably due to the same conformer which gives rise to the electronic origin, confirming the hypothesis that it belongs to a vibrational progression. The

+50 cm^{-1} band has been probed too; it shows exactly the same spectrum, confirming the fact that it is the third member of the vibrational progression.

The same procedure has been applied to the -88 cm^{-1} band and those which follow.

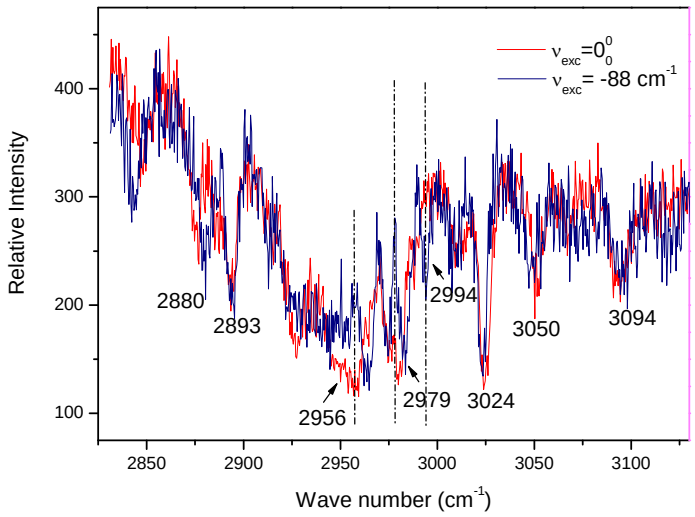

Figure 21*: IR-UV depletion spectra of Hydroquinidine in the ν(CH) range with the UV laser fixed at the electronic origin (red) and the band at -88 cm^{-1} (blue).*

From the plot shown in Figure 21 there is clearly a difference in absorption between the two spectra at ν(CH) stretch frequencies of 2994, 2979 and 2956 cm^{-1}. Hence the band to the red at -88 cm^{-1} appears to originate from a conformer which does not belong to the band origin.

IV. DISCUSSION : Existence of isomers and hot bands in case of Hydroquinine and Hydroquinidine

The low-frequency region of Hydroquinine and Hydroquinidine is rich with a large number of bands with/without following a vibrational progression as shown in Figure 7.

Changing the cooling conditions and recording the excitation spectra allows differentiating hot bands from cold isomers. It also allows differentiating conformers with different stability. However, if two different isomers have the same stability, they will behave in the same way when one

changes cooling conditions. As given in Figure 8 and Figure 9, both in Ar and Ne the band B (at 30646 cm^{-1}) observed in the spectrum of Hydroquinine is the most intense band of the spectrum at shorter distance between the jet and the excitation laser. This can be said because when the jet is moved closer to the excitation lasers the chances of the probe laser interacting with the cold molecules in the silent zone are increased. We can conclude from these observations that A is either a hot band or a conformer with lesser stability compared to B.

Similarly, the bands located at -88 and +3 cm^{-1} in Hydroquininidine do not seem to belong to the same species as that of the transition origin
Hence at this juncture the question that we ask ourselves is to know whether these bands belong to the same conformer or to hot bands.

Hydroquinine

Do the bands A and B belong to the same conformer?

The answer to this question has been found by performing IR-UV double resonance. While no obvious differences can be observed in the ν(OH) range (Figure 16), the ν(CH) region (Figure 17) shows slight differences in absorbance. As shown in Figure 17 the bands A and B absorb differently at 3004 and 2997 cm^{-1}. If we follow the energetic trends given by the calculations, it is tempting to assign band A to cis-γ-open(3b). The calculated frequencies of the cis-γ-open(3a) and cis-γ-open(3b) conformers of Hydroquinidine resemble each other mostly in the CH stretch region with closely related coupling between the CH_2 stretch vibrations in the Quinuclidine unit. However, the differences observed between the experimental spectra of bands A and B are not reflected in the calculated spectra of cis-γ-open(3a) and cis-γ-open(3b) which are very similar. Another possibility would be to assign band A to a higher-energy conformer like the cis-β-closed(7b) conformer, despite the energetics say otherwise.

Indeed, the vibrations observed in the infrared range (3000-3150 cm^{-1}) are different for the open and closed conformers. This range mainly involves the asymmetric CH stretch of the CH_3 group of the ethyl substituent, and the asymmetric CH_2 stretch modes in the Quinuclidine ring. These modes are strongly coupled to each other and it is the nature of coupling between

the asymmetric CH stretches of the CH_3 group and the asymmetric CH_2 stretch modes in the Quinuclidine ring which differentiates the two conformers. In the open form the coupling with the asymmetric CH stretches of the CH_3 group is distributed over almost all the CH_2 groups of the Quinuclidine ring. Even a vibration with a frequency down to 3032 cm^{-1} involves a contribution from the asymmetric CH stretch of the CH_3 group of the methyl substituent. In the closed form the coupling to the asymmetric CH stretch of the CH_3 group is much more limited, it mainly involves asymmetric CH stretch localised on CH_2 group close to the alkaloid Nitrogen. This results to characteristic fingerprints; the vibration calculated at 3138 cm^{-1} has as a major and almost only component involves the asymmetric CH_2 stretch of located on the C atom next to the nitrogen atom and on the other side relative to the ethyl substituent. It is calculated only for the closed form.

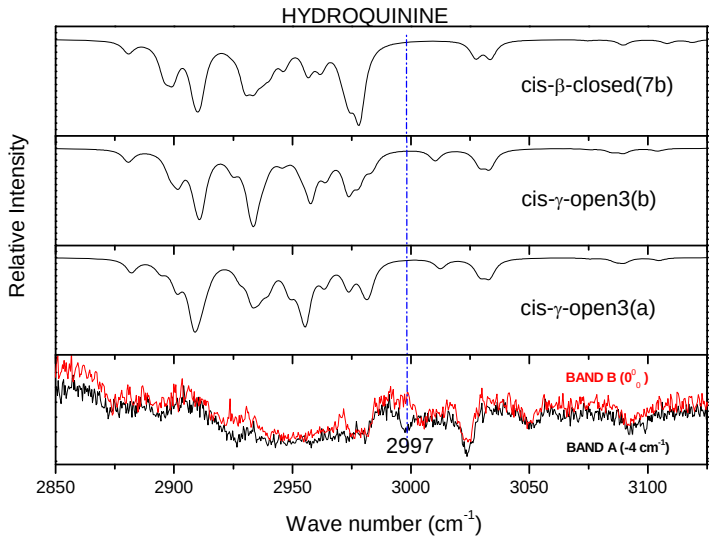

Figure 22: *The comparison between the infrared spectrum in the ν(CH) range obtained experimentally (shown at the bottom) and simulated one. The calculated spectra belong to cis-β-closed(7b) (top), cis-γ-open(3b) (middle) and cis-γ-open(3a) (bottom) conformers.*

However, as seen in Figure 22, the quality of the IR spectra does not allow us to give a clear assignment. It seems that the Hydroquinine is so

difficult to cool down that its IR spectrum in the CH stretch region is always broad.

Not just the low frequency region, but a particular band at the red (200 cm^{-1}) has also been probed with resonant IR and UV lasers (Figure 19) and it shows absorbance at infrared wavelengths 2952 and 3019 cm^{-1} which is characteristic of the band B (band origin). Thus it can be said that it belongs to the same conformer as that which gives rise to the band origin. Thus from the IR-UV study on five intense bands (0-0, +6, +14, -4 and-200 cm^{-1}) in the low-frequency region and to the red, it can be said that there is a possibility of existence of more than one species in the supersonic jet containing Hydroquinine but it is difficult to conclude whether they belong to different conformers or hot bands present in the jet.

Hydroquinidine

The low-frequency region of Hydroquinidine is particularly interesting as it contains two distinct vibrational progressions built on a mode of ~25 cm^{-1}, one of which starts from the band origin and the other from a band 88 cm^{-1} to the red. In contrast with Hydroquinine, Hydroquinidine can be cooled down enough so that the CH stretch range displays well distinct bands.

From Figure 21 it is observed that IR spectra obtained with the probe set on the band origin and at -88 cm^{-1} are different in the range 2955-3000 cm^{-1}. Similar scan performed in the ν(CH) range with the UV fixed at 25 cm^{-1} to the blue shows absorption at similar wavelengths as is observed in case of UV fixed at band origin (Figure 20).

Like in Hydroquinine, it is tempting to assign the origin and the band at -88 cm^{-1} to cis-γ-open(3a) and (b). However, the IR spectrum obtained by probing the band at -88 cm^{-1} resemble that of cis-γ-closed(1b) more than it does cis-γ-open(3a) as given in Figure 23. There is therefore a contradiction between the calculated energetics and the spectroscopic results.

*Discrepancy between experimental and theoretical results***.**

In Hydroquinine and Hydroquinidine as well, two low-energy conformers are expected from the calculations. However, the assignment

resting on energetics seems to be at odd with the results of vibrational spectroscopy.

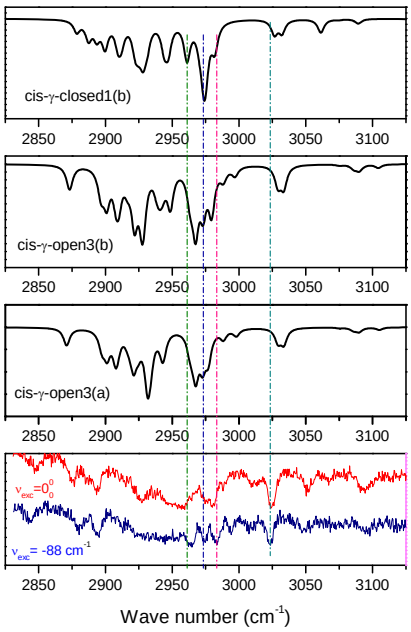

Figure 23: *The comparison between the experimental IR spectrum in the ν(CH) range (bottom) and simulated one. The calculated spectra belongs to cis-γ-closed(1b)(top), cis-γ-open(3b)(middle) and cis-γ-open(3a)(bottom) conformers.*

In all the studied molecules, it is difficult to draw an analogy between the differences observed experimentally and the calculated frequencies. One of the reasons for that can arise from experimental difficulties. Indeed, as mentioned earlier, Quinine derivatives are difficult to ablate and to cool down; and it is known from the experience of the past that double resonance spectra are difficult to obtain for insufficiently cooled molecules.

The scaling factor of 0.96 might not be accurate enough to have well matching between the experimental and calculated frequencies. Moreover, the scaling factor might be different for different types of modes.[6] [7] The method used in the calculations might not be precise enough as:

- Closed and open conformers have unequal configuration interaction components which are not reproducible by B3lyp.
- Due to the presence of an internal basis set superposition error (BSSE) which is not corrected for and might be different for the open and the closed forms.

However, one is provoked to assign the bands at -4 cm^{-1} in Hydroquinine and -88 cm^{-1} in Hydroquinidine to the other cis-γ-open(3) conformer (either a or b). The reasons behind such assignments are due to the results obtained from calculations which are identical irrespective of the method followed. Secondly the obvious differences observed in the experimental LIF spectrum. For instance in the excitation spectrum of Quinidine, one sees a set of bands at 0-0, +23, +45 cm^{-1} and while for Hydroquinidine there are two sets, one consisting 0-0, +25 and +50 cm^{-1} and another starting from -88 cm^{-1} which is most likely to be the other conformer.

Cooling down the molecules using a different valve and avoiding the saturation by the IR laser are planned in the future to confirm the above hypothesis of two conformers of Hydroquinine and its pseudoenantiomer.

V. CONCLUSION

Hydroquinine and its pseudoenantiomer have been introduced intact in gas phase and their electronic and vibrational spectroscopic fingerprints have been studied. Just like Quinidine was easier to ablate than Quinine, Hydroquinidine is easier to ablate than Hydroquinine.

Just like the other pair of cinchona alkaloids, Quinine-Quinidine, the two above-mentioned pseudoenantiomers absorb in the same frequency range with their band origins separated by only 2 cm^{-1}. Since all the four molecules have a Quinoline ring as chromophore, they show a $\pi \rightarrow \pi^*$ transition (lowest-energy transition) which is characteristic of 2-substituted Naphthalene derivatives. Also, another common feature for the four cinchona alkaloids is that they are weakly fluorescent with no $n \rightarrow \pi^*$ charge transfer observed in the fluorescence emission spectra.

Hydrogenation of the peripheral vinyl group has consequences on the fluorescence excitation spectrum Hydroquinine and Hydroquinidine, which are more pronounced in the latter case. As shown in Figure 7 both Hydroquinine and its pseudo-enantiomer show a more congested low

frequency region than Quinine and Quinidine. The low-frequency region is particularly important as it clearly differentiates the four molecules. Amidst the numerous hot bands and low-frequency modes as expected for a molecule so flexible, Hydroquinidine stands apart with a distinctly different excitation spectrum composed of two distinct vibrational progressions in the low-frequency region at a gap of 88 cm^{-1} as opposed to the rest three molecules. When the origin transition frequencies of these two progressions of Hydroquinidine are probed with an IR laser, they absorb at different frequencies thereby confirming that they belong to different species.

In the gas phase, three and nine conformers of Hydroquinine and Hydroquinidine have been calculated respectively, with $\Delta G<1.5$ kcal/mol at room temperature. Among them the most stable ones, cis-γ-open-(3a) and cis-γ-open-(3b), are almost equally abundant in each molecule

The differences between the two pseudoenantiomers are neither observed in their zero-point energies (271 kcal/mol in case of both) nor in the ν(OH) stretch modes involving the chiral linker. The differences manifest itself only in the asymmetric ν(CH) stretch modes localised on the Quinuclidine unit and in very low frequency modes, and in the number of conformers populated at room temperature. It is interesting to note that asymmetric CH stretch modes localised on the Quinuclidine unit is the most sensitive to subtle changes in the molecule, either chirality of the linker (pseudoenantiomerism), or conformation.

It is difficult to assign the intense bands in the low-frequency region of the experimental spectrum to the calculated low-energy conformers as the calculated frequencies of both the conformers are similar.

Comparison between open (low energy) and closed (high energy) conformers show slight differences in frequencies which could account for the experimentally observed differences in the IR spectra, but their energetics tell otherwise. Lastly it might be the case that the band almost equally intense to the electronic band origin for both hydroquinine (-4 cm^{-1}) and hydroquinidine (-88 cm^{-1}) might be hot bands. However, on the basis of the similarity between the laser-induced fluorescence spectra and on the basis of energetics, we tend to assign the bands observed at -4 and -88 cm^{-1}

for Hydroquinine and Hydroquinidine, respectively, to the second stable isomer. Further TDDFT calculations can give an idea of the excited state energy and thus give an idea about the source of the bands.

As observed in the earlier chapter these high-energy conformers are more abundant in solution than in supersonic-expansion conditions. Hence VCD studies in solution are eagerly awaited to confirm the abundance of higher energy conformers in case of Hydroquinine and Hydroquinidine too.

Among the high energy conformers calculated, a majority of them have the “closed” geometry. Cinchona alkaloids are prone to show differences in energetics in solution due to high energy conformers of “closed” geometry which are not observed in gas phase.[3] Indeed temperature dependent NMR studies done on Hydroquinidine in solution also shows a greater population of the syn-closed form (10-20 %) as compared to gas phase.[4]

The difference between the number of conformers calculated for Hydroquinidine and its pseudoenantiomer is larger than that of the Quinine/Quinidine pair. Since the number of stable conformers of Quinidine increases in solution compared to gas phase, one expects the same trend for Hydroquinidine too. Therefore, one anticipates less mirror-image relation in the VCD spectra for the hydrogenated species.

As discussed above, Hydroquinidine stands out with an excitation spectrum showing two transitions separated by 88 cm^{-1}. Hydrogenation increases the difference between the excitation spectrum of the pseudo enantiomers.

Thus it can be said that the differences between the pseudoenantiomers which was almost negligible for Quinine and Quinidine is more pronounced in case of Hydroquinine and Hydroquinidine.

VI. References

1 E. Smith., S. Barkan., B. Ross., M. Maienthal., and J. Levine., Journal of Pharmaceutical Sciences 62 (7), 1151 (1973); M. Edstein., A. Prasitthipayong., A. Sabchareon., T. Chongsuphajaisiddhi., and H. Webster., Therapeutic Drug Monitoring 12, 493 (1990).

2 A.Nontprasert., S.Pukrittayakamee., D. E. Kyle., S.Vanijanonta., and N. J. White., Transactions of the royal society of tropical medicine and hygiene 90, 553 (1996).

3 J. F. Lai, Z. Ma, L. Mink, L. J. Mueller, and F. Zaera, Journal of Physical Chemistry B 113 (34), 11696 (2009).

4 U. Berg., M. Aune., and O. Matsson., Tetrahedron Letters 36 (12), 2137 (1995).

5 M. J. Frisch, G. W. Trucks, H. B. Schlegel, G. E. Scuseria, M. A. Robb, J. R. Cheeseman, G. Scalmani, V. Barone, B. Mennucci, G. A. Petersson, H. Nakatsuji, M. Caricato, X. J. Li, H. P. Hratchian, A. F. Izmaylov, J. Bloino, G. Zheng, J. L. Sonnenberg, M. Hada, M. Ehara, K. Toyota, R. Fukuda, J. Hasegawa, M. Ishida, T. Nakajima, Y. Honda, O. Kitao, H. Nakai, T. Vreven, J. Montgomery, J. A. , J. E. Peralta, F. Ogliaro, M. Bearpark, J. J. Heyd, E. Brothers, K. N. Kudin, V. N. Staroverov, R. Kobayashi, J. Normand, K. Raghavachari, A. Rendell, J. C. Burant, S. S. Iyengar, J. Tomasi, M. Cossi, N. Rega, J. M. Millam, M. Klene, J. E. Knox, J. B. Cross, V. Bakken, C. Adamo, J. Jaramillo, R. Gomperts, R. E. Stratmann, O. Yazyev, A. J. Austin, R. Cammi, C. Pomelli, J. W. Ochterski, R. L. Martin, K. Morokuma, V. G. Zakrzewski, G. A. Voth, P. Salvador, J. J. Dannenberg, S. Dapprich, A. D. Daniels, O. Farkas, J. B. Foresman, J. V. Ortiz, J. Cioslowski, and D. J. S. Fox, Gaussian 09, Revision A.02 (Gaussian Inc., Wallingford CT, 2009).

6 H. S. Biswal, Y. Loquais, B. Tardivel, E. Gloaguen, and M. Mons, Journal of the American Chemical Society 133 (11), 3931 (2011).

7 E. Gloaguen, H. Valdes, F. Pagliarulo, R. Pollet, B. Tardivel, P. Hobza, F. o. Piuzzi, and M. Mons, The Journal of Physical Chemistry A 114 (9), 2973 (2009).

CHAPTER IV

Chiral Recognition in ionic complexes: Protonated Alanine and Camphor

INDEX

List of figures

List of tables

I. INTRODUCTION

The motive behind this study is to understand chiral recognition processes in ionic complexes. This study differs from those reported in the previous chapter in the following manner. Firstly, it involves charged species. Hence, the complexes are bound by much stronger interactions such as charge-dipole interactions between an ionic and a neutral species. Secondly, in contrast with the studies in a supersonic expansion, th study has been done in an ion trap at room temperature and hence anharmonicity and temperature effects are expected to play a role. In particular, the spectra obtained will show hot bands. Thus to simplify the analysis, we have first focused on interactions between small ionic species like the protonated alanine with camphor.

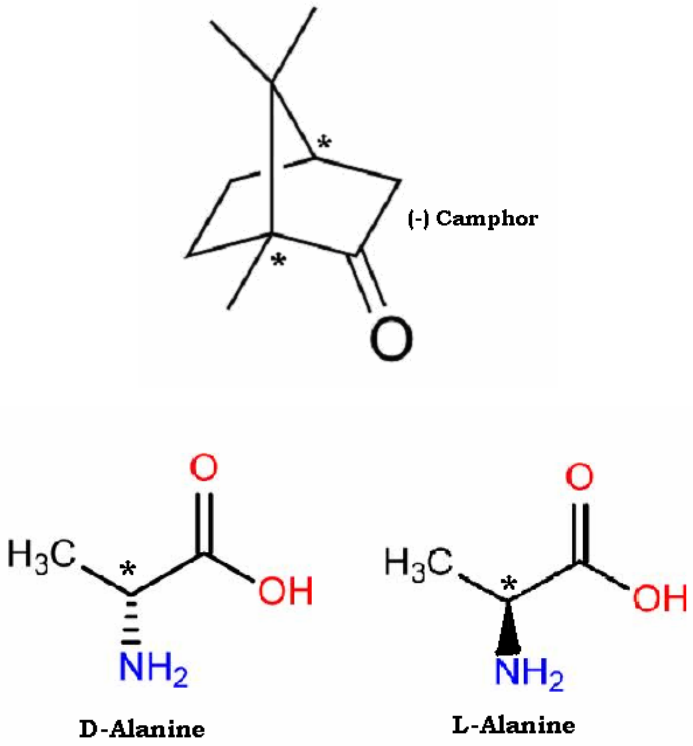

Figure 1*: Structures of (-) Camphor and D and L Alanine.*

Camphor, one of the components of turpentine, belongs to the family of terpenoid molecules and can be found naturally in some plants like laurel or rosemary. It is a rigid bicyclic compound which has two stereogenic chiral centres and exists only as two stereoisomers, the other pair not formed due to steric

reasons. Alanine is an α-amino acid which exists as zwitterionic form at pH between 2.2 and 9.4, as negative carboxylate anion at pH>2.2 and as positive ammonium cation at pH<9.4. It has two optical isomers, D and L Alanine which are mirror image to each other and among which the L isomer is present in all proteins.

The interaction between the two enantiomers of protonated alanine with the carbonyl group of camphor has been studied. This study is done within the context on previous studies of the group which tended to show that chiral recognition was more difficult to attain with systems which are not flexible enough for secondary interactions to be achieved, because the secondary interaction which are thought to be necessary for chiral recognition cannot take place in too rigid a system.[1] [2] More precisely, one wants to know whether the two rigid enantiomers of alanine interact differently with the chiral environment (camphor) from both an energetic point and spectroscopic point of view. This is achieved by analyzing the dissociation pathways of the dimers formed by L and D protonated alanine with camphor using collision-induced dissociation (CID) and the spectroscopic technique of Infra Red Multiple Photon Dissociation (IRMPD). In this chapter the homochiral dimer formed between *S*(-)Camphor and *S*(+)L Alanine has been termed by their respective absolute configurations and acronym of their names (Ala and Cam) as SS-Cam-AlaH$^+$. Similarly, the heterochiral dimer formed between S(-)Camphor and *R*(-)D Alanine has been named as SR-Cam-AlaH$^+$.

In the following sections the details of the experimental techniques will be explained followed by the results obtained by experiment and subsequent discussion with results obtained from calculations.

II. EXPERIMENTAL SET-UP

II.1. A Quadrupole Paul-ion trap "Esquire 3000+" combined with an electrospray ionization source

The aim of this experiment is to study gaseous ions generated from a solution with the help of a mass-spectrometer. This is done with the help of a

technique known as Electrospray Ionisation Mass Spectrometry (ESI-MS) developed by Fenn and co-workers[3]. Dr J.B Fenn was rewarded with a Nobel Prize in the year 2002 for the development of the electro-spray ionization source. This highly sensitive ionisation technique has the following three advantages:

- Ability to produce multiple charge ions of high molecular weights.
- As a liquid-phase ion source, it allows the study of ions in solution.
- Ability to preserve the non-covalent interactions of ions that exist in the solution, thereby acting as a "soft" ionisation technique.

All the experiments discussed in this chapter have been performed in an API-ESI (Atmospheric Pressure Interface-ElectroSpray Ionization) device which generates ions, focuses and transports them into the ion trap mass analyzer. The Figure 2 gives an overall view of the set up:

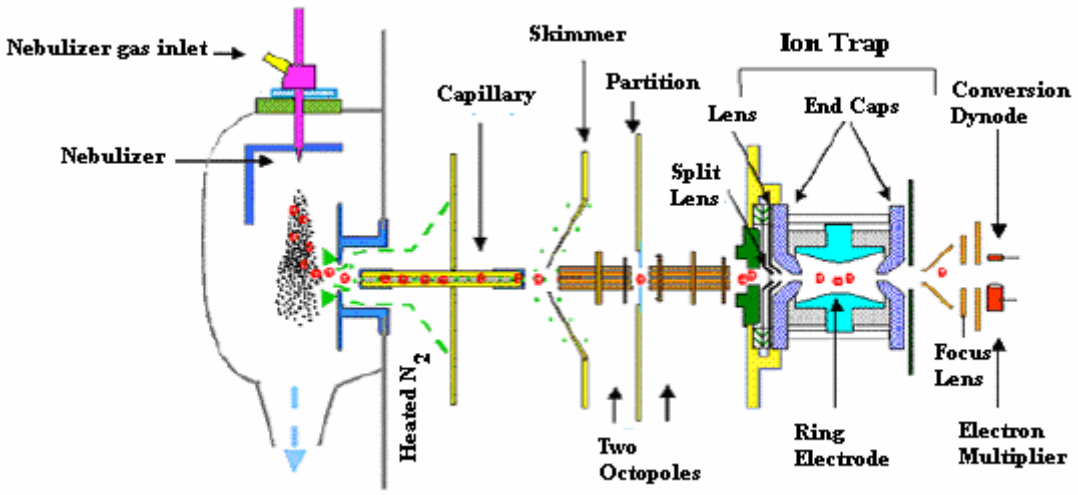

Figure 2: *Diagram of the electro-spray ionization source combined with a Paul-ion trap. The above scheme has been taken from the manual of BRUKER.*[4]

The setup can be described briefly to contain an external unit to generate ions, an ion trap to store the ions and then to eject them according to mass and lastly an ion detector to measure the number of ions of a given mass. The various stages of the instrument are controlled by electronic modules (e.g standard Bruker Esquire Control version 5.2[5]) which manage the parameters necessary for the generation, accumulation and analysis of ions. High vacuum is maintained in the ion transport and focussing region to ensure efficient ion transmission in

detection. In the following section the different stages in ion trap mass spectrometry will be discussed.

II.2. Electro-spray ionization

It is a technique well suited to analyse weakly volatile large molecules in the gas phase, without heating or fragmenting them.

In a standard electrospray ionisation set up, the sample is dissolved in a polar, volatile solvent and pumped through a narrow, stainless steel capillary at a suitable flow rate. A high voltage is applied to the tip of the capillary, which is situated within the ionisation source of the mass spectrometer. Due to the high voltage a strong electric field is generated which extracts the ions at the exit of the needle. Because of the competition between the surface tension and the electrostatic forces at the exit of the needle, the liquid undergoes some deformation and takes the shape of a cone, called the Taylor cone. Additionally, a nebulising nitrogen gas flowing around the exterior of the capillary is introduced co-axially. The combination of strong shear forces generated by the nebulizing gas and the strong electrostatic field draws out the sample solution from the tip and breaks it into an aerosol of highly charged droplets. The nebulizing gas is important for good spray and steady ion current.

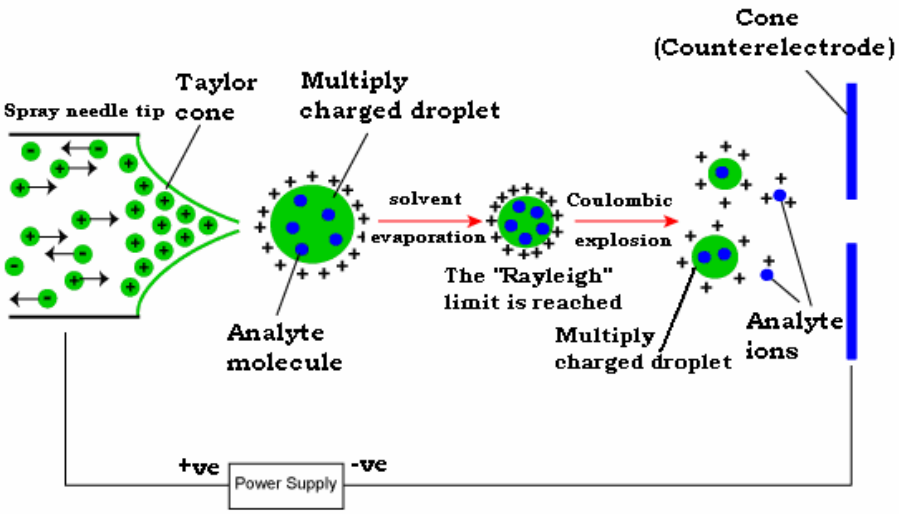

Figure 3: *A scheme showing the formation of ions by electro-spray method. The above figure has been taken from the mass spectrometry resource of department of chemistry of University of Bristol.*[6]

Next, when the repulsion between charges is larger than the surface tension, the highly charged droplets undergo Coulomb explosion and break into smaller droplets. This process happens several times, leading to smaller and smaller droplets. A drying gas, usually N_2, heated at a temperature which depends on the sample studied, is introduced into the spray chamber and helps evaporating the solvent from the droplets. A figure showing the charged droplet formation is given in Figure 3.

The high voltage electrostatic gradient present in the spray chamber guides the ions towards a glass capillary. While the spray chamber is outside the vacuum manifold, the ion transport and focusing components lie within it. This pressure difference between the two regions pushes the ions through the capillary. The capillary introduces the ions into the ion trap; it is also used for separating the high-pressure region (electrospray region) from the low-pressure region (Paul ion trap). Last, the ions are guided through ion optics (in particular two lenses) to enter the trap.

II.3. The Paul-ion trap (a quadrupole ion-trap)

A quadrupole ion trap is a multifunctional device, small in size and cost-effective when compared to other spectrometers, which can be used to analyse ions and store them long enough for performing experiments. It consists of two end caps and a ring electrode. Holes at the centre of the two end-caps act as entry and exit ports for the ions. An oscillating potential difference between the ring and end-cap electrodes generates a quadrupolar field which traps the ions. A quadrupolar field can be thought of as a pseudo-potential well, the depth of which is related, among other things, to the mass-to-charge ratio of the ion, the geometry of the trap, and the magnitude of the applied radiofrequency voltage. Analysis of the motion of the ions on the axis r of the trap (between the ring electrodes) show that it is dictated by a frequency called “secular frequency” which depends on m/z. Perpendicular to the axis of the trap, a potential is applied between the out coming endcap electrode and the entrance cap electrode so that the ions are maintained in the trap.

Since the ions are produced outside the ion trap, they tend to "*roll down*" into the pseudo-potential well and keep "*rolling back up*" until they exit the trap in order to follow the law of conservation of energy. Hence a collision gas, in the form of He is added so that collisions with He take away energy from the ion beam thereby forcing a part of the ions to remain inside the pseudo-potential well. The figure below depicts the ions trapped in a pseudo-potential well.[4 7 8]

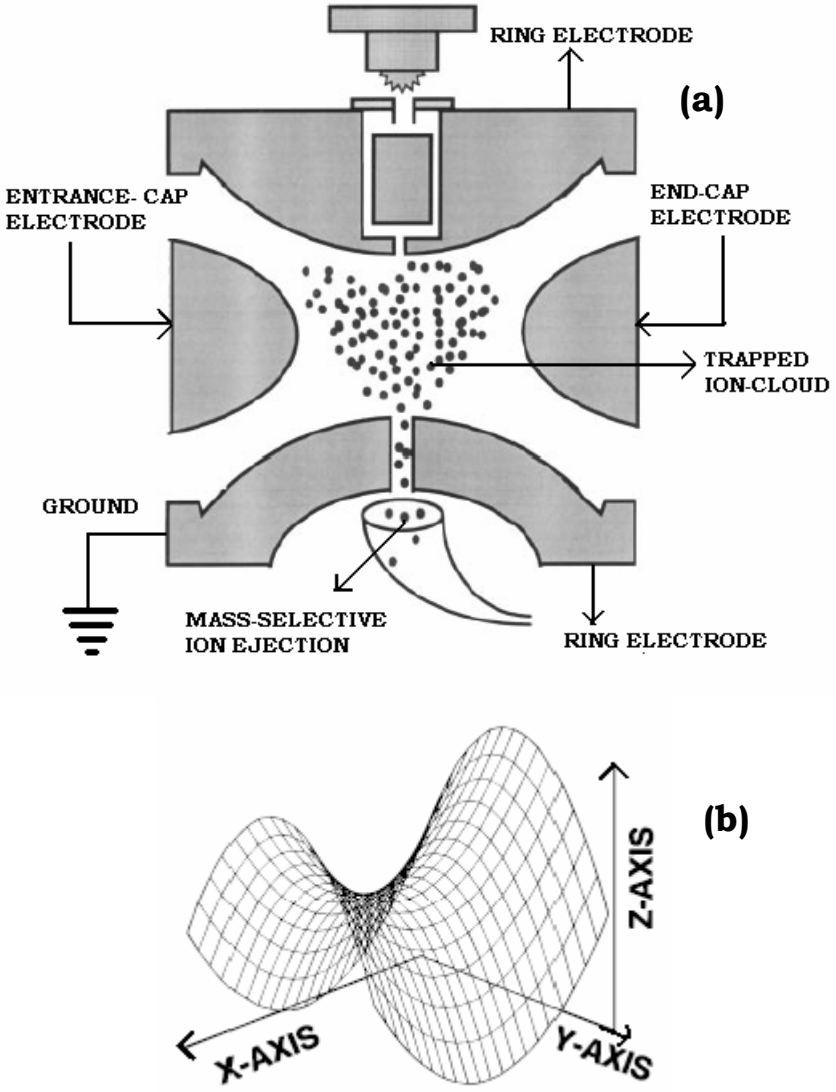

Figure 4: *(a) Ion cloud trapped inside a Paul-ion trap formed between two end cap electrodes and a ring electrode; (b) Potential surface (quadrupolar field) inside a quadrupole ion trap.* [8]

The ions which come out of the trap are detected by a detector. This detector is a conversion dynode based system (Daly detector). It is particularly

useful for highly sensitive detection of both positive and negative ions. An ion lens is also present in the detector to focus the ions on it.[4]

We shall now describe the kind of experiments which can be done in an ion- trap:

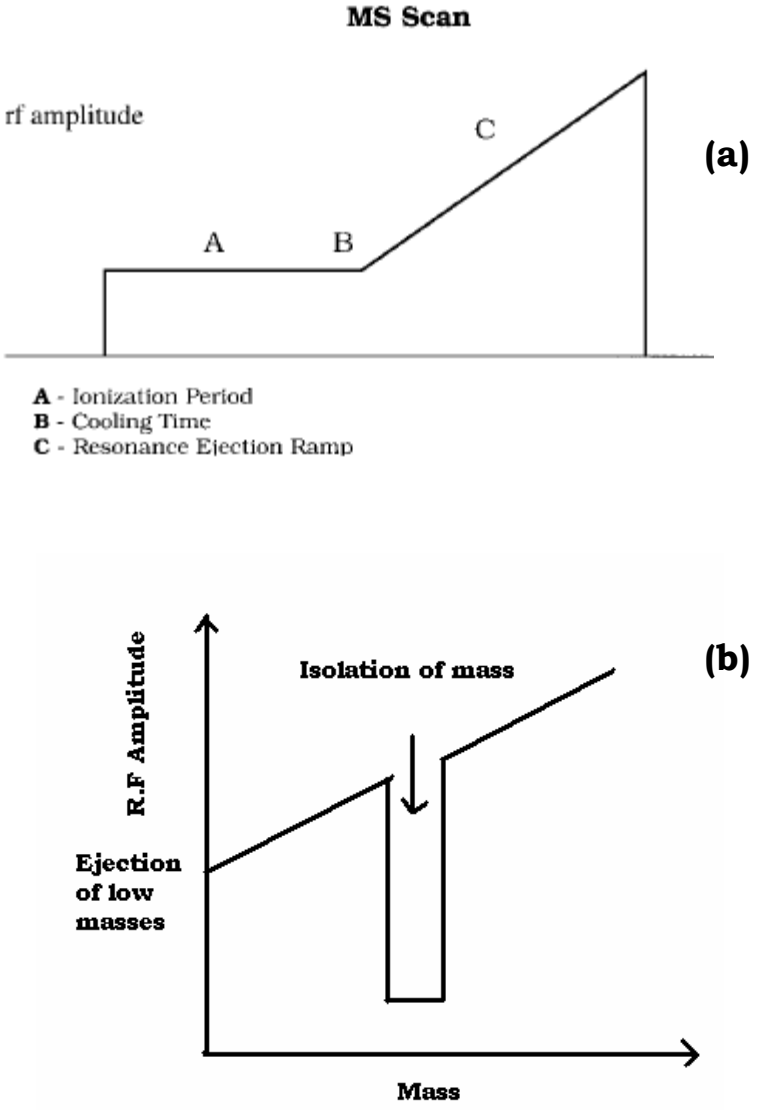

Figure 5: *(a): Scheme of a typical MS scan. For the MS scan, A=ionisation period, B=cooling time and C= resonance ejection ramp;[9] (b) Principle of isolation of mass.*

Mass Spectrum (MS) by resonant ejection

Each ion in an ion trap oscillates at its own secular frequency. When an additional voltage is applied to the ring electrode, whose frequency matches with the secular frequency of a particular ion, a resonance is established between them. This results in an increase in the amplitude of oscillation of the particular ion till a point is reached when it is so unstable that it gets ejected from the trap.

By scanning the amplitude of the RF voltage, one can eject successively the different ions present in the trap and detect them on the detector. Doing this, one can record a mass spectrum (MS) which describes the different masses contained in the trap.

Isolation of ions and fragmentation

A lot of information is given by analysing the dissociation patterns of an ion. However, before the dissociation of a precursor ion, it is necessary to remove all the other ions present inside the trap so that only the product ions are present. To do that, one varies the RF voltage amplitude so that one can eject all the ions from the trap except the desired one.

II.4. Collision induced dissociation

If the voltage with a frequency resonant to a particular ion is applied in smaller amplitude, there is a possibility for the ion to be excited instead of being ejected. This is achieved by initially selecting a particular ion by rejecting all others by the process of resonant ejection and then adjusting the RF voltage so that it is at a similar secular frequency as that of the selected m/z which is to be resonantly excited.

The voltage is then gradually increased thereby increasingly accelerating/decelerating the targeted ion. This in turn increases the number of collisions with the He buffer gas present in the trap. During each collision the kinetic energy of the fast moving ions is converted into internal energy. Hence as the amplitude of resonant frequency is increased, the internal energy of the ion also increases.[10]

However, this deposition of internal energy is rather slow, since a small amount of it is imparted in each collision. Thus with the help of this method one can study the lowest energy unimolecular dissociation pathways of the ion. This technique is known as collision induced dissociation (CID). As the energy deposited in the molecule has time to be redistributed among all the intramolecular degrees of freedom (vibrational modes), CID can be described

within the frame of statistical reactions. As a result, the products of CID reactions correspond to the breakage of the weakest bond.

Then a radiofrequency voltage amplitude ramp is applied again to analyse the different masses resulting from the dissociation. This kind of experiments is called MS-MS spectrometry because it involves two steps of mass selection; the first one being isolation of the precursor, and the second one being mass analysis of the fragments. A scheme showing the MS/MS scan is given below:

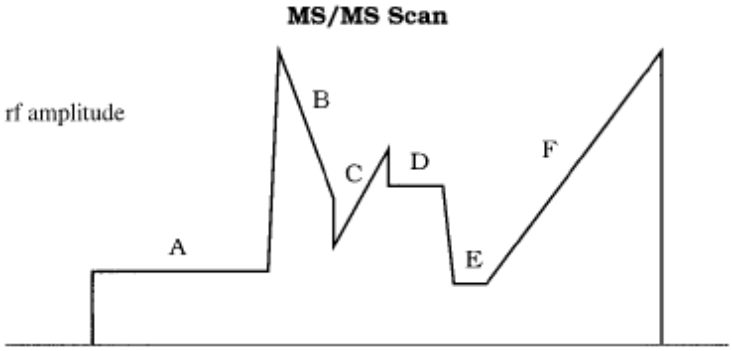

Figure 6*: Scheme of a typical MS/MS scan. For the MS/MS scan, A=ionisation period, B=reverse scan to eject ions of large masses, C= forward scan to eject ions of lower masses, D= resonance excitation period, E= cooling time and F= resonance ejection ramp.*[9]

Analysis of the MS-MS spectra brings information on the fragmentation pathways by giving the nature of the fragments resulting from the dissociation of the studied molecule, and the threshold of the radiofrequency voltage amplitude necessary for fragmentation. Indeed, the nature of fragments often depends on the structure of the molecule. For example, a molecule won't show the same fragmentation pattern whether there is an internal H bond or not. In the case of our study, the relative intensity of the fragments in the two diastereomer complexes gives information on their relative stability. However, one has to complement the CID experiments by other methods giving more direct structural information, such as infrared spectroscopy.

II.5. Infrared multiple-photon dissociation spectroscopy (IRMPD)

Infrared spectroscopy is a technique to identify molecular vibrations and hence determine the structure of molecular systems. Each atom or group of atoms show infrared activity in characteristic regions of the spectrum. In this

chapter, only the *fingerprint region* (< 2000cm^{-1}) of the infrared spectrum has been measured for the studied systems.

However, it is a challenging task to record direct absorption spectra of ions in gas phase since they exist in extremely low-densities (<10^8 cm^{-3}). *Infrared multiple-photon dissociation* (IRMPD) *spectroscopy* is a technique which can overcome this problem of sensitivity in an indirect manner.[11] [12] [13] [14]

Principle

When a mass-selected ion of interest is irradiated with a tunable infrared laser (free electron laser in this experiment), at a frequency which is in resonance with one of its vibration, the ion might absorb several infrared photons leading to its dissociation. The magnitude of ions undergoing unimolecular dissociation is a function of the laser wavelength absorbed and thereby can be presented in the form of a vibrational spectrum of the ion. Hence IRMPD spectroscopy is an indirect method for measuring the infrared spectrum of ions or in other words an "action" spectroscopic technique where a light absorption causes a change in the molecule. Such indirect techniques are more sensitive than direct absorption measurements.

This sequential and incoherent absorption mechanism can be divided into three zones (Figure 7).

Zone 1:

This zone is characterized by well-separated energy levels or in other words low density of states. Anharmonicity, if any, is weak in this region with few photons being resonantly absorbed.

Zone 2:

It is characterized by high density of mutually coupled states. The energy absorbed by the ion is rapidly lost into its bath of vibrational degrees of freedom by intramolecular vibrational redistribution (IVR). The IVR leads to de-excitation of the absorbing vibrational state by redistribution of energy into iso-energetic ro-vibrational states.

Here, the de-excited vibrational state may absorb new photons followed by redistribution of energy. Each absorption of new photon leads to a sequential increase in the internal energy of the ion till the dissociation threshold is reached.

Zone 3:

The final zone consists of a continuum of states where photo-dissociation occurs and fragment ions or neutral species are produced. After dissociation, most of the energy is stored as internal energy in th fragments. However, part of it might also be released as translational energy. Sequential dissociation is prevalent in such multi-photon dissociation experiments at high laser fluence and particularly in large systems.[15] Competing dissociation channels might be present if they lie too close to the lowest dissociation channel. A schematic diagram of the three zones discussed above is given below:

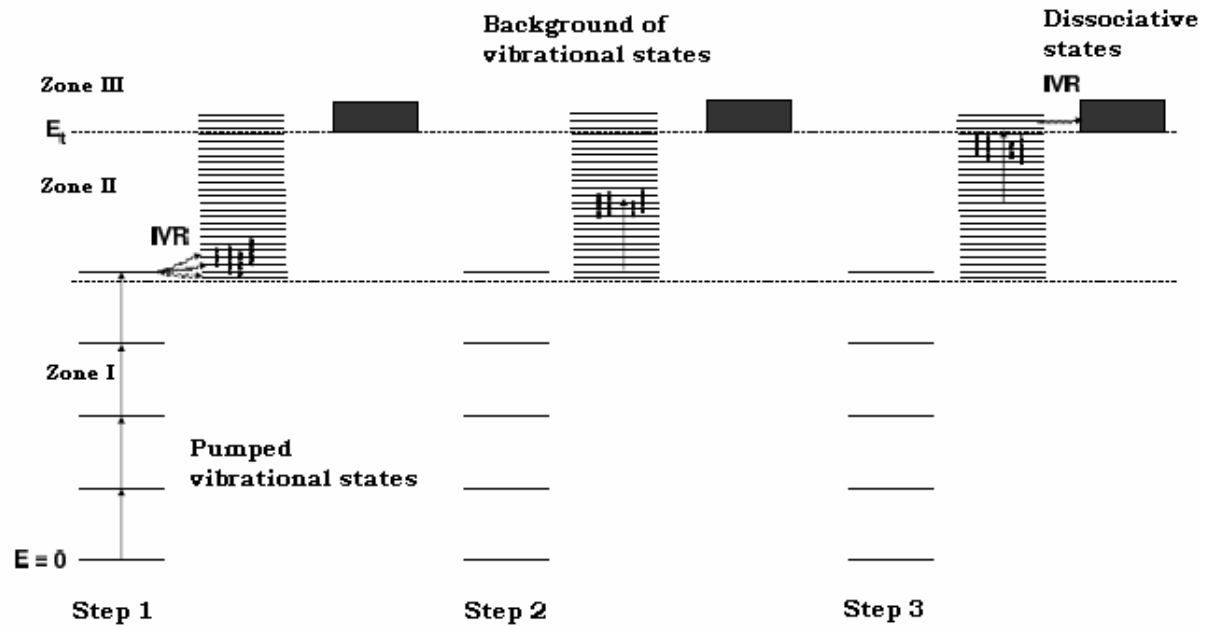

Figure 7*: A sequential incoherent absorption mechanism. Resonant absorption of few infrared photons followed by IVR to other vibrational modes (Zone 1); Quasicontinuum state with possible resonant transitions till the photo-dissociation threshold (E_t) is reached (Zone 2); Continuum of states where photo-dissociation occur (Zone 3). Adapted from the scheme described by Mukamel and Jortner.* [12,16]

Like in CID, IRMPD gives the fragments resulting from statistical dissociation.

The *Paul ion trap* used in CLIO Orsay has been modified by digging a hole of 1.2 mm diameter in the ring electrode[17]. This is done in order to allow access to the free electron laser used in our experiment. The IR-FEL beam enters through a

diamond window oriented near to the Brewster angle so as to obtain maximum transmission.

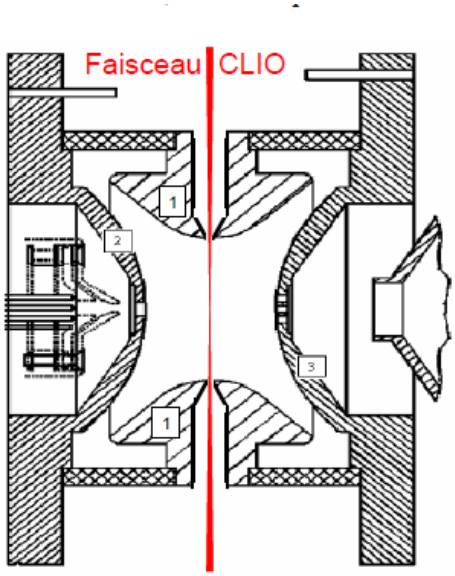

Figure 8: *Introduction of the laser beam to the RF ion trap through a hole dug in the ring electrodes.*[7]

II.6. Light Source: The Free Electron Laser (FEL)

A free-electron laser is well-suited to carry out IRMPD experiments due to its tunability over a wide spectral range (3-150 μm) and large spectral brightness (maximum peak power of 100 MW in 1ps). The free-electron laser used in this experiment has been developed in Centre Laser Infrarouge d'Orsay (CLIO) at Orsay, France[18]. The main difference between conventional lasers and a FEL is the use of high energy electron beam as an amplifying medium instead of excited atoms or molecules. The principle, design and radiation characteristics of the FEL will be briefly discussed in this section:

Principle

The source of radiation in a FEL is a bunch of electrons moving at relativistic speed under the influence of a magnetic field with oscillating polarity. The electrons are injected with the help of an electron gun into the magnetic field

structure called an *undulator* so that their trajectories are perpendicular to the magnetic field.[11,12,19] . The Figure 9 shows a scheme of the basic components of FEL.

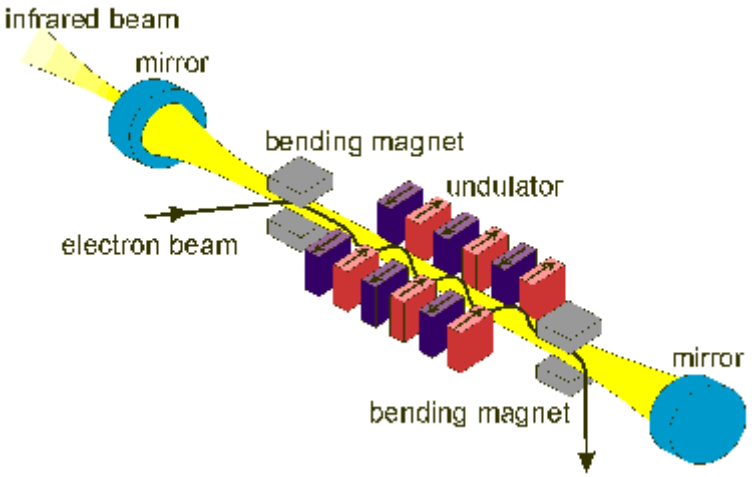

Figure 9: *Schematic of a free electron laser consisting of an electron gun, bending magnets and an undulator, the latter being placed inside a resonator cavity. The black arrow shows the trajectory of the electrons inside the cavity. The radiation is shown by the yellow coloured region between the two cavity mirrors. The radiation (infrared beam) exits the cavity through a hole in the centre of the cavity mirror placed at one of the resonator. Figure has been taken from the webpage of CLIO.*[19]

The electrons are first accelerated at relativistic energies (about 40 MeV) by a 20 m long linear Accelerator (LINAC). The produced bunches of electrons enters then the undulator, where they undergo a "wiggling" motion emitting a Synchroton radiation (SR) at each wiggle. These SR emissions can interfere leading to the so-called spontaneous emission of the undulator which is quite weak. However, when stored in an optical cavity, the spontaneous emission can be amplified by repeated circulation inside the undulator, via an energy exchange to the profit of the stored radiation and at the detriment of the electron beam, till the point of saturation is reached. Note that this amplification results in a *micro-bunching* of the electron beam, leading to a *coherent* emission: the laser effect.

Using the relativistic notations γ for the electron reduced energy, the radiated wavelength in laboratory frame is given by the following formulae:

$$\lambda_R = \frac{\lambda_0}{2\gamma^2}\left(1+\frac{K^2}{2}\right)$$

where λ_0 is the magnetic period of the undulator (see Figure 10) and K is proportional to the magnetic field on axis seen by the electrons.

The radiated wavelength thus depends on the energy of the electrons, the undulator period and the applied magnetic field. In practice at CLIO, the energy of the incoming electrons (after they exit from the linear accelerator) is chosen according to the wavelength range one wants to study. In our case, for the fingerprint region, it is around 40 MeV. The fine tuning of the wavelength is achieved by changing the magnetic field, *i.e* the air-gap between the magnetic jaws of the undulator.

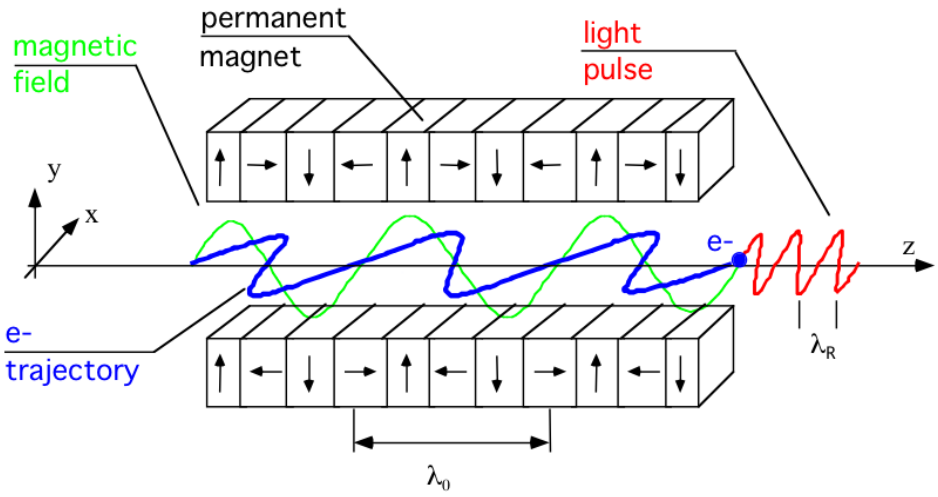

Figure 10: *Scheme of the transverse motion of the electron beam (shown in blue) perpendicular to the magnetic field (shown in green) and the corresponding emitted radiation (shown in red). Figure has been taken from the webpage of CLIO.*[19]

The pulse structure of the output radiation is dictated by the frequency of the injected electron beam and the microbunching process mentioned above. In case of CLIO, the macropulse train consists of short (0.5-3 ps) micropulses separated by 16ns, and appears in 9 μs bunches repeating at 25 Hz as given in the Figure 11. The band-width of CLIO laser is Fourier-limited. The spectral band-width is ~0.05% of the frequency, thus ranging from ~5 cm^{-1} at 1000 cm^{-1} to ~10 cm^{-1} at 2000 cm^{-1}. The high instantaneous power (100MW in 1ps) results in efficient photon-absorption and the time between two sub-sequent micropulses is long enough so that IVR takes place, so that it allows the re-absorption at the

fundamental transition. Thus a free electron laser is particularly useful for recording IRMPD experiments.[13,17,20]

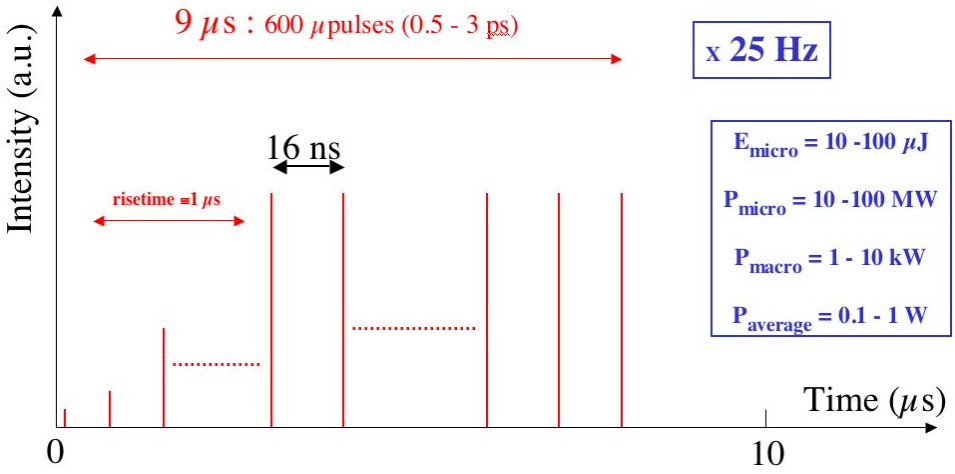

Figure 11: *Temporal scheme of the FEL used in CLIO. Figure has been taken from the webpage of CLIO.*[19]

II.7. Preparation of sample and experimental conditions

The capillary is kept at a voltage of -4200 V. The nebuliser is kept under 17 psi pressure. The dry gas is passed at a rate of 4L/mm and its temperature is maintained at 180 ºC. The skimmer is kept at 40V and the end cap exit is maintained at 109.2 V. The octopole RF is at 116 V (peak to peak voltage). The trap drive is at 26.2 V and the ions are accumulated in the trap for duration of 10 ms.

The sample solution prepared consists of 100μL of (-)(10^{-3} M) Camphor with 100μL of (10^{-3} M) D or L Alanine in 1mL of H_2O:CH_3OH (50:50) mixture. In our experiment the pH has been kept below 2.2 (pKa of carboxylic acid) by the addition of formic acid in order to obtain the protonated form of alanine.

II.8. Analysis of data

In our experiment (CID-MS^2), the fragmentation efficiency F has been calculated using the formulae:

$$F = -\ln \frac{[P]}{[P] + \sum [F_i]}$$

where, [P] and [F_i] represent concentrations of the parent ion and the fragment ions respectively, as measured in the MS^2 experiment.

The plots given in this chapter show the intensities of ionic complexes in function of the wavelength (cm^{-1}), and calculate their rates of fragmentation using the above-mentioned formulae.

III. EXPERIMENTAL RESULTS

III.1. Efficiency of formation

It has been found that *S* camphor has higher tendency to form a dimer with protonated *S* alanine than with *R* alanine in the ion-trap. Indeed, when solutions of identical concentrations are used in identical experimental conditions, one observes more complex in the case of the homochiral dimer.

III.2. Collision Induced Dissociation

Collision induced dissociation studies have been done on the homochiral and heterochiral dimers. The plots below show the CID on the two dimers. The mass 242 belongs to the protonated dimer and mass 90 belongs to the protonated alanine resulting from the dissociation of the dimer. We can conclude from this mass spectrum that CID of the dimer results to the dissociation of the intermolecular bond, which is not surprising as it is expected to be the weakest bond. The rates of fragmentation have been calculated and it has been found to be 0.39 for the homochiral dimer and 0.46 for the heterochiral dimer.

From the rates of fragmentation it can be said that the more difficult it is to form the dimers the easier they fragment. The homochiral complex is easier to form and more difficult to dissociate than the heterochiral complex. The mass spectrum (MS) and the CID-Mass spectrum of the two dimers are given in Figure 12.

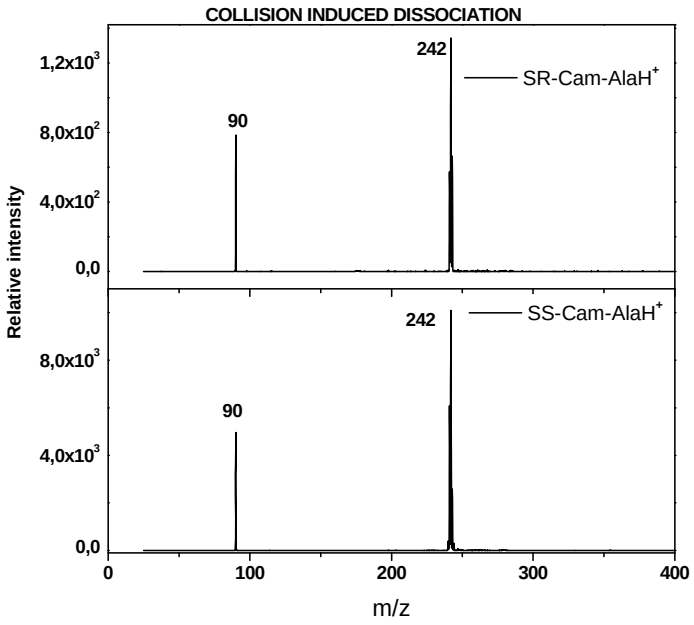

Figure 12*: CID-mass spectrum showing the intensities of protonated dimer and the protonated alanine fragment.RF=0.25Hz*

III.3. IRMPD Spectroscopy

The IRMPD spectra of the homochiral and heterochiral dimers have been recorded in the fingerprint region as given in the figure 12. In both the diastereomers the absorbed bands are broad in nature, broader than the resolution of the laser, with a band-width of ~40 cm^{-1}. The broad nature of the bands might be due to absorption by species which are not in their ground vibrational state and/or spectral congestion. In both cases the most intense absorption is at ~1690 cm^{-1} corresponding to the stretch mode of the carbonyl group. Broad and relatively intense absorptions are also observed at 1771, 1485 and 1173 cm^{-1} for the homochiral dimer and 1779, 1475 and 1164 cm^{-1} for the heterochiral dimer respectively.

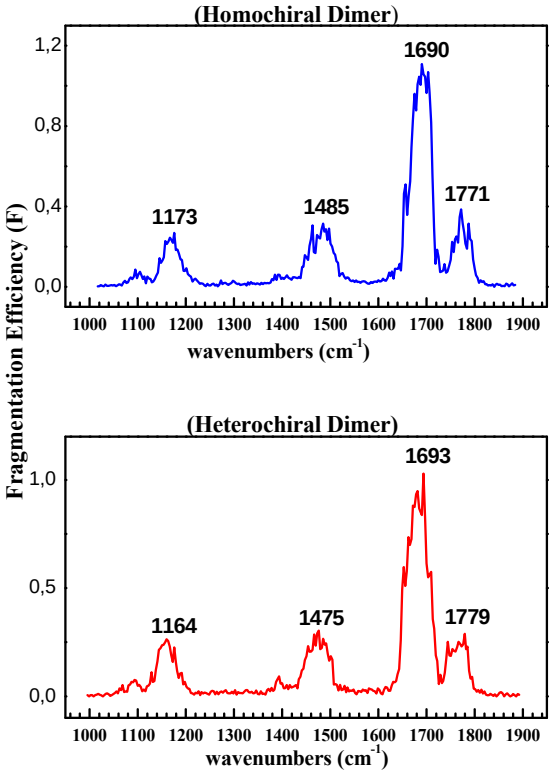

Figure 13*: IRMPD spectra of the homochiral dimer (above) and heterochiral dimer recorded experimentally in the region (1000-1900 cm-1)*

IV. RESULTS FROM CALCULATIONS

In order to know the nature of interactions between the protonated alanine and the camphor molecules, just the experimental results are not sufficient. Hence Gaussian calculations have been done using the method of b3lyp/6-31++g(d,p). The calculations have been done for the homochiral (SS-Cam-AlaH$^+$) and the heterochiral dimer (SR-Cam-AlaH$^+$). The most stable structure of the heterochiral and homochiral complexes is very similar. It consists of a protonated alanine, with the proton located on the most basic site, *i.e.* nitrogen, hydrogen-bonded to the keto group of camphor. The structures of the most stable and abundant conformers of the homochiral and heterochiral dimers are shown in Figure 14 with the N-H and O-H distances and N-H-O angle.

Calculations confirm the experimental results which show that in case of both the dimers the proton has greater chances of being attached to the less

electronegative N (3.04) compared to oxygen (3.44). In both the dimers the O-H distances are much larger than the N-H distances. The N-H--O bond angle for the homochiral and heterochiral dimers are identical with the values 164° and 165° respectively. The intermolecular distances are identical too (1.6 Å).

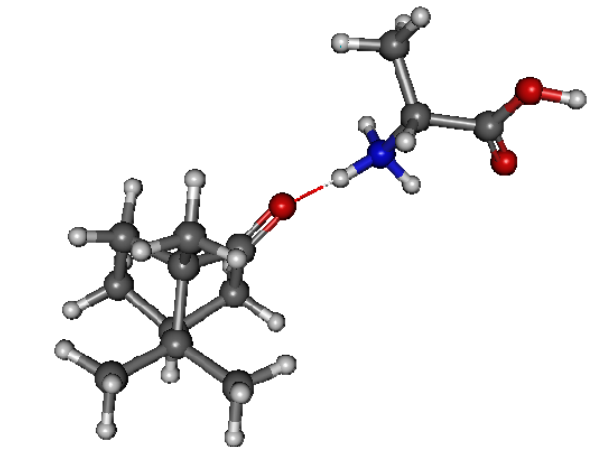

$N-H:1.07\,\mathring{A}\quad H-O:1.59\,\mathring{A}$
$N-H-O:165°$
SR - Cam - $AlaH^{+}(1)$
(heterochiral dimer)

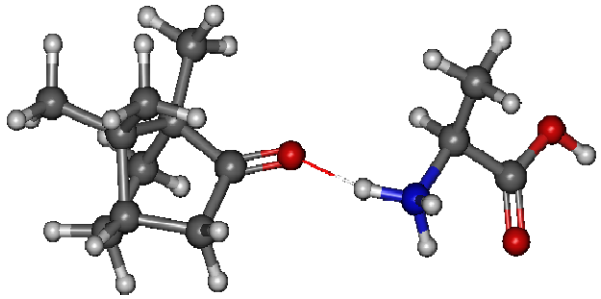

$N-H:1.07\,\mathring{A}\quad H-O:1.59\,\mathring{A}$
$N-H-O:164°$
$SS-Cam-AlaH^{+}(1)$
(homochiral dimer)

Figure 14*: Structures of the heterochiral dimer (above) and the homochiral dimer (below) showing H-bond between the proton attached to the amine and the carbonyl oxygen of camphor. The N-H, O-H distances and N-H-O angle have been supplied for each dimer.*

In case of the heterochiral dimer, 6 conformers have been calculated. Among them, four have ΔG <1.7 kcal/mol. In case of the homochiral dimer, four conformers have been calculated and all of them have ΔG <1.7 kcal/mol. at room temperature. The Boltzmann populations and the ΔG values at room temperature of the two dimers have been given in Table 1.

HETEROCHIRAL DIMER			HOMOCHIRAL DIMER		
CONFORMER	**BOLTZMANN POPULATION (%)**	**ΔG (kcal/mol)**	**CONFORMER**	**BOLTZMANN POPULATION (%)**	**ΔG (kcal/mol)**
SR-Cam-AlaH$^+$ (1)	51.7	0	SS-Cam-AlaH$^+$ (1)	49.9	0
SR-Cam-AlaH$^+$(2)	17.5	0.64	SS-Cam-AlaH$^+$ (2)	42.1	0.1
SR-Cam-AlaH$^+$(3)	17.2	0.65	SS-Cam-AlaH$^+$ (3)	5.1	1.35
SR-Cam-AlaH$^+$(4)	7.2	1.16	SS-Cam-AlaH$^+$ (4)	2.9	1.68
SR-Cam-AlaH$^+$(5)	3.3	1.62			
SR-Cam-AlaH$^+$(6)	3	1.68			
	100			100	

Table 1*: List of Boltzmann populations and ΔG values of the calculated stable conformers of the two diastereomers.*

The digits in bracket signify their numerical order with increase in energy and decrease in stability. The calculated structures of the stable conformers of the two dimers are given in Figure 15.

It can be noted from Figure 15 and Figure 16 that all the dimers are bound by a NH$^+$---O=C hydrogen bond. Hence they display similar structures and only the orientation of the molecular frame of camphor is different. In other words there is some floppiness around the hydrogen bond.

In order to compare with the experimental results, simulated infrared spectra have been calculated in the fingerprint region for the homochiral and heterochiral dimers. The calculated vibrational spectra have been plotted after convoluting the scaled frequencies by a Lorentzian line shape of 22 cm^{-1} FWHM. The scaling factor used is 0.975. Only the dimers having contribution of more than 10% at room temperature have been taken into account in the simulations. In case of the homochiral dimer a weighted average between SS-Cam-AlaH$^+$(1) and SS-Cam-AlaH$^+$(2) conformers has been taken into account while for the

heterochiral dimer a weighted average between SR-Cam-AlaH$^+$(1), SR-Cam-AlaH$^+$(2), SR-Cam-AlaH$^+$(3) conformers has been calculated.

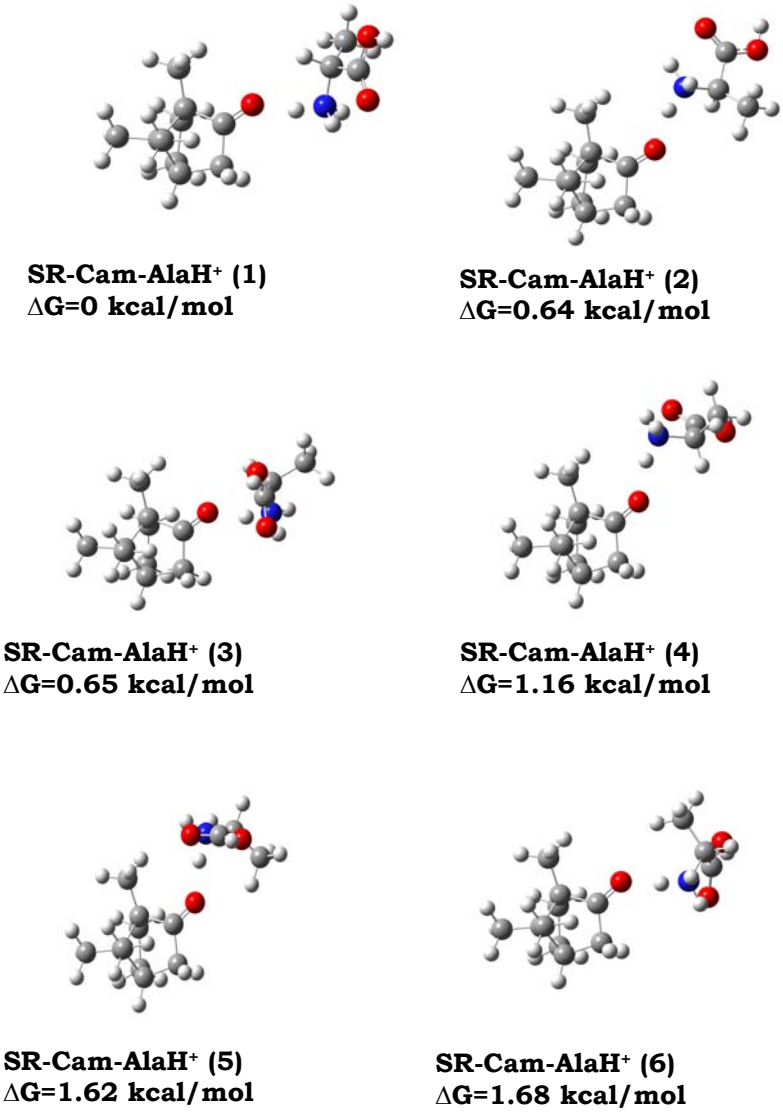

Figure 15*: Stable structures of the heterochiral dimer.*

The calculated vibrational spectrum shown in Figure 17 is similar to the experimental IRMPD spectrum. The total number of bands, their magnitudes and the wavelengths of absorption match the results obtained experimentally.

The Table 2 gives a comparison between the frequencies obtained experimentally with the calculated frequencies of the most abundant stable SR and SS conformers (SR-Cam-AlaH$^+$(1) and SS-Cam-AlaH$^+$(1)). The calculated frequencies tabulated below are not scaled. Since the experimental spectra are recorded only in the fingerprint region (1000-2000 cm^{-1}), the calculated low

frequency modes (<1000 cm^{-1}) cannot be observed experimentally. These low frequency modes at 63, 172 and 642 cm^{-1} mainly correspond to a rocking motion

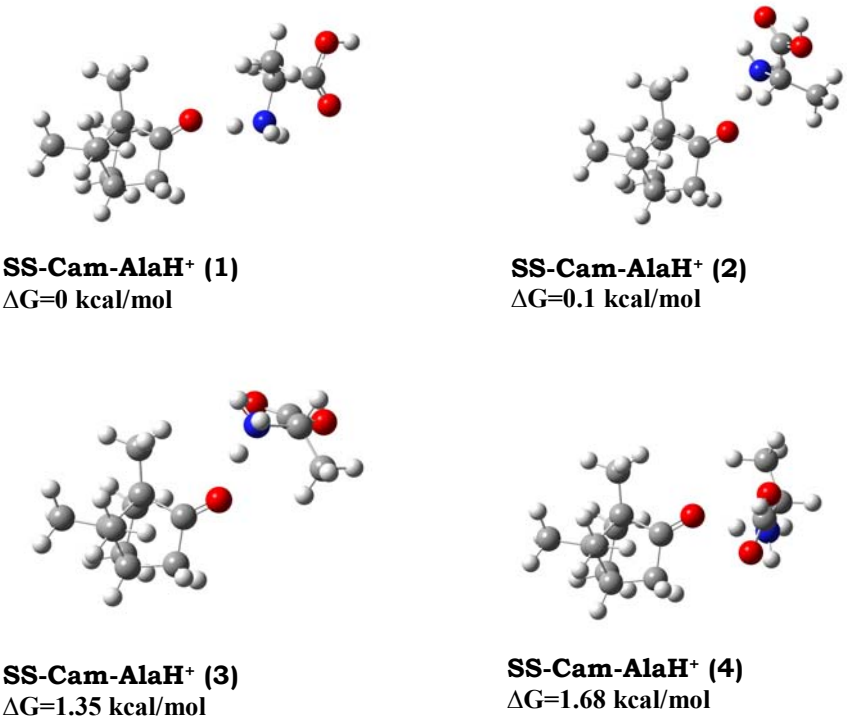

Figure 16: *Stable structures of homochiral dimer.*

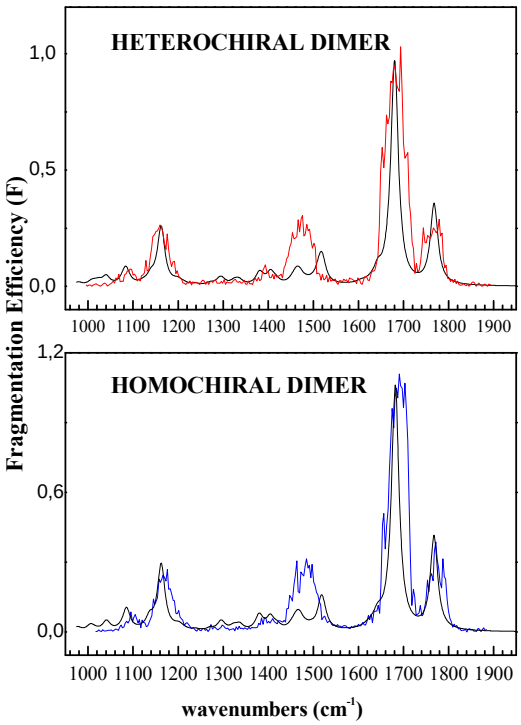

Figure 17*: The simulated vibrational spectrum by convoluting scaled frequencies by a Lorentzian line shape of 22 cm^{-1}. The scaling factor being 0.975.*

Frequency (cm^{-1})				Assignment
Heterochiral dimer		Homochiral dimer		
Experimental	Calculated	Experimental	Calculated	
	63		61	Rocking motion of both the units.
	172		172	Hindered rotation of camphor methyl groups.
	642		643	OH bend, out of the plane of the COOH group.
1164	1191	1173	1193	OH bend, in the plane of the COOH group.
1475	1557	1485	1555	Umbrella motion of the protonated amine of alanine.
1693	1723	1690	1724	Carbonyl stretch in camphor.
1771	1812	1779	1812	Carbonyl stretch of the –COOH group in alanine.
	2684		2712	Stretch mode localised on the hydrogen-bonded NH.
	3493		3493	Asymmetric stretch of NH_3^+ group.
	3729		3730	OH stretch of alanine.

Table 2*: List of frequencies absorbed and the nature of vibrations involved by each dimer in the infrared region (50-4000 cm^{-1}).*

of the camphor and alanine units. These modes have exactly the same frequencies for the two diastereoisomers. In the finger-print region the most active mode is calculated at 1191 cm^{-1}. This mode is localised on the alanine unit and corresponds to the bending vibration of the COOH group, in the COOH plane, slightly coupled with bending of the NH group. Moving to the blue, in between 1500 and 1510 cm^{-1}, there exist the bending modes located on the methyl groups of camphor and protonated alanine. They are coupled together and appear at the same frequencies in both the dimers. The umbrella motion of the protonated amine of alanine is calculated at 1555 cm^{-1} for the homochiral dimer and 1557 cm^{-1} for the heterochiral dimer. This mode, together with the bends

described above, correspond to the peak at 1475 and 1485 cm^{-1} for hetero and homochiral dimers respectively. The characteristic vibration of carbonyl stretches are calculated at ~1723 cm^{-1} for that of camphor and 1812 for that of alanine for both the diastereomers. They correspond to the peaks observed at 1690 and 1771 cm^{-1} in case of the homochiral and 1693, 1779 cm^{-1} in case of the heterochiral dimer. It is interesting to note that the carbonyl stretch mode of camphor is coupled with a deformation of the terpenoid ring in both the dimers. The NH stretch mode localised on the hydrogen- bonded NH is calculated at different values for the homochiral (2714 cm^{-1}) and heterochiral (2684 cm^{-1}) complexes. It is too high in frequency for being observed in our experimental conditions.
Further to the blue, the calculated vibrations mostly correspond to the symmetric and asymmetric stretch of alkyl groups of camphor (3116 cm^{-1}), asymmetric stretch of NH bond of protonated alanine (3493 cm^{-1}) and symmetric stretch of OH bond in alanine (3729 cm^{-1}). In this range, there is no difference between the homochiral and heterochiral complex.

V. DISCUSSION

The experimental IRMPD spectra are the same for the two diasteroisomers. Indeed, all the calculated structures expected to be populated at room temperature, and thus taken into account for simulating the vibrational spectra, show very similar structures which do not lead to different spectroscopic signature in the fingerprint region.

Calculated energetics are also the same for the two diastereomers. As seen above, the difference in the binding energies of the heterochiral and homochiral complexes is negligible (0.22 kcal/mol) and does not account for the differences in formation or fragmentation efficiency. Other methods have been used, either within the frame of DFT or post Hartree Fock ab initio methods. Whatever the functional used (WB97XD or M062X with the same basis set as before), or with the MP2 method, the SR complex is always slightly more stable, which is in contradiction with the experimental results. One possibility for accounting for this discrepancy is to suppose that the the dissociation or the formation of the complexes involves an energy barrier (kinetic control). To test this hypothesis, a

reaction path from the isolated molecule to the dimer has been calculated. The distance (r) between the proton associated with the amino group of alanine and the carbonyl oxygen of camphor, in other word the intermolecular distance, has been increased step by step and all the other degrees of freedom have been optimised. The step size has been taken to 0.1 Å. E *vs* r plots of the two dimers are given in Figure 18.

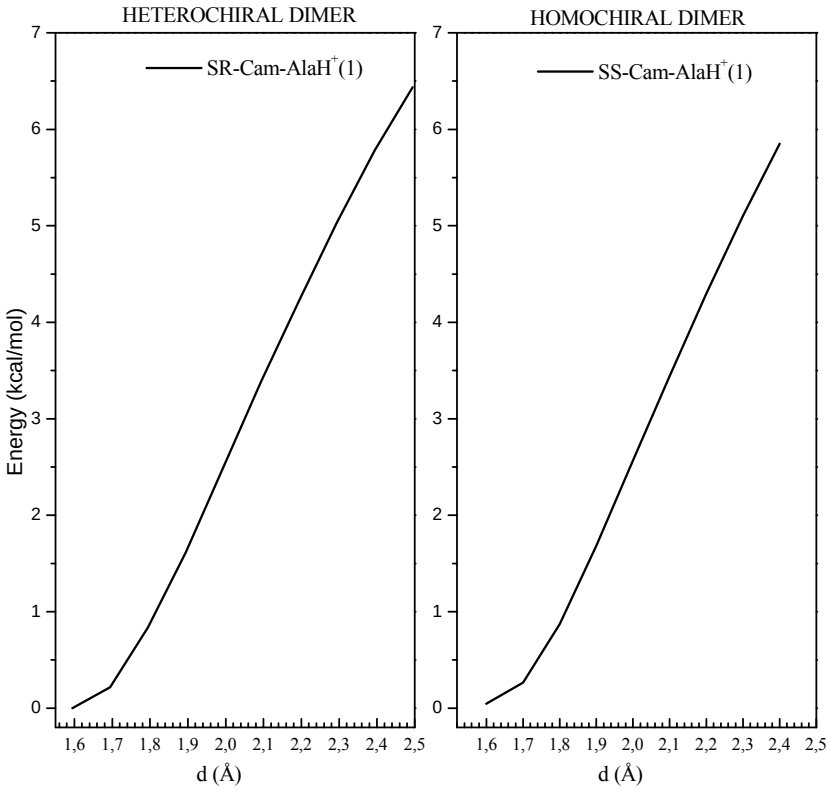

Figure 18*: Energy vs intermolecular distance of most stable conformers of the heterochiral and homochiral dimers.*

Two conclusions can be drawn from the plot shown in Figure 18. The first observation is that there is no barrier. It is therefore impossible to evoke kinetic arguments and a presence of stereoselective barriers for explaining the differences in fragmentation efficiency. Second, the two diastereomers follow exactly the same trend, at least for the most stable dimer.

However, we have to keep in mind the fact that we observe ionic complexes at room temperature. The difference in behaviour between the two diastereisomers can arise from higher-energy conformers. Indeed, we have to keep in mind that there are more conformers with ΔG under 2 kcal/mol for the

heterochiral dimer (SR) (6 confomers) than for the homochiral dimer (SS) (4 conformers). The trend is amplified if we set the ΔG limit at 6 kcal/mol (15 isomers for SR, 9 for SS).

VI. CONCLUSION

It is difficult to draw a definitive conclusion about the effects of chirality on the interaction between ionic species from the studies done above. The spectroscopic results seem to confirm the hypothesis made earlier that too rigid systems like those containing bicyclic terpenoid frame are not flexible enough for the secondary interactions necessary for chiral recognition to take place. However, the infrared absorption bands obtained experimentally appear broad due to superimposition of absorption due to hot species as is expected in studies done in room temperature. This would not allow observing tiny differences between the two diastereomers, if any. The calculated geometries are very similar; in particular, the hydrogen bond characteristics are identical (distance and angle) for the two complexes. However, the calculated spectra described in this chapter differ in the ν(NH) stretch region. In particular, the bonded NH appears at different frequencies, which is quite unexpected considering the similarity between the structures. Unfortunately, this frequency range is not easily accessible neither with CLIO nor with the OPOs which are available in our Institute.

On the other hand the differences observed between the two dimers in terms of efficiency of formation or fragmentation are not reproduced by the energies calculated. Furthermore, no energy barrier could be determined on the reaction path for the dimer formation. However, we have to explain why the fragmentation efficiency is different for the two dimers.

Collision-induced dissociation is usually described within the frame of statistical reactions. In this context, a RRKM reaction rate can be calculated for the dissociation of the complexes. It is expressed as:

$$k(E) = \frac{S^{\#}(E - E_0)}{h\rho(E)}$$

where S is the sum of vibrational states at the transition state, and ρ the density of vibrational states in the reactant.

As we have seen earlier, there is no barrier on the reaction path; therefore the transition state will be set close to the products. The transition state is therefore the same for the heterochiral and the homochiral complexes and it resembles the product, *i.e.* separated species.

In these conditions, the ratio $k(E)_{RS}/k(E)_{SS}$ is given by $\rho(E)_{SS}/\rho(E)_{RS}$.

To check this hypothesis further we will first calculate some sort of "effective density" of state taking into account all the conformers. As has been calculated, there are six conformers present for heterochiral dimer and four for homochiral dimer, with ΔG at room temperature smaller than 2 kcal/mol. These higher energy isomers contribute less to the "effective density of states" leading to $\rho(E)_{SS}/\rho(E)_{RS}$ larger than unity. This gives a qualitative explanation of the larger fragmentation efficiency observed in the heterochiral complex. Then we will use these densities of states to roughly evaluate the fragmentation efficiency of the two diastereomers using the RRKM expression and to get a quantitative value of the ratio between dissociation rate constants.

VII. REFERENCES

1 F. Lahmani, K. Le Barbu, and A. Zehnacker-Rentien, Journal of Physical Chemistry A 103 (13), 1991 (1999).

2 D. Scuderi, K. Le Barbu-Debus, and A. Zehnacker, Physical Chemistry Chemical Physics 13 (40), 17916 (2011).

3 J. B. Fenn, M. Mann, C. K. Meng, S. F. Wong, and C. M. Whitehouse, Science. 1989, 64-71. (1989).

4 D. BRUKER, (2002), Vol. 1.

5 D. Scuderi, P. Maitre, F. Rondino, K. Le Barbu-Debus, V. Lepere, and A. Zehnacker-Rentien, Journal of Physical Chemistry A 114 (9), 3306 (2010).

6 P. Gates, (2004).

7 L. MAC ALEESE, L'UNIVERSITE PARIS-SUD 2006.

8 R. E. March, Journal of mass spectrometry 32 (4), 351 (1997).

9 K. R. Jonscher and J. R. Yates Iii, Analytical Biochemistry 244 (1), 1 (1997).

10 M. E. Milner, University of York, 2010.

11 N. C. Polfer, Chemical Society Reviews 40 (5), 2211 (2011).

12 E. C. Kaposta, Freien Universit¨at Berlin, 2005.

13 J. Lemaire, P. Boissel, M. Heninger, G. Mauclaire, G. Bellec, H. Mestdagh, A. Simon, S. L. Caer, J. M. Ortega, F. Glotin, and P. Maitre, Physical Review Letters 89 (27), 273002 (2002).

14 D. van Heijnsbergen, G. von Helden, G. Meijer, P. Maitre, and M. A. Duncan, Journal of the American Chemical Society 124 (8), 1562 (2002).

15 M. A. Duncan, International Reviews in Physical Chemistry 22 (2), 407 (2003).

16 S. Mukamel and J. Jortner, Journal of Chemical Physics 65 (12), 5204 (1976).

17 L. Mac Aleese, A. Simon, T. B. McMahon, J.-M. Ortega, D. Scuderi, J. Lemaire, and P. Maître, International Journal of Mass Spectrometry 249-250, 14 (2006).

18 R.Prazeres., J.M.Berset., R.Chaput., F.Glotin., D.Jaroszinski., and J.M.Ortega., Nucl.Intrum.Meth.B 89 (1-4), 54 (1994).

19 http://clio.lcp.u-psud.fr/ (2012).

20 N. C.Polfer, Chem.Soc.Rev. 40, 2211 (2011).

CONCLUSION

This thesis is based on two main aspects: spectroscopy and energetics. While the spectroscopic aspects have been studied by probing neutral molecules, both spectroscopic and energetic studies have been performed on ionic complexes. However the main motive behind these two studies has been the same. In each case the interactions between chiral molecule(s) have been studied.

The *spectroscopic studies* have been performed by probing neutral molecules. The cinchona alkaloids Quinine and Quinidine have been chosen for their interesting structure consisting in two bulky units joined by a chiral linker. The two molecules differ in the configuration of atoms around the chiral linker and are known as floppy molecules. To understand whether the slight differences in physical properties between the two pseudo-enantiomers arise from the geometry of the molecule around the chiral linker or far away from it, they have been isolated in gas phase and studied in jet cooled conditions.

From the ground state spectroscopic studies, the most stable conformer is the *cis*-γ-open(3) form for both the molecules. However, the two pseudo-enantiomers show some slight spectroscopic differences. There are two possible reasons behind the observed differences:

1. Quinidine, which is a floppier molecule in comparison to Quinine, is experimentally easier to ablate and shows only the dominant *cis*-γ-open(3) conformer in the gas phase. While in case of Quinine there exists an ambiguous band which has been assigned either to a *trans*-γ-open(3) conformer or more likely to a hot band. The differences in the gas-phase spectroscopy of the two pseudo enantiomers is not likely to arise from the gas-phase thermodynamics but more from different solid-state structures which result to different ablation efficiency.

2. More pronounced differences between the pseudo-enantiomers appear in solution than in the gas phase. While Quinine mostly exists in the *cis*-γ-open(3) form in $CHCl_3$, conformers of higher energy are stabilised too in the case of Quinidine. For instance, the value of ΔG at room temperature of the higher energy conformer trans-γ-open(3) of Quinine increases from 1.28 kcal/mol to 1.46 kcal/mol from gas phase

to solution. On the contrary the free energy of the *cis*-γ-closed(1) conformer of Quinidine decreases from 1.19 kcal/mol to 0.91 kcal/mol. Differences between the enantiomers Quinine and Quinidine have also been observed in the VCD spectra, as they show good mirror-image relation in the range above 1300 cm^{-1}, but the mirror-image relation is lost in the range below 1300 cm^{-1}, especially for the deformation modes located on the alkaloid sub-unit.

3. When the vinyl group of neutral Quinine is saturated it gives rise to more floppiness as is observed experimentally in Hydroquinine and Hydroquinidine. However, it is difficult to compare the experimental results with theory due to the following two reasons:

a. The ν(CH) stretch region of the infrared spectrum displays broad and congested bands. Thus the slight differences between the two enantiomers which were observed in the electronic excitation spectrum could not be completely recovered in the IR-UV double resonance spectra. Another difficulty was to obtain a perfectly cold jet. As is observed in the electronic and vibrational spectrum absorption by hot species could not be totally eradicated. Different valve conditions and position of the jet were tried to decrease the formation of hot species to a minimum.

b. The negligible differences between the enantiomers Quinine and Quinidine are more pronounced in case of Hydroquinine and Hydroquinidine. Calculations of ΔG in gas phase yield nine conformers for Hydroquinidine compared to three in case of Hydroquinine with ΔG<1.6 kcal/mol at room temperature. Calculations show that the conformers with closed geometry and *cis* orientation of OMe group are higher in energy than the *cis*-open variety. This difference in energy is higher in Hydroquinine (1.57 kcal/mol of *cis*-β-closed(7b)) compared to that of Hydroquinidine (1.15 kcal/mol of *cis*-γ-closed(1b)) at room temperature.

c. High energy conformers are more abundant in solution than in supersonic-expansion conditions because solutions are at room temperature. Hence VCD studies in solution are eagerly awaited to confirm the abundance of higher energy

mirror image relation between Hydroquinine /Hydroquinidine compared to Quinine/Quinidine.

The *energetic aspects* have been studied in the case of ionic species trapped in an ion trap at room temperature. The interactions between the two diastereomeric dimers formed by *S*-Camphor with *R* and *S* protonated Alanine have been studied. It has been observed that the homochiral dimer is easier to form and harder to fragment compared to the heterochiral dimer. However this observation is neither reflected by spectroscopy nor by calculations. Indeed, the calculated geometries are identical for the two diastereomers as are the calculated binding energies or IR spectra in the fingerprint region. The infrared absorption bands obtained experimentally at room temperature appear broad due to absorption by hot species thereby not allowing us to observe the tiny differences between the two diastereomers, if any.

The calculations show no energy barrier for the formation of the two diastereomers. It is therefore not possible to explain the differences in fragmentation efficiency in terms of kinetic control of the reaction. Another possible explanation could lie in differences in fragmentation efficiency of the two dimers due to different density of states. To confirm this hypothesis, one should calculate the reaction rates within the frame of the statistical methods (RRKM theory). Indeed, one looks forward to calculate the “effective density of state” for the six conformers present for heterochiral dimer and four for homochiral dimer, considering ΔG at room temperature smaller than 2 kcal/mol. With the help of these densities of states and the RRKM expression, one can roughly evaluate the fragmentation efficiency of the two diastereomers by obtaining a quantitative value of the ratio between dissociation rate constants.

In all the systems we have studied, it seems that chiral recognition is less important in the lowest-energy structure than it is for higher-energy structures. For example, both the UV and the IR spectra of Quinine and Quinidine cooled in the supersonic expansion are similar. The pseudoenantiomers differ more in solution, as

evidenced by their VCD spectra, because solutions are at room temperature and higher-energy conformers are populated. The manifestation of pseudoenantiomerism is more pronounced in the Hydroquinine/Hydroquinidine pair. Indeed, Hydroquinidine has the maximum number of calculated high-energy conformers among the four studied Cinchona alkaloids. It has a very different spectral signature than the rest three. This makes it easier to differentiate between Hydroquinine and Hydroquinidine.

Similarly in the studies done in the ion trap, the lowest-energy structure of the camphor/protonated alanine complex is the same in terms of binding energy as well as spectroscopic signature in the fingerprint region for the two diastereoisomers. This contrasts with CID measurements which show larger fragmentation efficiency for the heterochiral complex. This has been tentatively explained by the fact that the heterochiral dimer has larger number of conformers than the other diastereomer. The differences between them lie in their fragmentation efficiency and one hopes to support this experimental evidence by calculating the dissociation rates of not only the low-energy conformers but also the higher energy ones.

Perspectives

Earlier studies performed on neutral jet-cooled complexes between an aromatic alcohol and camphor or camphene[1] showed no chiral discrimination in the S_0-S_1 electronic spectrum. This was a rare observation and was thought to be arising from the rigidity of the terpenic globular frame which allowed only the hydrogen bond from alcoholic chromophore to Camphor to occur. The same observation seems to hold in ionic complexes for the Camphor/protonated Alanine complex. The study of complexes made from more flexible molecules showing ability for multiple hydrogen bond formation is foreseen.

The studies on cinchona alkaloids will be complemented in several directions. We first look forward to some technical developments of the setup. For instance,

different valve parameters are to be used to obtain better cooling conditions. Second, we would like to go one step further in the comparison between the conformational studies in the gas phase, as brought by supersonic jet spectroscopy experiments, and those in solution brought by VCD. To bridge the gap between gas phase and solution, we intend to study clusters of Quinine with usual solvents (mainly water and $CHCl_3$). We want to know whether higher-energy conformers could be stabilised by the solvent and show larger differences between the two enantiomers than the lower-energy conformers do. The formation of hydrates by addition of water externally, by introducing it through the valve or internally by mixing it with the solid mixture containing the studied molecules has failed so far. We intend to improve the jet conditions to form the complexes.

So far, we have not tried to perform a study of the vibrational transitions in the excited vibrational levels of the excited electronic state of Quinine and its derivatives, or in the ion. Quinine having a very short fluorescence life-time decays within the pulse of the pump laser (UV), the study of the S_1 state might be difficult. However, the vibrational spectroscopy of the ion should not be out of the reach. Indeed, Quinine loses the fragment m/z 136 in the ion, the formation of which can be used to monitor the IR absorption. Thus in future we would like to study the UV-IR double resonance study of neutral and ionic Quinine using a Time of Flight mass spectrometer as detector.

In future, we would also like to know whether the differences observed between the two pseudo enantiomers persist if a substitution is introduced either in the OH group of the chiral linker or the ethylene unit attached to the Quinuclidine unit (for example a carbamoylated Quinine unit). These systems are inspired by those used in asymmetric catalysis[2,3]. We shall also try to form complexes which mimic those involved in asymmetric catalysis, namely, Quinine/ketone complexes inspired by the systems involved in the asymmetric hydrogenation of ketones. Attempts to form complexes between acetone and camphor with protonated Quinine in the ion trap failed, but we shall try in the near future to make complexes between neutral Quinine and acetone or camphor.

REFERENCES

(1) Lahmani, F.; Le Barbu, K.; Zehnacker-Rentien, A. *Journal of Physical Chemistry A* **1999**, *103*, 1991.

(2) Vargas, A.; Burgi, T.; Baiker, A. *Journal of Catalysis* **2004**, *226*, 69.

(3) Sonderegger, O. J.; Ho, G. M. W.; Burgi, T.; Baiker, A. *Journal of Catalysis* **2005**, *230*, 499.

CHIRAL RECOGNITION IN NEUTRAL AND IONIC MOLECULAR COMPLEXES

The main objective of this thesis is a spectroscopic study of molecules or complexes bearing multiple chiral centres in the gas phase, to understand the effects of stereochemistry on their structural properties. Neutral cinchona alkaloids have been introduced intact in gas phase by laser-ablation. They have been studied by combining supersonic expansion with laser spectroscopy. The two pseudo-enantiomers Quinine and Quinidine show similar electronic and vibrational spectra, in line with similar structure. Their properties in solution differ more, as shown by Vibrational Circular Dichroism (VCD) experiments. This difference is further enhanced in Hydroquinine and Hydroquinidine. Lastly chiral recognition has been studied in ionic complexes in an ion trap. A homochiral preference has been shown in the stability of the complexes formed between *S*-Camphor and *R* and *S* protonated Alanine. However, the calculated interaction energy as well as the IRMPD spectrum in the fingerprint region are identical. The role of higher energy conformers in chiral recognition has been discussed.

Key words:
Chiral Recognition
Laser ablation
Vibrational Circular Dichroism (VCD)
Pseudo-enantiomers
Supersonic Expansion
Infrared multiple-photon dissociation (IRMPD)

RECONNAISSANCE CHIRALE DANS DES COMPLEXES MOLECULAIRES NEUTRES ET IONIQUES.

L'objectif principal de cette thèse est l'étude spectroscopique de molécules ou de complexes portant plusieurs centres chiraux en phase gazeuse, pour comprendre les effets de la stéréochimie sur leurs propriétés structurales. Des alcaloïdes dérivés de la *Cinchonine* ont été introduits intacts en phase gazeuse par ablation laser. Ils ont été étudiés en combinant un jet supersonique avec de la spectroscopie laser. Les deux pseudo-énantiomères Quinine et Quinidine ont montré des spectres électroniques et vibrationnels similaires, en accord avec leur structure similaire. Leurs propriétés en solution diffèrent davantage, comme le montrent les expériences de dichroïsme circulaire vibrationnel (VCD). Cette différence est encore plus marquée dans l'Hydroquinine et l'Hydroquinidine. Enfin la reconnaissance chirale a été étudiée dans des complexes ioniques dans un piège à ions. La stabilité des complexes formés entre *S*-camphre et les *R* et *S*-Alanine protonées indique une préférence homochirale. Cependant, l'énergie d'interaction calculée ainsi que les spectres IRMPD dans la région des empreintes digitales sont identiques. Le rôle des conformères plus hauts en énergie dans la reconnaissance chirale a été discuté.

Mots Clés :
Reconnaissance chirale
Ablation laser
Dichroïsme circulaire vibrationnel (VCD)
Pseudo-énantiomères
Jet supersonique
Dissociation infrarouge multi-photonique(IRMPD)